Institute of Mechanics and Computational Mechanics

Leibniz Universität Hannover

Modeling and numerical simulation of Air spring bellow

Master's thesis
Jamal Ahmed Bhatti
Student matriculation number: 10034207

November 25, 2023

Supervisor(s):
Engr. Boris Balanchonzew
Dr. Jorge-Humberto Urrea-Quintero

Examiner(s):
Prof. Dr.-Ing. Udo Nackenhorst
Prof. Dr. Thomas Wick

Plagiarism Declaration

I declare that this work is my own and I have not used any external material other than the provided sources with the appropriate citations. Furthermore, this work, or parts thereof, has not been previously submitted in the same or similar form to the examination office.

Hanover, ...

....
Name, Family Name

Acknowledgements

I extend my heartfelt gratitude to my supervisor, Mr. Boris Balanchonzew, and Dr. Dieter Kardas at ContiTech Air Spring Systems GmbH. Their insightful discussions and invaluable guidance played a pivotal role in shaping the trajectory of my work. I am particularly grateful to senior engineer Jens Jagusch for his profound insights into air springs and his unwavering assistance in overcoming challenges. This work has been accomplished with the generous support of ContiTech Air Spring Systems GmbH.

I would also like to express my appreciation to Mr. Mark Lindenberg for his continuous support and keen interest in the progress of this thesis.

A special acknowledgment goes to my office mate, Paul Huber, whose exceptional clarity in explanations and willingness to assist with any query significantly facilitated my understanding.

I owe a debt of gratitude to Prof. Dr.-Ing. Udo Nackenhorst and Prof. Dr. Wick for their consistent support and guidance not only during the thesis but throughout my entire academic journey. I am thankful to Leibniz University for providing advanced courses that have significantly contributed to my personal and professional growth.

A sincere thanks is extended to my supervisor, Dr. Jorge-Humberto Urrea-Quintero, for his unwavering guidance and inspiration, which have positively impacted both my academic and personal development.

Lastly, I express my deepest gratitude to my father, Mussawir Ahmed Bhatti, my elder brother, Faraz Ahmed Bhatti, and the rest of my family, friends, and all teachers for their enduring support and emphasis on the value of education.

Abstract

Air springs are integral for mitigating vibrations in diverse vehicles, encompassing both commercial and private sectors. Comprising rubber and fabric layers, these springs can be conceptualized as composite materials. Modeling and simulating the fabric layer, and rubber at 3D using Finite Element Method (FEM) proves computationally demanding. To address this, numerical homogenization is pivotal for capturing the material's heterogeneity. This study tackles this challenge through a Representative Volume Element (RVE) approach, defining the effective stiffness of the heterogeneous air spring material and developing requisite tools for generalization.

Utilizing the commercial software ABAQUS, finite element simulations were conducted with the support of a custom plugin. This plugin was developed to enhance efficiency in applying periodic boundary conditions and automating the homogenization process. Initially validated for linear perturbation analysis, the plugin was subsequently extended to accommodate nonlinear analysis. In the linear perturbation phase, various homogenization scenarios were generated, encompassing monotropic, orthotropic, transverse isotropy in all three axes, and isotropy. These scenarios served as simplifications of the linear anisotropic model and were validated using the theoretical homogenization method.

In nonlinear analysis, the process entails transferring data to MATLAB, where users define hyperelastic material models. This step is also automated, with the system calculating the necessary derivatives and material model parameters based on the user's specifications.

The stress and strain responses from the Representative volume element (RVE) obtained in ABAQUS are then exported to MATLAB. At this juncture, a customized variation of the optimization algorithm, Adaptive Moment Estimation (ADAM), is introduced. This algorithm facilitates the determination of parameters for a new constitutive model, taking into account all six components of stress simultaneously. This is a departure from traditional approaches that compare data from stress in one or two directions. Once a suitable model and its parameterization are established, a Fortran-based User Material (UMAT) script is formulated. This script enables the simulation of the air spring's bellow as a homogeneous material within ABAQUS, providing a versatile framework that users can readily adapt to their specific material models.

This work presents homogenized models for air spring bellows, developed through both strain-based and invariant-based approaches. Results indicate that while the strain-based approach aligns well with the data, it poses stability challenges. Conversely, invariant-based approaches demonstrate stability but encounter difficulties in data fitting.

Keywords: Rubber-Cord Composite, Linear Anisotropy, RVE, Nonlinear Anisotropy, ABAQUS, Plugin, Optimization, UMAT

Contents

List of Figures

List of Tables

Glossary

J Determinant of deformation gradient also known as change in volume ratio. 12

Ψ Helmholtz free energy potential. 27

$\bar{C}$ Distortional part of the Right Cauchy-Green tensor $\bar{C} = J^{-\frac{2}{3}} F^T \cdot F$. 28

$\bar{F}$ Distortional part of the deformation gradient $\bar{F} = J^{-\frac{1}{3}} F$. 28

$\bar{b}$ Distortional part of the Left Cauchy-Green tensor $\bar{b} = J^{-\frac{2}{3}} F \cdot F^T$. 30

A^∇ Jaumann stress rate. 23

E_{lin} Linearized Green-Langrange strain tensor. 14

σ° Truesdell rate of Cauchy stress. 22

η_c Entropy in current configuration. 20

$\mathcal{K}$ Kinetic energy. 19

$\mathcal{P}_{int}$ Stress power. 19

$\mathcal{P}$ Rate of external mechanical work. 19

$\mathcal{Q}$ Thermal power. 20

AM Angular momentum. 17

C Right Cauchy-Green tensor. 14

E or ε^G Green-Langrange strain tensor. 14

LM Linear momentum. 17

P First Piola-Kirchhoff stress tensor. 16

S Second Piola-Kirchhoff stress tensor. 16

T Traction in reference configuration, also known as first Piola-Kirchhoff or nominal traction vector. 15

U Right or material stretch tensor. 15

σ Cauchy stress tensor. 16

τ Kirchhoff stress tensor $\tau = J\sigma$. 16

b Body force. 18

b Left Cauchy-Green tensor. 14

d Rate of deformation tensor, it is the symmetric part of l. 22

l Spatial velocity gradient. 21

t Traction vector in current configuration, also known as Cauchy traction vector. 15

v Left or spatial stretch tensor. 15

w Spin tensor, it is the skew-symmetric part of l. 22

$\mathbb{C}$ Lagrangian Elasticity Tensor. 24

$\mathbb{c}$ Eulerian Elasticity Tensor. 25

ϱ Density. 18

F Deformation gradient tensor. 12

ADAM Adaptive Moment Estimation. 2, 88

CAGR compound annual growth rate. 2

FEM Finite Element Method. 2

RVE Representative volume element. 1, 2

UMAT User Material. 2

Chapter 1

Introduction

Air springs provide significant advantages in terms of vibration performance and energy storage. The stiffness of an air spring constitutes a crucial performance parameter in its design and application. Analyzing the stiffness of an air spring using the finite element method poses a challenge due to the need to simulate the heterogeneity of materials within the air spring.

This thesis centers around the application of the RVE approach, a method instrumental in bridging micromechanical properties at the micro scale to the macro scale of structures. This approach is particularly valuable for homogenizing material properties. Within this context, a novel plugin has been developed to facilitate the implementation of periodic boundary conditions in Abaqus, laying the groundwork for detailed computational homogenization.

The computational homogenization presented in this work initially focuses on linear analysis, extending subsequently to encompass nonlinear analysis. The practical application of this approach involves determining parameters for a homogenized material model tailored to air springs. Specifically, the study emphasizes a hyperelastic material model for the matrix material, with broad applicability to diverse components such as tires, air springs, and belts. Notably, the methodology is readily extendable to composite materials with two constituents, assuming straight and parallel fiber materials, resulting in a highly anisotropic response. Conversely, considering random fiber directions leads to isotropic responses in composite materials.

The primary focus of this investigation is the bellow structure, a key component of air springs crafted from rubber with chord reinforcement. Comprising multiple layers of fabric and rubber, the fabric layers contain twisted chords aligned parallel to each other at fixed intervals and angles with the global axis. The cords, fashioned from materials like steel, aramid, polyamide, or nylon, contribute distinct mechanical properties to the air spring based on their specific stacking sequence.

The complexity of cord-reinforced rubber composites arises from the intricate internal geometry and strongly anisotropic, nonlinear material behavior resulting from twisted structures of polymeric filaments within the cords. The demand for accurate simulation procedures that predict material behavior in alignment with experimental results under varying loading conditions is particularly in demand.

While it is conceivable to model chords directly at the global scale for the most accurate solution, the computational challenges associated with the macro problem's simulation size make this approach impractical. Consequently, a more viable strategy involves modeling properties at the micro scale and homogenizing the material at the global scale, thereby simplifying the simulation process. This necessitates the development of a comprehensive homogenization theory and work pipeline to streamline these procedures effectively.

1.1 Background and Motivation

The global Air Spring market exhibited a valuation of USD 2741.69 million in 2022, with projections indicating a robust expansion at a compound annual growth rate (CAGR) of 5.49% throughout the forecast period, potentially reaching USD 3777.83 million by 2028 [32]. Several factors propel the air spring market, including consumer demand, market dynamics, regulatory considerations, and notably, product innovation.

Product innovation stands out as a significant driver, playing a pivotal role in securing a larger market share. ContiTech Luftdersysteme GmbH, a major global player, manufactures a diverse range of air springs encompassing rolling lobe, convoluted air springs, sleeve-type air springs, guided air springs, and convoluted air springs. These variations find applications in various sectors, with some catering to transport buses and others finding utility in the railway industry.

At the core of air spring performance lies the bellows, and designing these bellows to meet specific loading requirements involves extensive empirical testing. Even minor design adjustments necessitate prototyping and rigorous testing, constituting a costly and time-consuming process. FEM simulations offer a solution by detecting design flaws early on, significantly streamlining the design process and excluding unworthy designs before progressing to the prototyping stage.

The bellows, composed of rubber and fabric layers, exhibit responses influenced by the type of fiber, its angle, and laying sequence. Tailoring bellows for specific applications poses a challenge, given the varying dimensions required for fitting air springs in different vehicles, such as BMW and Mercedes. Optimizing for such conditions requires virtual testing, provided that virtual testing accurately represents the true model and predicts properties with precision, expediting the process of achieving the most optimized air spring, a demand echoed by end-users.

Linear differential equations were formulated by Loeb et al. [25] to compute both vertical and lateral stiffness. Kao and Warholic [21] and Wu et al. [44] employed an orthotropic material model, homogenizing the bellow structure using the Halpin-Tsai mixing rule—an analytical method of homogenization. Ye et al. incorporated rebar reinforcements into the air spring. On the other hand, Cembrola and Dudek [10] utilized a transversely isotropic model, employing the Halpin-Tsai model for micro-scale homogenization and classical lamination theory for meso-scale considerations. Despite facing challenges in predicting shear response and Poisson's ratio, attempts were made to calculate properties through experimentation.

Rebars were also utilized by Palanivelu et al., Alkan et al., Yanjin et al., Wei and Olatunbosun [28, 2, 45, 42] for reinforcement. Wei-min et al. [43] employed an orthotropic model, although specific details of the homogenization process were not provided in the paper. In Behnke and Kaliske's [8] work, a constitutive model for the chord was developed in 1D and implemented

directly into the 3D model without homogenization. Lastly, Yintao et al. [48] made an attempt to model the helix structure of the chord.

However, accurately modeling cord-reinforced rubber composites remains a challenge. Traditional Rebar models, originating from their use in simulating reinforced bars in concrete structures, have been adopted for air spring modeling. These models, however, oversimplify material behavior, assuming linearity and neglecting the inherent non-linearity of the rubber matrix, the anisotropy, non-linearity, and inelastic behavior of reinforcement cords. Rebar models also separate the rubber matrix and reinforcement cords, overlooking potential interactions and locally produced stresses. Additionally, Rebar models assume stiffness exists only in the direction of cords, resulting in erroneous strains in other directions due to the highly anisotropic behavior of actual elastomeric composites.

In a preceding study [4], four distinct models were devised to simulate the bellows of air springs, with a specific focus on modeling the fabric layer. The initial model employed a linear orthotropic approach (Model 1), while the second model incorporated a rebar layer (Model 2). Model 3 combined the rebar layer with a linear orthotropic model, and Model 4 introduced a more complex structure, utilizing both a rebar layer and the hyperelastic anisotropic Holzapfel Gasser Ogden model. Subsequently, these models underwent analysis within the overarching global simulation framework. In this extensive model, each layer was meticulously defined in three dimensions, and the fabric layer was characterized by the inclusion of a rebar layer. However, the sheer scale of this simulation model rendered it impractical. Furthermore, the absence of a systematic framework for determining material properties posed a significant limitation in the previous study, compelling the manual estimation of these crucial parameters.

The motivation for the this study stems from these challenges. To render simulations practical, computational homogenization is required to homogenize the fabric layer within the air spring. Establishing a streamlined pipeline for modeling any air spring and deriving its material properties within this framework becomes imperative.

1.1.1 Air spring main components

The primary components of an air spring, as depicted in Figure 1.1.1, consist of a plate, piston, and bellow. To elucidate the function of each component, we discuss a simplistic model that calculates the vertical stiffness of the air spring. The relationship between the vertical load F, relative internal pressure P_r, and effective area A_{ef} can be expressed as:

$$F = P_r A_{ef} = \frac{\pi}{4} P_r d_{ef}^2,$$

where d_{ef} is the effective diameter of the piston. The gas inside the air spring is modeled as an ideal gas, following the relationship $(P_r + P_a) V^n = (P_0 + P_a) V_0^n$, where P_a is the atmospheric pressure, and P_0, V_0 are initial pressure and volume in the air spring. The variable V represents the volume of the air spring at a given height of the piston. Additionally, n is the polytropic index ranging from 1 to 1.4, depending on the gas inside. The vertical stiffness k becomes:

$$k = \frac{dF}{dx} = -nA_{ef}\frac{P_r + P_a}{V}\frac{dV}{dx} + P_r\frac{dA_{ef}}{dx},$$

where $\frac{dV}{dx}$ is the volume change rate of the air spring, and $\frac{dA_{ef}}{dx}$ is the effective area change rate.

This relationship indicates that by adding additional volume, softer spring characteristics can be achieved. Moreover, the value of n adds further distinction, depending on the speed of the thermodynamic change in the air during spring action. For adiabatic assumption, its value can be considered as 1.4, and for isothermal assumption, its value can be assumed to be 1. It's important to note that this simplistic equation does not consider the stiffness of the bellow.

The terms $\frac{V}{dx}$ and $\frac{dA_{ef}}{dx}$ are selected by the designer to tailor the air spring for a specific type of application.

A bellow-type air spring consists of layers of cord reinforcement in the bellow's wall, covered with an elastomeric layer internally and externally. The reinforcing cords, bonded with a Resorcinol-Formaldehyde-Latex (RFL) adhesive system, have a higher elastic modulus than the rubber matrix.

As observed, the cord carries the air spring load, making design parameters like cord angle, thickness, and spacing crucial for the overall life of an air spring. An air spring comprises cord, rubber, and adhesive materials, forming a multi-material system with significantly different physical properties. This heterogeneity, combined with anisotropy induced by the orientation of the reinforcements, poses challenges in both manufacturing and numerical modeling. Being heterogeneous, anisotropic, and involving geometric material non-linearity, the modeling of an air spring requires meticulous attention.

Numerical modeling of cord-reinforced structures, with an emphasis on global-to-local ("mesolevel") approaches, has been extensively studied in the mechanics community. This approach assumes that cord and rubber matrix are smeared on the macroscopic model, while derived meso-mechanics models capture local heterogeneity. Meso-scale finite element analysis of composites, often based on Representative Volume Element (RVE) or Repetitive Unit Cell (RUC) homogenization, has gained popularity for describing the influence of structural parameters on load-displacement characteristics and obtaining effective macroscopic constitutive behavior. Notable contributions in this field include works by [12, 15, 27].

1.1.2 Macro-micro Approach

Continuum mechanics is applicable at various scales, progressing from the micro scale (constituent level) to the meso scale (laminate, composite, and/or stiffened panel level), and finally to the global scale (global/structural level), as illustrated in Figure 1.1.2.

Homogenization techniques provide the properties or response of a 'structure' based on the properties or response of the structure's 'constituents'. In contrast, localization techniques offer the response of constituents based on the response of the structure.

Several homogenization methods exist, ranging from simple analytical approximations like Voigt/Reuss to more accurate but complex methods such as the Mori-Tanka method or Generalized Method of Cells (GMC), and fully numerical methods that are highly accurate but computationally demanding. Each method has its limitations, particularly in capturing effects like damage or viscoelasticity.

Micromechanical and macromechanical approaches differ in their starting points—the former begins at the micro scale or constituent level, while the latter starts at the homogenized material
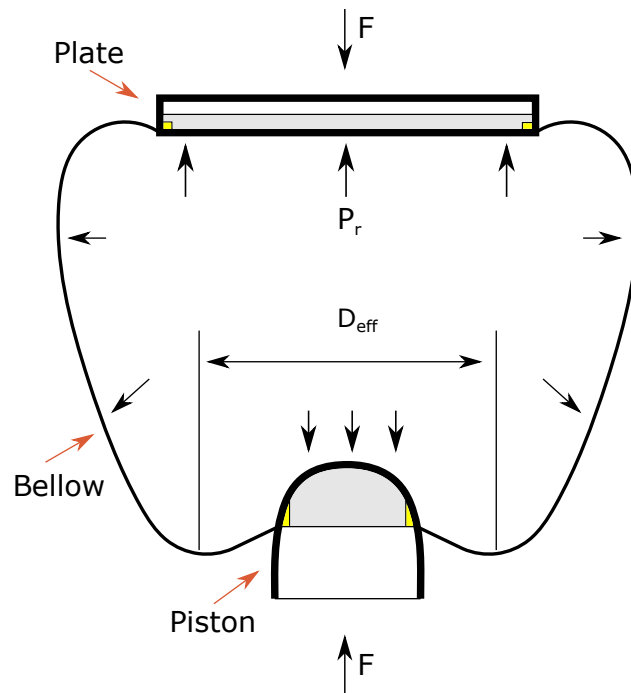
Figure 1.1.1: Basic components of air spring.
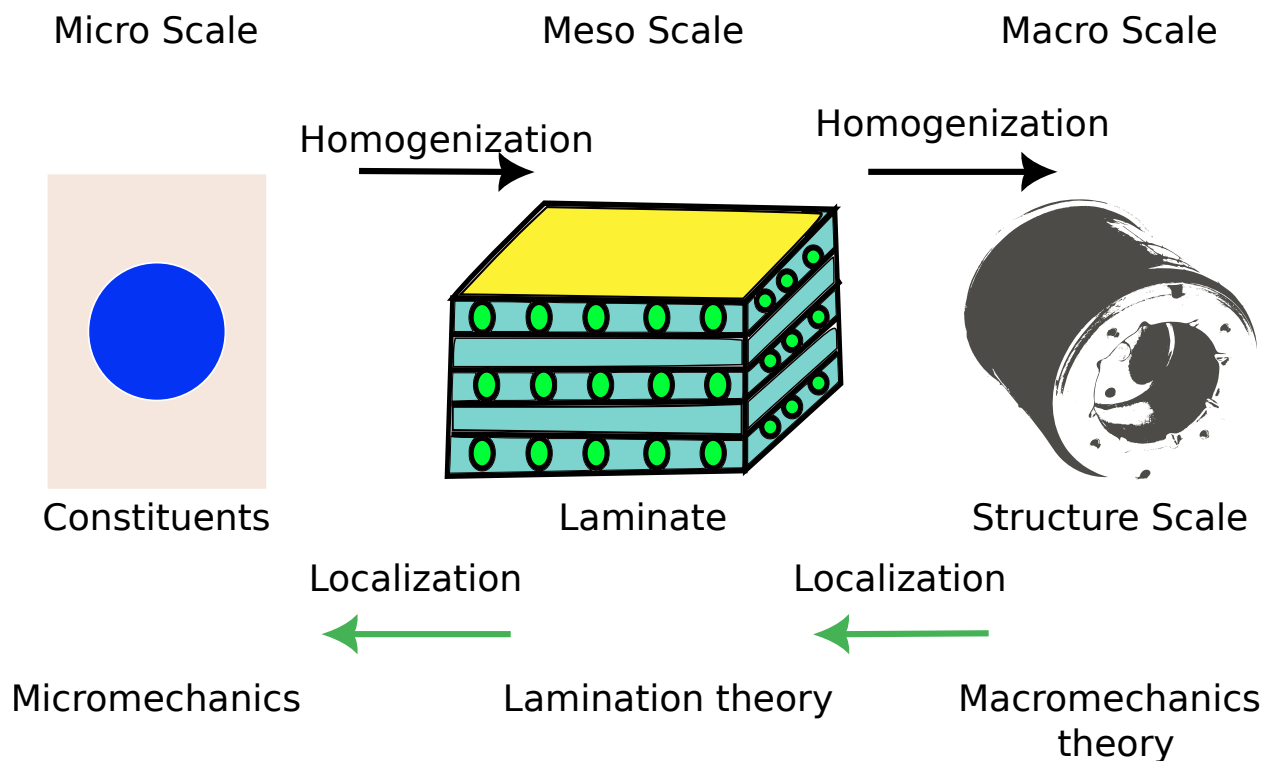
Figure 1.1.2: Illustration of different continuum scales.

element level within the global scale. Each approach has unique requirements for experimental characterization and verification.

In the micro scale approach, models for constituents are used with homogenization to predict composite behavior. The macro scale approach treats the composite as an anisotropic material, with its own experimentally measurable properties, performing the homogenization procedure from the micro scale to the global scale. However, the macromechanical approach's validity depends on the structure and the size of the internal texture of the material, making it unsuitable for certain multiphased materials.

The superiority of the micro or macro scale approach remains debatable concerning the primary goal of developing accurate, computationally efficient, and experimentally validated analysis tools. Each approach has its strengths and weaknesses.

In summary, the macromechanical approach is computationally efficient and incorporates effects like residual stresses and damage. However, it requires anisotropic constitutive theory, constant recalibration for changes in parameters, and is phenomenologically based. On the other hand, the micromechanical approach captures deformation and damage at a more fundamental scale, accommodating changes in parameters, and considering isotropic constitutive models. However, it increases computational expense and requires experimental verification at different scales.

This thesis focuses on micromechanical approaches due to their capability to handle 'what if' scenarios in material design.

1.2   Objectives of thesis

The thesis aims to address various aspects through the utilization of a micromechanical Finite Element Method (FEM) model, implemented using the commercial software ABAQUS. The outcomes of ABAQUS post-processing are subsequently analyzed in MATLAB. The overarching goals of the thesis are outlined as follows:

- Development of a comprehensive framework for achieving computational homogenization.
- Determination of effective material properties through computational homogenization techniques.
- Formulation and development of material models using both strain-based and invariant-based approaches.
- Establishment of a systematic framework for identifying material parameters applicable to diverse models.
- Comparison of obtained results with established theoretical principles and experimental data.
- Code development adhering to PEP-8 standards for enhanced readability and maintainability.

1.3   Contributions

This thesis establishes a comprehensive framework for achieving the numerical homogenization of two-phase materials, integrating seamlessly with the ABAQUS software through a dedicated

plugin. This plugin employs linear perturbation analysis to accomplish homogenization, encompassing various anisotropic scenarios such as monotropy, orthotropy, transverse isotropy, and isotropy.

One of the key contributions is the formulation of an equation (3.3.3) for determining effective properties in the context of linear anisotropy. Validation against a periodic microstructure model demonstrates its accuracy, reinforcing its reliability for practical applications.

Furthermore, the capabilities of the plugin have been extended to handle geometric nonlinearity. Additionally, a robust framework has been devised for the design and testing of diverse material models. To enhance efficiency in parameter determination, a modification to the ADAM algorithm has been incorporated.

In the realm of air springs, a noticeable gap exists in the literature concerning a framework for designing a homogeneous material response. The predominant focus among researchers has been on the Halpin-Tsai homogenization model or incorporating rebar as reinforcement. Furthermore, the common practice in determining material parameters involves comparing only one stress component, often overlooking the comprehensive stress state of the material.

This emphasis on a single stress component is understandable in experimental tests like tensile testing, where stress is typically measured in one direction. However, by adopting the RVE approach to design the material response, all six components of stress can be obtained simultaneously. Surprisingly, a material model that accurately predicts all six stresses concurrently is lacking in the existing literature, based on my knowledge.

To address this gap, my work introduces a novel perspective by comparing all six stresses simultaneously, leading to the formulation of six distinct objective functions for optimization. Rather than resorting to multi-objective optimization techniques, the study employs the ADAM algorithm. Stochastic weights are introduced to all six objective functions, introducing an element of stochasticity into the batched-gradient optimization algorithm. The findings reveal that this modified algorithm outperforms traditional gradient descent methods, providing a more effective approach to optimization in this context.

An intriguing finding during this investigation was the identification of inaccuracies in the equation for Cauchy stress in the invariant-based formulation, as presented in existing sources, including [20] and the Abaqus manual [34]. I have derived corrected equations in the last section of Chapter 2.

In summary, this work offers practical applications and user-friendly tools for homogenization processes, significantly advancing the understanding and implementation of numerical homogenization in the field.

1.4 Structure of thesis

The structure of the thesis unfolds as follows: Chapter 1 presents a succinct introduction to the problem statement, offering insights into the background and motivation. Chapter 2 provides a brief overview of continuum theory and constitutive modeling. In this chapter, the equations for

stress are also derived based on the strain-based approach and also based on the invariant-based approach.

Chapter 3 delves into micromechanics modeling, exploring concepts such as the representative volume element, methods for determining effective properties, periodic structure models, and computational homogenization. It also introduces a dedicated plugin developed for computational homogenization, along with its verification process. This chapter also discusses about the equation which is derived for linear anisotropic model.

Chapter 4 shifts the focus to air springs. It begins with a general introduction to air springs and subsequently details the modeling of the bellow. The chapter encompasses necessary modifications to accommodate material nonlinearity and presents results for various material models developed using either strain-based or invariant-based formulations. Finally, the conclusions and future prospects are discussed in the concluding chapter.

Chapter 2

Theory of Kinematics and Kinetics

In this crucial chapter, we embark on a foundational journey into continuum mechanics. Beginning with a thorough exploration of fundamental principles, we delve into the essence of key concepts, elucidating the meanings of stretch, strain, stress, and the delicate equilibrium governed by balanced laws. Our inquiry extends to the complexities of strain rates, stress rates, and the profound domain of tangents.

Furthermore, this chapter provides a concise overview of constitutive modeling, delving into its generalities. It also delves into the derivation of equations for Cauchy stress within both strain-based and invariant-based formulations. This nuanced exploration lays the groundwork for a profound understanding of the intricate interplay between material behavior and the theoretical frameworks that underpin our study. Subsequently, these theoretical foundations will be applied in the forthcoming chapters.

2.1 Basics of Continuum Mechanics

The world around us is made up of discrete particles. However, it can be assumed continuum at the *macroscopic* view. These quantities are averages over dimensions that are small enough to catch gradients and reflect the microstructural effects. This assumption should be good enough to design engineering elements.

All ideas of continuum mechanics can be derived from the kinematics of the motion, kinetics of forces (stresses) , and fundamental laws of physics. This is power enough to capture the response of all classes of materials, regardless of their internal physical strucutre.

2.1.1 Motions of Continuum Bodies

Let body $\mathcal{B}$ which is made of infinite particles p which makes it continuous occupies a region Ω_0 with a regular boundary $\partial\Omega_0$ at time $t = 0$. This body is embedded into three-dimensional Euclidean space. Under the influence of some external forces, this body body $\mathcal{B}_0$ moves with time t, and it occupies a continuous sequence of geometrical regions denoted by $\Omega_0, \Omega_1, \ldots \Omega_t$.

These regions which is occupied by body $\mathcal{B}$ at a given time is known as *configuration*, as shown in Figure 2.1.1.
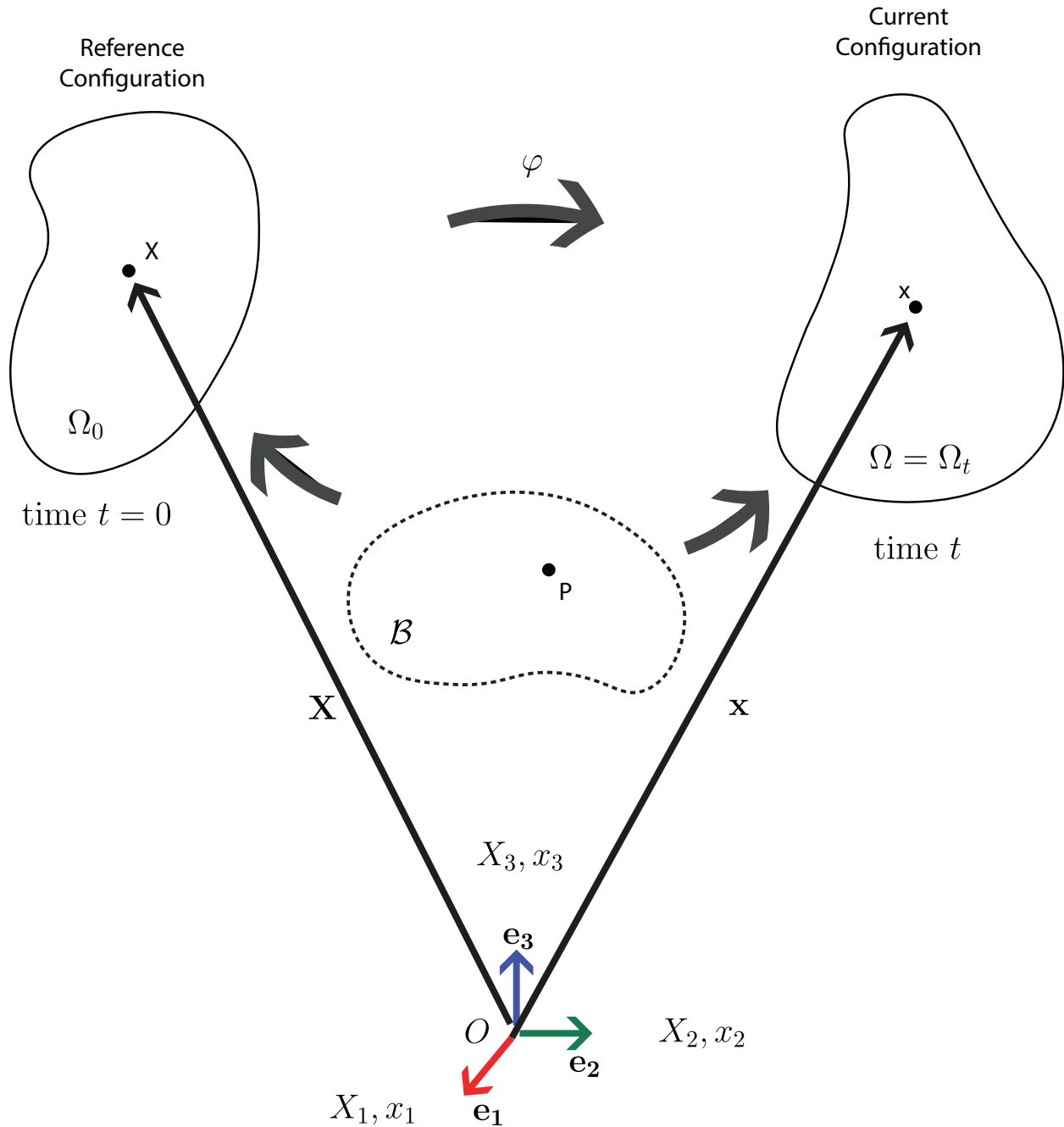
Figure 2.1.1: Configurations and motion φ of continuum body

Two important configurations are known as *reference* configuration and *current* configuration. We assume at reference configuration there is no deformation; consequently, this is also known as *undeformed* or *initial* configuration. Similarly, the configuration for $t > 0$ is known as *current* configuration or *deformed* configuration. The quantities which are defined in reference configu-

ration are denoted by capital letters and which are defined in current configuration are denoted in small case letters.

The next idea is to relate the quantity x in current configuration to the quantity X in the reference configuration. A one-one mapping function φ can be assumed:

$$x = \varphi\,(p) = \varphi\,(X,\mathrm{t})$$

This function φ is a vector field which describes the motion of body $\mathcal{B}$. This function is assumed to be uniquely invertible. In turn, this function can be used to move to current configuration or from current configuration to the reference configuration.

Definition 2.1.1 (Deformation field). *A deformation of Ω_0 is a smooth, one-to-one, orientation-preserving mapping*

$$\varphi\colon \Omega_0 \longrightarrow \Omega_t \qquad\qquad with\ (X,t) \mapsto (x,t) = (\varphi\,(X)\,,t)\,.$$

This mapping relates each point $X \in \Omega_0$ in the reference configuration to a new position $x \in \Omega_t$ at the current configuration.

2.1.1.1 Material and spatial description

To analyze the motion of particle there are two fundamental ways to do it. In one way, we analyze the properties of a particle and moves with it. This way of description is known as *Langrangian description* or *material description*. In this description, the quantities are expressed with respect to the reference configuration. The consistency condition for this description is at $t = 0$, it must $X = x$. This description of motion is more popular in solid mechanics community.

Another way to analyze the particle is to fix your probe and see what happens with quantity with time. This is known as *Eulerian description* or *spatial description*. Here, the quantities are expressed with respect to the current configuration. This description of motion is more common in fluids mechanics community.

Definition 2.1.2 (Material description of a displacement field).

$$U\,(X,t) = x\,(X,t) - X$$

. It relates a typical particle's position X in the undeformed configuration to its position x in the current configuration at time t.

Definition 2.1.3 (Spatial description of a displacement field).

$$u\,(x,t) = x - X\,(x,t)$$

. It defines the current position x at time t, which generates from its referential position $X\,(x,t)$ plus its displacement $u\,(x,t)$ from that position.

It should be noted that the displacement description in both spatial and material are essentially equal.

$$U\,(X,t) = U\left(\varphi^{-1}\,(x,t)\,,t\right) = u\,(x,t)\,.$$

This is also true with velocity and acceleration fields. There are two more important ideas left to introduce. First idea is relating material tangent vector $d\boldsymbol{X}$ in the reference configuration with the spatial tangent vector $d\boldsymbol{x}$, and the other idea is of relating infinitesimal vector area element $d\boldsymbol{S}$ in undeformed configuration with the vector area element $d\boldsymbol{s}$ in the deformed configuration.

Definition 2.1.4 (Deformation gradient). *The line element $d\boldsymbol{x}$ in current configuration can be related with linear mapping $\boldsymbol{F}$ to the line element $d\boldsymbol{X}$ in the reference configuration as,*

$$d\boldsymbol{x} = \boldsymbol{F}(\boldsymbol{X},t)\,d\boldsymbol{X},$$
$$dx_i = F_{iJ}dX_J,$$
$$\boldsymbol{F}(\boldsymbol{X},t) = \frac{\partial\varphi(\boldsymbol{X},t)}{\partial\boldsymbol{X}}$$

where $\boldsymbol{F}(\boldsymbol{X},t)$ is the second order two-point tensor *and known as deformation gradient. This description is defined in material coordinate system.*

Definition 2.1.5 (Determinant of deformation gradient). *The material volume element dV and a spatial volume element dv can be related at a give time t as,*

$$dv = J(\boldsymbol{X},t)\,dV,$$
$$J(\boldsymbol{X},t) = \det(\boldsymbol{F}(\boldsymbol{X},t)),$$
$$J > 0,$$

in which J is the determinant of the deformation gradient $\boldsymbol{F}$, which is also known as volume ratio.

Definition 2.1.6 (Nason's Formula). *Let $d\boldsymbol{s} := \boldsymbol{n}\,ds$ be the vector area element in the current configuration with a unit a normal vector $\boldsymbol{n}$, and let $d\boldsymbol{S} := \boldsymbol{N}dS$ denoting the vector area element in the reference configuration. They can be related as,*

$$d\boldsymbol{s} = J\boldsymbol{F}^{-T}d\boldsymbol{S},$$

where J is the determinant of deformation gradient $\boldsymbol{F}(\boldsymbol{X},t)$.

Proof. $dv = d\boldsymbol{s}\cdot d\boldsymbol{x}$, and $dV = d\boldsymbol{S}\cdot d\boldsymbol{X}$, they can be related by using definition 2.1.5,

$$d\boldsymbol{s}\cdot d\boldsymbol{x} = Jd\boldsymbol{S}\cdot d\boldsymbol{X}.$$

Now by using definition 2.1.4, we can write,

$$d\boldsymbol{s}\cdot d\boldsymbol{x} = d\boldsymbol{s}\cdot(\boldsymbol{F}\cdot d\boldsymbol{X}),$$
$$= (\boldsymbol{F}^T\cdot d\boldsymbol{s})\cdot d\boldsymbol{X},$$

,so,

$$(\boldsymbol{F}^T\cdot d\boldsymbol{s})\cdot d\boldsymbol{X} = Jd\boldsymbol{S}\cdot d\boldsymbol{X},$$
$$(\boldsymbol{F}^T\cdot d\boldsymbol{s} - Jd\boldsymbol{S})\cdot d\boldsymbol{X} = 0$$

, which is true for all values of $d\boldsymbol{X}$ if $\boldsymbol{F}^T\cdot d\boldsymbol{s} - Jd\boldsymbol{S} = 0$, which proves Nason's formula. □

With these definitions two more important ideas of strain and stress are needed to be defined.

2.1.2 Strain

The basic idea of strain is derived from a measure of dimensionless relative motion between two points in a body. To elaborate this idea one can understand it better in one dimension, then later it can be extended to 3 dimensions.

Let's assume two points in 1-D has distance L, and under the influences of some forces their distance is changed to $L + \Delta L$. Thus, we need some kind of function ε which should give 0 which is considered as the *unstrained state* when the length is L, and it should output ΔL when the distance is $L + \Delta L$. This function can be determined by expanding a Taylor series around L.

$$\varepsilon = f(L) + [x - L]\frac{\partial f}{\partial x} + \frac{1}{2}[x - L]^2 \frac{\partial^2 f}{\partial x^2} + \cdots \tag{2.1.1}$$

Now by assuming $f(L) = 0$, we can reach to different approximations of strain by imposing certain conditions on $\frac{\partial f}{\partial x}$.

In literature, instead of using $f(x)$, the $f(\lambda)$ is more common where $\lambda = \frac{\Delta L}{L}$ is a measure of stretch. The idea is instead of using unstrained state as $f(L)$, use $f(1)$ which is a normalized version of f. Consequently, the equation can be written as:

$$\varepsilon = [\lambda - 1]\frac{\partial f}{\partial \lambda} + \frac{1}{2}[\lambda - 1]^2 \frac{\partial^2 f}{\partial \lambda^2} + \cdots \tag{2.1.2}$$

Now by assuming different condition of $\frac{\partial f}{\partial \lambda}$, many different measures are used:

- Nominal (Biot's) strain: $\frac{\partial f}{\partial \lambda} = 1, \frac{\partial^i f}{\partial \lambda^i} \approx 0 \ \forall i > 2, \ \varepsilon(\lambda) = \lambda - 1$
- Logarithmic strain: $\varepsilon(\lambda) = \ln \lambda$
- Green's strain: $\frac{\partial f}{\partial \lambda} = \frac{\partial^2 f}{\partial \lambda^2} = 1, \frac{\partial^i f}{\partial \lambda^i} \approx 0 \ \forall i > 3, \ \varepsilon(\lambda) = 1/2 [\lambda^2 - 1]$

Nominal strain which is some times also called engineering strain is common among engineers who are working with uniaxail specimen. In a uniformly strained uniaxial specimen, where x represents the current length and L denotes the original gauge length, this strain is quantified as $\frac{x}{L} - 1$.

The logarithmic strain measure finds widespread application in the realm of metal plasticity. One rationale behind its prevalence in this context lies in the close alignment of tension, compression, and torsion test results when *true* stress (force per current area) is plotted against log strain. Subsequently, it will become evident that this strain measure holds mathematical relevance for such materials due to the assumption that the elastic component of strain can be considered small.

Green's strain measure proves advantageous computationally in scenarios involving significant motions. This is because, as we will elucidate later, its extension to a strain tensor in any three-dimensional motion can be directly derived from the deformation gradient, bypassing the need to solve for principal stretch ratios and their orientations.

While numerous strain functions can be conceived, the selection ultimately hinges on convenience. Given that strain typically serves as the bridge between kinematic and constitutive theories, the

choice is guided by two key factors in the context of finite elements. Firstly, the ease with which strain can be computed from displacements, as the latter typically constitute the fundamental variables in finite element models. Secondly, the compatibility of the strain measure with the specific constitutive model in play. For instance, as previously noted, log strain emerges as particularly fitting for plasticity, while the analysis of elasticity under large strains (for materials like rubber) can be effectively conducted without recourse to any "strain" measure, except for the stretch ratio.

This idea will now be extended to three dimensions.

2.1.2.1 Strain in three dimensions

The strain measure in three dimensions is derived by the deformation gradient. There are various definitions of strains [19], here only main ones are discussed.

Definition 2.1.7 (Right Cauchy-Green tensor C).

$$\boldsymbol{C} = \boldsymbol{F}^T \cdot \boldsymbol{F} \qquad\qquad C_{IJ} = F_{kI}F_{kJ},$$

C *is the second order, symmetric, and positive definite tensor for all* $\boldsymbol{X} \in \Omega_0$. *This measure is defined for the reference configuration.*

Definition 2.1.8 (Left Cauchy-Green tensor b).

$$\boldsymbol{b} = \boldsymbol{F} \cdot \boldsymbol{F}^T \qquad\qquad b_{ij} = F_{ik}F_{jk},$$

b *is the second order, symmetric, and positive definite tensor for all* $\boldsymbol{X} \in \Omega_t$. *This measure is defined for the current configuration.*

Definition 2.1.9 (Green-Langrange strain tensor E).

$$\boldsymbol{E} = \boldsymbol{\varepsilon}^G = \frac{1}{2}\left(\boldsymbol{C} - \boldsymbol{I}\right) \qquad\qquad E_{IJ} = \frac{1}{2}\left(F_{kI}F_{kJ} - \delta_{IJ}\right),$$

E *or* ε^G *is again the second order, symmetric, and positive definite tensor for all* $\boldsymbol{X} \in \Omega_0$. $\boldsymbol{I}$ *is the second order identity tensor. This measure is defined for the reference configuration.*

Definition 2.1.10 (Linearized Green-Langrange strain tensor $\boldsymbol{E}_{lin}$).

$$\boldsymbol{E}_{lin} = \frac{1}{2}\left(\operatorname{Grad}\boldsymbol{u} + \operatorname{Grad}\boldsymbol{u}^T\right) \qquad\qquad E_{lin\,IJ} = \frac{1}{2}\left(u_{I,J} + u_{J,I}\right),$$

$\boldsymbol{E}_{lin}$ *is again the second order, symmetric, and positive definite tensor for all* $\boldsymbol{X} \in \Omega_0$. $\operatorname{Grad}\boldsymbol{u} := \frac{\partial \boldsymbol{u}}{\partial \boldsymbol{X}}$ *is the second order tensor, and* $\boldsymbol{u}$ *is the displacement vector. This measure is valid for both reference and current configuration because at small strain both configuration are coincident to each other.*

2.1.3 Stretch Tensors

Definition 2.1.11 (Polar Decomposition). *Let* $\boldsymbol{U}$, *and* $\boldsymbol{v}$ *define unique, positive definite, symmetric tensors. Let* $\boldsymbol{R}$ *be a proper orthogonal tensor. For each point* $\boldsymbol{X} \in \Omega_0$, *and at each time* t, *the unique polar decomposition of the deformation gradient* $\boldsymbol{F}$,

$$\boldsymbol{F} = \boldsymbol{R} \cdot \boldsymbol{U} = \boldsymbol{v} \cdot \boldsymbol{R} \qquad\qquad F_{iJ} = R_{iK}U_{KJ} = v_{ik}R_{kJ},$$

U is also called right *(or* material*) stretch tensor, and v is also called* left *(or* spatial*) stretch tensor. It also holds,*

$$U^2 = C,$$
$$v^2 = b,$$

in which C, and b are left and right Cauchy-Green tensors.

The eigen values of U, and v are stretches in the principal direction. We can see from definition 2.1.11 eigen vectors of C, and b are same. Similar observation can be formed for U, and v. However, their eigen vectors are not same. The eigen vectors of U lie in reference configuration, and the eigen vectors of v lie in the current configuration. The U and v in terms of eigen values and eigen vectors can be written as:

$$U = \lambda_I N_I \otimes N_I + \lambda_{II} N_{II} \otimes N_{II} + \lambda_{III} N_{III} \otimes N_{III},$$
$$v = \lambda_I n_I \otimes n_I + \lambda_{II} n_{II} \otimes n_{II} + \lambda_{III} n_{III} \otimes n_{III},$$

where λ_i, $\forall i \in \{I, II, III\}$ are eigen values, also known as principle stretches of U and v. In the same way, N_i, $\forall i \in \{I, II, III\}$, n_i, $\forall i \in \{I, II, III\}$, are eigen vectors and also known as principle directions in the reference and current configurations respectively.

2.1.4   Stress

The concept of stress as it lends itself into the framework of continuum mechanics is described in this section. A natural consequence of deformation in the body, regardless of the particular strain measure being used, is the creation of forces within the internal structure of the body. These forces are said to exist within the 'surfaces' inside the body and can be thought of as arising due to interaction of surfaces of one part of the body with the other. Since these forces arise and act on surfaces within the body, they are described by a concept called *Stress* in continuum mechanics. Similar to different strain measures, stress can also be described in multiple ways.

Definition 2.1.12 (Traction Vector). *Let dA be an area element in the reference configuration, and da be an area element in the current configuration. The traction vector t, and T can be defined as:*

$$t := \lim_{da \to 0} \frac{df}{da},$$
$$T := \lim_{dA \to 0} \frac{df}{dA},$$

in which df is the differential force on the current area element. Both T, and t have the same direction. t is also known as first Piola-Kirchhoff*(or* nominal*) traction vector, which is a measure in the reference configuration. Similarly, t is also known as* Cauchy*(or* true*) traction vector, which is defined for the current configuration.*

Definition 2.1.13 (Cauchy's stress theorem). *For each point $X \in \Omega_0$, and $x \in \Omega_t$, with their traction vectors T, and t, and with their normal vectors N, and n on area elements dA, and*

da, in their reference and current configuration. There exist unique second-order tensor fields $\boldsymbol{P}$, and $\boldsymbol{\sigma}$ for a given time t such that:

$$\boldsymbol{T}\left(\boldsymbol{X},t,\boldsymbol{N}\right)=\boldsymbol{P}\left(\boldsymbol{X},t\right)\cdot\boldsymbol{N}\qquad\qquad T_i=P_{iJ}N_J,$$
$$\boldsymbol{t}\left(\boldsymbol{x},t,\boldsymbol{n}\right)=\boldsymbol{\sigma}\left(\boldsymbol{x},t\right)\cdot\boldsymbol{n}\qquad\qquad t_i=\sigma_{ij}n_j,$$

in which $\boldsymbol{\sigma}$ is called Cauchy*(or* true*)* stress tensor, and $\boldsymbol{P}$ is called first Piola-Kirchhoff*(or* nominal*)* stress tensor.

By using definitions 2.1.13, 2.1.13,

$$\boldsymbol{t}\ da=\boldsymbol{T}\ dA,$$
$$\boldsymbol{\sigma}\cdot\boldsymbol{n}da=\boldsymbol{P}\cdot\boldsymbol{N}dA$$

Now, by using Nason's formula2.1.6,

$$\boldsymbol{\sigma}\cdot\left(J\boldsymbol{F}^{-T}\boldsymbol{N}dA\right)=\boldsymbol{P}\cdot\boldsymbol{N}dA,$$
$$\left(J\boldsymbol{\sigma}\cdot\boldsymbol{F}^{-T}-\boldsymbol{P}\right)\cdot\boldsymbol{N}dA=0,$$

which leads to,

$$\boldsymbol{P}=J\boldsymbol{\sigma}\cdot\boldsymbol{F}^{-T}\qquad\qquad P_{iJ}=J\sigma_{ik}F_{Jk}^{-1}\qquad\qquad(2.1.3)$$

It can be seen that Piola stress is a two-point tensor. Hence, it is not symmetric. There are more important stress measures that need to be discussed.

Definition 2.1.14 (Kirchhoff stress tensor). *The* contravariant *spatial tensor field* $\boldsymbol{\tau}$ *is defined as:*

$$\boldsymbol{\tau}=J\boldsymbol{\sigma}\qquad\qquad\tau_{ij}=J\sigma_{ij},$$

in which J is the volume ratio and determinant of the deformation gradient, and $\boldsymbol{\sigma}$ is the Cauchy stress tensor. It is also a symmetric tensor.

Definition 2.1.15 (Second Piola-Kirchhoff stress tensor). *The* contravariant *material tensor field* $\boldsymbol{S}$ *is defined as:*

$$\boldsymbol{S}=\boldsymbol{F}^{-1}\cdot\boldsymbol{\tau}\cdot\boldsymbol{F}^{-T}\qquad\qquad S_{IJ}=F_{Ik}^{-1}\tau_{kl}F_{Jl}^{-1}.$$

This measure is obtained by the pull-back *operation* $\left(\varphi_*^{-1}\left(\bullet\right)=\boldsymbol{F}^{-1}\cdot\left(\bullet\right)\cdot\boldsymbol{F}^{-T}\right)$ *on* $\boldsymbol{\tau}$, *and it is also a symmetric tensor.*

By using definition 2.1.15, and Equation 2.1.3, we can readily obtain,

$$\boldsymbol{\sigma}=\frac{1}{J}\boldsymbol{F}\cdot\boldsymbol{S}\cdot\boldsymbol{F}^T\qquad\qquad\qquad(2.1.4)$$
$$\boldsymbol{P}=\boldsymbol{F}\cdot\boldsymbol{S}\qquad\qquad\qquad(2.1.5)$$

2.2 Balance Laws

All continuum study follows the *balanced principles*, such as conservation of mass, the momentum balance principles and balance of energy. Moreover, in the thermodynamic framework, it also follows inequalities which are consequence of the second law of thermodynamics. These laws will be summarized in this section.

Definition 2.2.1 (Reynold's transport theorem). *Let $\mathbf{f}$ is a vector valued function, and $\mathbf{v}$ is the velocity of the material area element. Then, the time derivative of function $\mathbf{f}$ under the integral of current configuration Ω_t,*

$$\frac{d}{dt} \int_{\Omega(t)} \mathbf{f} \, dv = \int_{\Omega(t)} \frac{\partial \mathbf{f}}{\partial t} \, dv + \int_{\partial\Omega(t)} (\mathbf{v} \cdot \mathbf{n}) \, \mathbf{f} \, da$$

$$= \int_{\Omega(t)} \frac{\partial \mathbf{f}}{\partial t} + \nabla \cdot (\mathbf{f} \otimes \mathbf{v}) \, dv$$

The proof is given in appendix section A.2.

Definition 2.2.2 (Conservation of mass). *Let ϱ be mass density in the current configuration, then conservation of mass states that during deformation no mass can be produced or taken from the material element or total mass of the material element remains same, mathematically,*

$$\frac{d}{dt} \int_{\Omega_t} \varrho(\boldsymbol{x}, t) \, dv = 0.$$

By using Reynold's transport theorem 2.2.1,

$$\int_{\Omega(t)} \frac{\partial \varrho}{\partial t} + \nabla \cdot (\varrho \mathbf{v}) \, dv = 0$$

Definition 2.2.3 (Linear momentum). *Let $\varrho_0(\boldsymbol{X})$, and $\boldsymbol{V}(\boldsymbol{X}, t)$ be the density and the velocity in the reference configuration, and, $\varrho(\boldsymbol{x})$, and $\boldsymbol{v}(\boldsymbol{x}, t)$ are the density and the velocity in the current configuration, then, the* linear momentum $(\boldsymbol{LM})$*,*

$$\boldsymbol{LM}(t) = \int_{\Omega(t)} \varrho(\boldsymbol{x}, t) \, \boldsymbol{v}(\boldsymbol{x}, t) \, dv,$$

$$= \int_{\Omega_0} \varrho(\boldsymbol{X}, t) \, \boldsymbol{V}(\boldsymbol{X}, t) \, dV.$$

Definition 2.2.4 (Angular momentum). *Let $\varrho_0(\boldsymbol{X})$, and $\boldsymbol{V}(\boldsymbol{X}, t)$ be the density and the velocity in the reference configuration, and, $\varrho(\boldsymbol{x})$, and $\boldsymbol{v}(\boldsymbol{x}, t)$ are the density and the velocity in the current configuration. Let position vector $\boldsymbol{r} := \boldsymbol{x} - \boldsymbol{x}_0$ then, the* angular momentum $(\boldsymbol{AM})$*,*

$$\boldsymbol{AM}(t) = \int_{\Omega(t)} \boldsymbol{r} \times \varrho(\boldsymbol{x}, t) \, \boldsymbol{v}(\boldsymbol{x}, t) \, dv,$$

$$= \int_{\Omega_0} \boldsymbol{r} \times \varrho(\boldsymbol{X}, t) \, \boldsymbol{V}(\boldsymbol{X}, t) \, dV.$$

2.2.1   Conservation of momentum

As per Newton's second law of motion, the net force $\boldsymbol{F}_{net}$, and net torque $\boldsymbol{M}_{net}$ on body is,

$$\frac{d}{dt}\boldsymbol{LM} = \boldsymbol{F}_{net}, \tag{2.2.1}$$

$$\frac{d}{dt}\boldsymbol{AM} = \boldsymbol{M}_{net}. \tag{2.2.2}$$

On the material element there are two kinds of forces that can act upon. One is called volume (or body) forces $\boldsymbol{b}$ such as gravity, and the others are called surface forces $\boldsymbol{t}$, which acts upon boundary of body.

At the current configuration both body and surfaces forces can be added. By using Equation 2.2.1, 2.2.3, 2.2.4,

$$\frac{d}{dt}\int_{\Omega_{(t)}} \varrho\left(\boldsymbol{x},t\right)\boldsymbol{v}\left(\boldsymbol{x},t\right)dv = \int_{\Omega_{(t)}} \boldsymbol{b}dv + \int_{\partial\Omega_{(t)}} \boldsymbol{t}ds,$$

$$\frac{d}{dt}\int_{\Omega_{(t)}} \boldsymbol{r}\times\varrho\left(\boldsymbol{x},t\right)\boldsymbol{v}\left(\boldsymbol{x},t\right)dv = \int_{\Omega_{(t)}} \boldsymbol{r}\times\boldsymbol{b}dv + \int_{\partial\Omega_{(t)}} \boldsymbol{r}\times\boldsymbol{t}ds.$$

By employing Reynold's transport theorem 2.2.1 yields,

$$\int_{\Omega_{(t)}} \frac{\partial}{\partial t}\left(\partial\varrho\left(\boldsymbol{x},t\right)\boldsymbol{v}\left(\boldsymbol{x},t\right)\right) + \nabla\cdot\left(\varrho\left(\boldsymbol{x},t\right)\boldsymbol{v}\left(\boldsymbol{x},t\right)\otimes\boldsymbol{v}\left(\boldsymbol{x},t\right)\right)dv = \int_{\Omega_{(t)}} \boldsymbol{b}dv + \int_{\partial\Omega_{(t)}} \boldsymbol{t}ds,$$

$$\int_{\Omega_{(t)}} \frac{\partial}{\partial t}\left(\boldsymbol{r}\times\varrho\left(\boldsymbol{x},t\right)\boldsymbol{v}\left(\boldsymbol{x},t\right)\right) + \nabla\cdot\left(\boldsymbol{r}\times\varrho\left(\boldsymbol{x},t\right)\boldsymbol{v}\left(\boldsymbol{x},t\right)\otimes\boldsymbol{v}\left(\boldsymbol{x},t\right)\right)dv = \int_{\Omega_{(t)}} \boldsymbol{r}\times\boldsymbol{b}dv + \int_{\partial\Omega_{(t)}} \boldsymbol{r}\times\boldsymbol{t}ds.$$

By using definition 2.1.13, A.1.1 the traction forces $\boldsymbol{t}$,

$$\int_{\partial\Omega_{(t)}} \boldsymbol{t}ds = \int_{\partial\Omega_{(t)}} \left(\boldsymbol{\sigma}\cdot\boldsymbol{n}\right)ds$$

$$= \int_{\Omega_{(t)}} \nabla\cdot\left(\boldsymbol{\sigma}\right)dv$$

Also, by using chain rule on the left hand side of momentum balance equation,

$$\frac{\partial}{\partial t}\left(\varrho\boldsymbol{v}\right) + \nabla\cdot\left(\varrho\boldsymbol{v}\otimes\boldsymbol{v}\right) = \boldsymbol{v}\frac{\partial\varrho}{\partial t} + \varrho\frac{\partial\boldsymbol{v}}{\partial t} + \boldsymbol{v}\left(\nabla\cdot\varrho\boldsymbol{v}\right) + \varrho\boldsymbol{v}\cdot\left(\nabla\boldsymbol{v}\right)$$

$$= \boldsymbol{v}\left(\underbrace{\frac{\partial\varrho}{\partial t} + \left(\nabla\cdot\varrho\boldsymbol{v}\right)}_{=0,\text{conservation of mass}}\right) + \varrho\frac{\partial\boldsymbol{v}}{\partial t} + \varrho\boldsymbol{v}\cdot\left(\nabla\boldsymbol{v}\right)$$

$$= \varrho\frac{\partial\boldsymbol{v}}{\partial t} + \varrho\boldsymbol{v}\cdot\left(\nabla\boldsymbol{v}\right).$$

Therefore,

$$\int_{\Omega_{(t)}} \left(\varrho\frac{\partial\boldsymbol{v}}{\partial t} + \varrho\boldsymbol{v}\cdot\left(\nabla\boldsymbol{v}\right) - \nabla\cdot\boldsymbol{\sigma} - \boldsymbol{b}\right)dv = 0 \tag{2.2.3}$$

By using material derivative A.2.1,

$$\int_{\Omega_{(t)}} \left(\varrho \frac{d\boldsymbol{v}}{dt} - \nabla \cdot \boldsymbol{\sigma} - \boldsymbol{b} \right) dv = 0 \tag{2.2.4}$$

This equation is also known as *Cauchy's first equation of motion.*

A similar treatment can be established for the term $\int_{\partial \Omega} \boldsymbol{r} \times \boldsymbol{t} \, ds$. The details can be found at [19]. Under the condition, if there is no couple involved at the material element, this leads to *Cauchy's second equation of motion*

$$\boldsymbol{\sigma} = \boldsymbol{\sigma}^T, \tag{2.2.5}$$

which tells the symmetry of Cauchy stress tensor.

2.2.2   Balance of Energy

This equation is the consequence of Cauchy's first equation of motion. We need to define first a few definitions, then, it would be easier to explain.

Definition 2.2.5 (Rate of external mechanical work). *The power input on a region Ω_t, at time t, done by the system forces traction and body forces $(\boldsymbol{t}, \boldsymbol{b})$ is defined as,*

$$\mathcal{P}(t) = \int_{\partial \Omega} \boldsymbol{t} \cdot \boldsymbol{v} \, da + \int_{\Omega} \boldsymbol{b} \cdot \boldsymbol{v} \, dv,$$

in which $\boldsymbol{v}$ is the spatial velocity vector, and $\boldsymbol{t} \cdot \boldsymbol{v}$ and $\boldsymbol{b} \cdot \boldsymbol{v}$ are mechanical power per unit current surface a and current volume v, respectively.

Definition 2.2.6 (Kinetic energy). *The kinetic energy $\mathcal{K}$ for a region Ω at time t is given as,*

$$\mathcal{K}(t) = \int_{\Omega} \frac{1}{2} \varrho \boldsymbol{v}^2 dv,$$

where $\boldsymbol{v}^2 = \boldsymbol{v} \cdot \boldsymbol{v}$.

Definition 2.2.7 (Stress power). *For a region Ω at time t, the power response of the stress field $(\mathcal{P}_{int})$ is defined as,*

$$\mathcal{P}_{int}(t) = \int_{\Omega} \boldsymbol{\sigma} : \boldsymbol{d} \, dv,$$

in which $\boldsymbol{d}$ is the symmetric part of $\boldsymbol{l}$ (2.2.12). This is also known as rate of internal mechanical work. *This $\mathcal{P}_{int}(t)$ is also equal to rate of internal energy for a region Ω if there is no thermal power.*

By using definitions [2.2.6, 2.2.72.2.5], the balanced principle in the spatial coordinates can be defined as,

$$\frac{d}{dt} \mathcal{K}(t) + \mathcal{P}_{int}(t) = \mathcal{P}_{ext}(t), \tag{2.2.6}$$

$$\frac{d}{dt} \left(\int_{\Omega} \frac{1}{2} \varrho \boldsymbol{v}^2 dv \right) + \int_{\Omega} \boldsymbol{\sigma} : \boldsymbol{d} \, dv = \int_{\partial \Omega} \boldsymbol{t} \cdot \boldsymbol{v} \, da + \int_{\Omega} \boldsymbol{b} \cdot \boldsymbol{v} \, dv. \tag{2.2.7}$$

If $\frac{d}{dt}\mathcal{K}(t) = 0$, then the problem is called *quasi-static*.

Until now, we considered only the mechanical powers. However, if the system response is also sensitive with change in temperature. We have to take into account thermal energies as well.

Definition 2.2.8 (Thermal power). *Let the rate of thermal work is denoted by $\mathcal{Q}$, and defined in spatial coordinates by,*

$$\mathcal{Q}(t) = \int_{\partial\Omega} q_n \, da + \int_{\Omega} r \, dv,$$

in which q_n is a heat flux, determining heat per unit time and per unit current surface area, and $r := r(\boldsymbol{x}, t)$ denotes a heat source per unit time and per unit current volume.

Heat flux is a measure of rate of heat enters or leaves to the normal of surface, and a heat source is a kind of reservoir that supplies energy in the form of heat.

Definition 2.2.9 (Internal Energy). *For a thermo-mechanical system, the rate of internal energy $\dot{u}$ is defined in spatial coordinates by,*

$$\dot{u} = \mathcal{P}_{int}(t) + \mathcal{Q}(t),$$

which is also known as balance of thermal energy.

Definition 2.2.10 (First law of thermodynamic). *It is the generalization of the balance of energy by adding a thermal power. Consequently, by using balance of energy (2.2.6), and definition of $\dot{u}$ 2.2.9,*

$$\frac{d}{dt}(\mathcal{K}(t) + u) = \mathcal{P}_{ext}(t) + \mathcal{Q}(t)$$

$$\frac{d}{dt}\left(\int_{\Omega}\left(\frac{1}{2}\varrho\boldsymbol{v}^2 + u\right) dv\right) = \int_{\partial\Omega}(\boldsymbol{t}\cdot\boldsymbol{v} + q_n)\, da + \int_{\Omega}(\boldsymbol{b}\cdot\boldsymbol{v} + r)\, dv.$$

It is defined for spatial coordinates.

First law of thermodynamics does not tell the direction of the energy transfer. This is explained through second law of thermodynamics.

2.2.2.1 Second Law of Thermodynamics

This tells that the heat always flows from hotter region to the colder region. To define it mathematically, we need to introduce a new state variable *entropy*.

Definition 2.2.11 (Entropy). *Entropy is a measure of microscopic randomness and disorder. It is denoted as $\eta_C := \eta_c(\boldsymbol{x}, t)$ for the entropy per unit current volume for a time t. The entropy $\mathcal{S}$ for a region Ω, is defined to be*

$$\mathcal{S}(t) = \int_{\Omega} \eta_c(\boldsymbol{x}, t)\, dv.$$

Definition 2.2.12 (Rate of entropy input). *The rate of entropy input $\tilde{Q}$ is defined in a similar manner as the thermal energy was defined.*

$$\tilde{Q} = -\int_{\partial\Omega} \boldsymbol{h} \cdot \boldsymbol{n} \ da + \int_{\Omega} \tilde{r} \ dv,$$

in which $\tilde{r} := \tilde{r}(\boldsymbol{x}, t)$ is a time-dependent scalar field denoting entropy source per unit time and per unit current volume. With $\int_{\Omega} \tilde{r} dv$ measures the total entropy of the source at which entropy is either generated or destroyed for a region Ω. Whereas $\boldsymbol{h} := \boldsymbol{h}(\boldsymbol{x}, t)$ is a vector field, determines the entropy flux defined per unit current suffice area in $\partial\Omega$.

Definition 2.2.13 (Total production of entropy). *The total production of entropy $\Gamma(t)$ is the difference between the rate of change of entropy $\dot{S}$ and the rate of entropy input $\tilde{Q}$.*

$$\Gamma(t) = \dot{S}(t) - \tilde{Q}(t)$$

Definition 2.2.14 (Second law of thermodynamics). *The total entropy production for all thermodynamic processes is never negative,*

$$\Gamma(t) \geq 0,$$

$$\frac{d}{dt}\left(\int_{\Omega} \eta_c(\boldsymbol{x}, t)\right) + \int_{\partial\Omega} \boldsymbol{h} \cdot \boldsymbol{n} \ da - \int_{\Omega} \tilde{r} \ dv \geq 0.$$

The rate of entropy input is closely related with rate of thermal work. In fact, $\boldsymbol{h}$, and $\tilde{r}$ are related with scalar field ϑ which is known as absolute temperature.

$$\boldsymbol{h} = \frac{\boldsymbol{q}}{\vartheta}, \tag{2.2.8}$$

$$\tilde{r} = \frac{r}{\vartheta}. \tag{2.2.9}$$

Inserting these into second law of thermodynamics 2.2.14,

$$\Gamma(t) = \frac{d}{dt}\left(\int_{\Omega} \eta_c(\boldsymbol{x}, t)\right) + \int_{\partial\Omega} \frac{\boldsymbol{q}}{\vartheta} \cdot \boldsymbol{n} \ da - \int_{\Omega} \frac{r}{\vartheta} \ dv \geq 0, \tag{2.2.10}$$

which is also known as the *Clausius-Dauhem inequality* in the spatial description.

2.2.3 Deformation Rates

Deformation rates show how tensor fields change with time. The spatial velocity gradient, for instance, tells how the velocity varies over the spatial domain. There are two possible possible definitions of material and spatial velcoity gradients.

Definition 2.2.15 (Spatial velocity gradient). *It is a derivative of a spatial velocity field $\boldsymbol{v}(\boldsymbol{x}, t)$ with respect to spatial coordinates,*

$$\boldsymbol{l}(\boldsymbol{x}, t) = \frac{\partial \boldsymbol{v}(\boldsymbol{x}, t)}{\partial \boldsymbol{x}} \qquad\qquad l_{ij} = \frac{\partial v_i}{\partial x_j}$$

The spatial field $\boldsymbol{l}$ is in general a non symmetric second-order tensor.

Definition 2.2.16 (Material velocity gradient). *The material time derivative of the deformation gradient $\boldsymbol{F}$ gives the material velocity gradient.*

$$\dot{\boldsymbol{F}}\left(\boldsymbol{X},t\right) = \frac{\partial}{\partial t}\left(\frac{\partial\varphi(\boldsymbol{X},t)}{\partial\boldsymbol{X}}\right)$$
$$= \frac{\partial}{\partial\boldsymbol{X}}\left(\frac{\partial\varphi(\boldsymbol{X},t)}{\partial t}\right)$$
$$= \frac{\partial\boldsymbol{V}\left(\boldsymbol{X},t\right)}{\partial\boldsymbol{X}}$$

The spatial, and material velocity gradients can also be written as $\mathrm{grad}\left(\boldsymbol{v}\left(\boldsymbol{x},t\right)\right)$, $\mathrm{Grad}\left(\boldsymbol{V}\left(\boldsymbol{X},t\right)\right)$, and they can be related to each other by using chain rule,

$$\boldsymbol{l}(\boldsymbol{x},t) = \frac{\partial\boldsymbol{v}(\boldsymbol{x},t)}{\partial\boldsymbol{x}}$$
$$= \frac{\partial}{\partial t}\left(\frac{\partial\varphi(\boldsymbol{X},t)}{\partial\boldsymbol{X}}\right)\cdot\frac{\partial\boldsymbol{X}}{\partial\boldsymbol{x}}$$
$$= \dot{\boldsymbol{F}}\boldsymbol{F}^{-1}\,. \tag{2.2.11}$$

It can be split into symmetric and skew-symmetric parts,

$$\boldsymbol{l} = \boldsymbol{d} + \boldsymbol{w}\,. \tag{2.2.12}$$

The symmetric part, $\boldsymbol{d}$, is known as the *rate of deformation tensor*, while the non-symmetric part, $\boldsymbol{w}$ is known as the *spin tensor* and characterizes the rate of rotation,

$$\boldsymbol{d} = \frac{1}{2}\left[\boldsymbol{l} + \boldsymbol{l}^{\mathrm{T}}\right] \quad \text{and} \quad \boldsymbol{w} = \frac{1}{2}\left[\boldsymbol{l} - \boldsymbol{l}^{\mathrm{T}}\right]\,. \tag{2.2.13}$$

The rate of deformation $\boldsymbol{d}$ can be shown to be the push forward of the time rate of change of the Green-Lagrange strain tensor $\boldsymbol{E}$

$$\dot{\boldsymbol{E}} = \boldsymbol{F}^{\mathrm{T}}\cdot\boldsymbol{d}\cdot\boldsymbol{F}\,. \tag{2.2.14}$$

2.2.4 Stress Rates

2.2.4.1 Truesdell Stress Rates

Tensorial quantities in solid mechanics, including stress and stress rates, must satisfy the criterion of objectivity, which means the quantities must remain unchanged regardless of the position of the observer. The simplest objective stress rate is the Truesdell stress rate, $\boldsymbol{\sigma}^{\circ}$, which is the Piola transformation (push forward) of the time derivative of the second Piola-Kirchhoff stress. Using the expressions

$$\frac{\partial}{\partial t}\boldsymbol{F} = \boldsymbol{l}\cdot\boldsymbol{F}\,, \qquad \frac{\partial}{\partial t}\boldsymbol{F}^{-1} = -\boldsymbol{F}^{-1}\cdot\boldsymbol{l}\,, \qquad \text{and} \qquad \frac{\partial}{\partial t}\boldsymbol{F}^{-\mathrm{T}} = -\boldsymbol{l}^{\mathrm{T}}\cdot\boldsymbol{F}^{-\mathrm{T}}\,, \tag{2.2.15}$$

along with

$$\dot{J} = J \operatorname{div}(\boldsymbol{v}) \qquad \text{and} \qquad \operatorname{div}(\boldsymbol{v}) = \operatorname{tr}(\nabla \boldsymbol{v}) = \operatorname{tr}(\boldsymbol{l}) \,, \tag{2.2.16}$$

the Truesdell stress rate of the Cauchy stress simplifies to

$$\boldsymbol{\sigma}^{\circ} = J^{-1} \boldsymbol{F} \cdot \left[\frac{\partial}{\partial t} \boldsymbol{S} \right] \cdot \boldsymbol{F}^{\mathrm{T}} \tag{2.2.17}$$

$$\cdots$$

$$\boldsymbol{\sigma}^{\circ} = \dot{\boldsymbol{\sigma}} - \boldsymbol{l} \cdot \boldsymbol{\sigma} - \boldsymbol{\sigma} \cdot \boldsymbol{l}^{\mathrm{T}} + \operatorname{tr}(\boldsymbol{l}) \boldsymbol{\sigma} \,. \tag{2.2.18}$$

The Truesdell rate of the Cauchy stress can also be interpreted as the Lie derivative of the Kirchhoff stress; that is,

$$J \boldsymbol{\sigma}^{\circ} = \mathcal{L}_{\phi} (\boldsymbol{\tau}) = \boldsymbol{\tau}^{\circ} = \cdots = \dot{\boldsymbol{\tau}} - \boldsymbol{l} \cdot \boldsymbol{\tau} - \boldsymbol{\tau} \cdot \boldsymbol{l}^{\mathrm{T}} \,. \tag{2.2.19}$$

(Note: Holzapfel defines the Lie derivative of a spatial stress field to be the Oldroyd stress rate, and gives the same definition to the result.)

2.2.4.2 Jaumann Stress Rates

Another important objective stress rate is the Jaumann-Zaremba rate.

$$\boldsymbol{A}^{\nabla} = \dot{\boldsymbol{A}} - \boldsymbol{w} \cdot \boldsymbol{A} + \boldsymbol{A} \cdot \boldsymbol{w} \tag{2.2.20}$$

It is essentially a simplification of the Truesdell stress, assuming only rigid-body rotation ($\boldsymbol{F} = \boldsymbol{R}$); that is, the Truesdell and Jaumann rates of a stress are equivalent if $\boldsymbol{d} = \boldsymbol{0}$.

$$\boldsymbol{\sigma}^{\nabla} = \dot{\boldsymbol{\sigma}} - \boldsymbol{w} \cdot \boldsymbol{\sigma} + \boldsymbol{\sigma} \cdot \boldsymbol{w} \tag{2.2.21}$$

$$\boldsymbol{\tau}^{\nabla} = \dot{\boldsymbol{\tau}} - \boldsymbol{w} \cdot \boldsymbol{\tau} + \boldsymbol{\tau} \cdot \boldsymbol{w} \tag{2.2.22}$$

The Jaumann stress is used because it is easy to deal with, and leads to a symmetric tangent.

2.2.4.3 Relations Between Stress Rates

The Jaumann stress is related to the Truesdell stress by:

$$\begin{aligned} \boldsymbol{\tau}^{\circ} &= \dot{\boldsymbol{\tau}} - \boldsymbol{l} \cdot \boldsymbol{\tau} - \boldsymbol{\tau} \cdot \boldsymbol{l}^{\mathrm{T}} \\ &= \dot{\boldsymbol{\tau}} - [\boldsymbol{d} + \boldsymbol{w}] \cdot \boldsymbol{\tau} - \boldsymbol{\tau} \cdot [\boldsymbol{d} + \boldsymbol{w}]^{\mathrm{T}} \\ &= \dot{\boldsymbol{\tau}} - \boldsymbol{d} \cdot \boldsymbol{\tau} - \boldsymbol{w} \cdot \boldsymbol{\tau} - \boldsymbol{\tau} \cdot \boldsymbol{d}^{\mathrm{T}} - \boldsymbol{\tau} \cdot \boldsymbol{w}^{\mathrm{T}} \\ &= \dot{\boldsymbol{\tau}} - \boldsymbol{d} \cdot \boldsymbol{\tau} - \boldsymbol{w} \cdot \boldsymbol{\tau} - \boldsymbol{\tau} \cdot \boldsymbol{d} + \boldsymbol{\tau} \cdot \boldsymbol{w} \\ &= \underbrace{\dot{\boldsymbol{\tau}} - \boldsymbol{w} \cdot \boldsymbol{\tau} + \boldsymbol{\tau} \cdot \boldsymbol{w}}_{\boldsymbol{\tau}^{\nabla}} - \boldsymbol{d} \cdot \boldsymbol{\tau} - \boldsymbol{\tau} \cdot \boldsymbol{d} \end{aligned}$$

$$\boldsymbol{\tau}^{\circ} = \boldsymbol{\tau}^{\nabla} - \boldsymbol{d} \cdot \boldsymbol{\tau} - \boldsymbol{\tau} \cdot \boldsymbol{d} \tag{2.2.24}$$

The four stress rates introduced here are related by:

$$\boxed{\boldsymbol{\sigma}^{\circ} = \mathcal{L}_{\phi}\left(\boldsymbol{\sigma}\right) = \dot{\boldsymbol{\sigma}} - \boldsymbol{l} \cdot \boldsymbol{\sigma} - \boldsymbol{\sigma} \cdot \boldsymbol{l}^{\mathrm{T}} + \mathrm{tr}(\boldsymbol{l})\boldsymbol{\sigma}} \xrightarrow{\boldsymbol{\sigma}^{\nabla} = \boldsymbol{\sigma}^{\circ}|_{d=0}} \boxed{\boldsymbol{\sigma}^{\nabla} = \dot{\boldsymbol{\sigma}} - \boldsymbol{w} \cdot \boldsymbol{\sigma} + \boldsymbol{\sigma} \cdot \boldsymbol{w}}$$

$$\boldsymbol{\tau}^{\circ} = J\boldsymbol{\sigma}^{\circ}$$

$$\boxed{\boldsymbol{\tau}^{\circ} = \mathcal{L}_{\phi}\left(\boldsymbol{\tau}\right) = \dot{\boldsymbol{\tau}} - \boldsymbol{l} \cdot \boldsymbol{\tau} - \boldsymbol{\tau} \cdot \boldsymbol{l}^{\mathrm{T}}} \xrightarrow{\boldsymbol{\tau}^{\nabla} = \boldsymbol{\tau}^{\circ}|_{d=0}} \boxed{\boldsymbol{\tau}^{\nabla} = \dot{\boldsymbol{\tau}} - \boldsymbol{w} \cdot \boldsymbol{\tau} + \boldsymbol{\tau} \cdot \boldsymbol{w}}$$
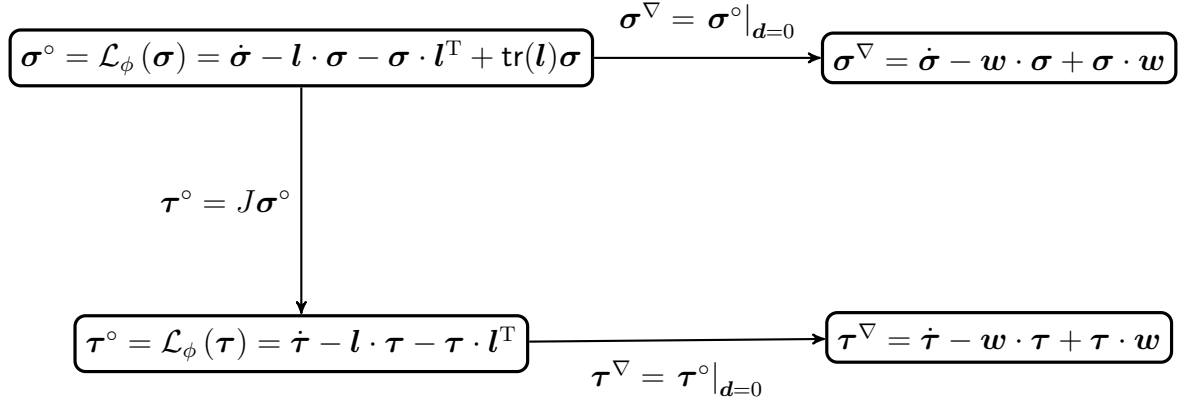
For more information on stress rates, see Bonet & Wood, p152, or Holzapfel, p192.

2.2.5 Tangents

Tangents relate the change in stress (or stress rate) to the change in strain (or strain rate).

2.2.5.1 Lagrangian Elasticity Tensor

The Lagrangian elasticity tensor or tangent arises from the linearization of the stress,

$$D\boldsymbol{S}_{IJ} = \left. \frac{\partial}{\partial \varepsilon} \left(\boldsymbol{S}_{IJ}\left(\boldsymbol{E}(\boldsymbol{u} + \varepsilon \boldsymbol{\delta u}) \right) \right) \right|_{\varepsilon=0} \tag{2.2.25}$$

$$= \left. \frac{\partial \boldsymbol{S}_{IJ}}{\partial \boldsymbol{E}_{KL}} \frac{\partial}{\partial \varepsilon} \boldsymbol{E}_{KL}(\boldsymbol{u} + \varepsilon \boldsymbol{\delta u}) \right|_{\varepsilon=0}$$

$$= \frac{\partial \boldsymbol{S}_{IJ}}{\partial \boldsymbol{E}_{KL}} D\boldsymbol{E}_{KL}(\boldsymbol{u})$$

$$D\boldsymbol{S}_{IJ} = \mathsf{C}_{IJKL} D\boldsymbol{E}_{KL}(\boldsymbol{u}). \tag{2.2.26}$$

Thus we have the Lagrangian elasticity tensor,

$$\mathsf{C}_{IJKL} = \frac{\partial \boldsymbol{S}_{IJ}}{\partial \boldsymbol{E}_{KL}} = 2\frac{\partial \boldsymbol{S}_{IJ}}{\partial \boldsymbol{C}_{KL}}, \tag{2.2.27}$$

which has both minor symmetries but not necessarily major symmetry.

2.2.5.2 Eulerian Elasticity Tensor

The spatial equivalent is "intractable" so instead the rate form is used. (Essentially, the terms $\boldsymbol{S}$ and $\boldsymbol{E}$ can be linearized in the direction of $\boldsymbol{v}$ instead of $\boldsymbol{u}$.) This is done using the fact that the time derivative of the second Piola-Kirchhoff stress is the pull back of the Truesdell stress rate and the time derivative of the Green-Lagrange strain tensor is the pull back of the rate of deformation,

$$\dot{\boldsymbol{S}} = \boldsymbol{F}^{-1} \cdot \boldsymbol{\tau}^{\circ} \cdot \boldsymbol{F}^{-\mathrm{T}} = J\boldsymbol{F}^{-1} \cdot \boldsymbol{\sigma}^{\circ} \cdot \boldsymbol{F}^{-\mathrm{T}} \quad \text{and} \quad \dot{\boldsymbol{E}} = \boldsymbol{F}^{\mathrm{T}} \cdot \boldsymbol{d} \cdot \boldsymbol{F}. \tag{2.2.28}$$

Thus,

$$\dot{S}_{IJ} = \mathbf{C}_{IJKL}\dot{E}_{KL} \tag{2.2.29}$$

$$\mathbf{F}_{Ii}^{-1}\tau_{ij}^{\circ}\mathbf{F}_{Jj}^{-1} = \mathbf{C}_{IJKL}\mathbf{F}_{kK}d_{kl}\mathbf{F}_{lL}$$

$$\tau_{ij}^{\circ} = \underbrace{\mathbf{C}_{IJKL}\mathbf{F}_{iI}\mathbf{F}_{jJ}\mathbf{F}_{kK}\mathbf{F}_{lL}}_{J\mathbf{c}_{ijkl}}d_{kl}$$

$$\tau_{ij}^{\circ} = J\mathbf{c}_{ijkl}d_{kl} \tag{2.2.30}$$

$$\sigma_{ij}^{\circ} = \mathbf{c}_{ijkl}d_{kl}\,, \tag{2.2.31}$$

and the Eulerian elasticity tensor is defined as

$$\mathbf{c}_{ijkl} = \frac{1}{J}\mathbf{C}_{IJKL}\mathbf{F}_{iI}\mathbf{F}_{jJ}\mathbf{F}_{kK}\mathbf{F}_{lL} \qquad \text{or} \qquad \mathbf{c} = \frac{1}{J}\left[\mathbf{F}\overline{\otimes}\mathbf{F}\right] : \mathbf{C} : \left[\mathbf{F}^{\mathrm{T}}\overline{\otimes}\mathbf{F}^{\mathrm{T}}\right]\,, \tag{2.2.32}$$

which similarly has both minor symmetries but not necessarily major symmetry.

2.2.5.3 Jaumann Elasticity Tensor

The objective stress rate used by Abaqus is actually the Jaumann stress rate instead of the Truesdell stress rate, given by:

$$C^{\mathrm{Abaqus}} = \frac{1}{J}\frac{\partial\Delta\left(J\boldsymbol{\sigma}\right)}{\partial\Delta\varepsilon} \tag{2.2.33}$$

The format of the elasticity tensor can be found using the relationship between the two stress rates,

$$\boldsymbol{\tau}^{\circ} = J\mathbf{c} : \boldsymbol{d} \tag{2.2.34}$$

$$\boldsymbol{\tau}^{\nabla} - \boldsymbol{d}\cdot\boldsymbol{\tau} - \boldsymbol{\tau}\cdot\boldsymbol{d} = J\mathbf{c} : \boldsymbol{d}$$

$$\boldsymbol{\tau}^{\nabla} = J\mathbf{c} : \boldsymbol{d} + \boldsymbol{d}\cdot\boldsymbol{\tau} + \boldsymbol{\tau}\cdot\boldsymbol{d}$$

$$\boldsymbol{\tau}^{\nabla} = J\left[\mathbf{c} : \boldsymbol{d} + \boldsymbol{d}\cdot\boldsymbol{\sigma} + \boldsymbol{\sigma}\cdot\boldsymbol{d}\right]\,. \tag{2.2.35}$$

We are seeking a tangent that will satisfy the equation

$$\boldsymbol{\tau}^{\nabla} = J\mathbf{c}^{\mathrm{Abaqus}} : \boldsymbol{d}\,. \tag{2.2.36}$$

That is,

$$J\mathbf{c}^{\mathrm{Abaqus}} : \boldsymbol{d} = J\left[\mathbf{c} : \boldsymbol{d} + \boldsymbol{d}\cdot\boldsymbol{\sigma} + \boldsymbol{\sigma}\cdot\boldsymbol{d}\right]$$

$$\mathbf{c}^{\mathrm{Abaqus}} : \boldsymbol{d} = \mathbf{c} : \boldsymbol{d} + \boldsymbol{d}\cdot\boldsymbol{\sigma} + \boldsymbol{\sigma}\cdot\boldsymbol{d}$$

$$\mathbf{c}^{\mathrm{Abaqus}} : \boldsymbol{d} = \left[\mathbf{c} + \mathbf{c}'\right] : \boldsymbol{d}\,, \tag{2.2.37}$$

where $\mathbf{c}'$ is some fourth-order tangent that satisfies

$$\mathbf{c}' : \boldsymbol{d} = \boldsymbol{d}\cdot\boldsymbol{\sigma} + \boldsymbol{\sigma}\cdot\boldsymbol{d}\,. \tag{2.2.38}$$

Because the double contraction with a symmetric tensor is not unique, there are an infinite number of tensors that could satisfy this. We restrict this further by requiring major and minor symmetries and find the form to be

$$\mathbf{c}'_{ijkl} = \frac{1}{2} \left[\delta_{ik}\sigma_{jl} + \delta_{il}\sigma_{jk} + \delta_{jk}\sigma_{il} + \delta_{jl}\sigma_{ik} \right] \tag{2.2.39}$$

$$\mathbf{c}' = \frac{1}{2} \left[\boldsymbol{I}\overline{\otimes}\boldsymbol{\sigma} + \boldsymbol{I}\underline{\otimes}\boldsymbol{\sigma} + \boldsymbol{\sigma}\underline{\otimes}\boldsymbol{I} + \boldsymbol{\sigma}\overline{\otimes}\boldsymbol{I} \right] \tag{2.2.40}$$

$$\mathbf{c}' = \begin{bmatrix} 2\sigma_1 & 0 & 0 & \sigma_4 & \sigma_5 & 0 \\ & 2\sigma_2 & 0 & \sigma_4 & 0 & \sigma_6 \\ & & 2\sigma_3 & 0 & \sigma_5 & \sigma_6 \\ & & & \frac{1}{2}(\sigma_1 + \sigma_2) & \frac{1}{2}\sigma_6 & \frac{1}{2}\sigma_5 \\ & sym. & & & \frac{1}{2}(\sigma_1 + \sigma_3) & \frac{1}{2}\sigma_4 \\ & & & & & \frac{1}{2}(\sigma_2 + \sigma_3) \end{bmatrix} , . \tag{2.2.41}$$

This extra term, the geometric tangent, can be reduced to purely kinematic terms. Thus we have the Abaqus tangent [31, 9],

$$\mathbf{c}^{\mathsf{Abaqus}} = \mathbf{c} + \mathbf{c}' , \tag{2.2.42}$$

which relates the volume-normalized Jaumann rate of the Kirchhoff stress to the symmetric rate of deformation tensor,

$$\frac{1}{J}\boldsymbol{\tau}^{\nabla} = \mathbf{c}^{\mathsf{Abaqus}} : \boldsymbol{d} . \tag{2.2.43}$$

2.3 Constitutive Modeling

The state of a thermo-mechanical system can be characterized using a set of parameters, including velocity ($\boldsymbol{v}$), stress tensor ($\boldsymbol{\sigma}$), mass density (ϱ), internal energy per unit current volume (u), temperature (ϑ), heat flux vector per unit volume ($\boldsymbol{q}$), and entropy per unit current volume (η_c). By virtue of law of conservation of angular momentum, the number of unknowns needed to solve a thermo-mechanical continuum reduces to 16. To describe any continuum body, whether solid or fluid, we rely on balance laws, which provide five essential equations (mass conservation: 1, linear momentum conservation: 3, first law of thermodynamics: 1). The remaining 11 equations are established through constitutive modelling. Specifically, we require six constitutive equations for stress ($\boldsymbol{\sigma}$), one for internal energy (u), three for heat flux ($\boldsymbol{q}$), and one for entropy (η_c). These constitutive equations play a crucial role in differentiating the response of materials. While the balance laws apply universally to any continuum matter, the material-specific responses are determined by the constitutive relations.

Material response, in particular, pertains to how stress evolves in response to a given strain. Constitutive equations articulate this relationship, which may be time-dependent or time-invariant. For instance, in elastic materials, such as those described by Hooke's law, stress varies linearly in proportion to applied strain, with a material constant like Young's modulus governing this relationship. Hooke's law serves as a constitutive model for elastic materials.

Constitutive models encompass mathematical equations that describe the interplay between stress and strain for a broad spectrum of material behaviors. Given the diversity of material phenomena

in the natural world, developing constitutive models demands extensive research and understanding.

This section's specific focus is on hyperelastic materials. Hyperelasticity characterizes materials in which stress relies solely on the initial and final states of the material, with no dependence on the intermediate states. Hyperelastic behavior is path-independent, meaning it is free from dissipative effects like plasticity and viscosity.

In engineering, instead of directly measuring internal energy, we rely on specific thermodynamic potentials to assess it. For a controlled process where both pressure and volume are regulated, a widely used potential is the *Helmholtz free energy* Ψ. This is obtained through a mathematical operation known as a Legendre transformation [40] on the internal energy. The Helmholtz free energy is particularly prominent in the field of constitutive theory, where it is employed to model the elastic response of materials.

In hyperelastic materials, stress response is contingent on a scalar-valued energy function, commonly referred to as Helmholtz free energy function, and it is independent of the loading path. Additionally, this type of modeling does not account for effects related to strain rate.

Constitutive modeling is quite an extensive topic, the details about this modeling can be found at Kollar and Springer, Truesdell et al., Ball, Paolucci, Holzapfel. However a short summary is presented here as:

- Principle of objectivity: This condition ensures that the strain energy function, denoted as Ψ remains independent of the choice of frame of reference. In other words, for any orthogonal second-order tensor $\boldsymbol{Q}$, the following relationship must hold:

$$\Psi\left(\bullet\right) = \Psi\left(Q\left(\bullet\right)\right) = Q\Psi\left(\bullet\right)Q^{T}.$$

- Normalization condition: The stress-free condition stipulates that stress should be zero in the reference configuration, which is expressed as:

$$\Psi\left(\boldsymbol{I}\right) = 0,$$

here, $\boldsymbol{I}$ represents the second-order identity tensor.

- Growth condition: This condition is relevant for finite strains and states that as the volume ratio approaches infinity or approaches zero (incompressible material) from a positive direction, the strain energy function must tend towards positive infinity. Mathematically, this can be represented as:

$$\lim_{\det \boldsymbol{F} \to +\infty} \Psi\left(\boldsymbol{F}, \boldsymbol{X}\right) \longrightarrow +\infty,$$
$$\lim_{\det \boldsymbol{F} \to 0^{+}} \Psi\left(\boldsymbol{F}, \boldsymbol{X}\right) \longrightarrow +\infty,$$

where $\det \boldsymbol{F}$ denotes the determinant of the deformation gradient tensor $\boldsymbol{F}$.

- Polyconvexity: This condition addresses the existence of a global minimum for the free strain energy function Ψ. It requires that, for any second-order tensor $\mathcal{H}$, the following inequalities are satisfied:

$$\mathcal{H} : \frac{\partial^2 \Psi}{\partial \boldsymbol{F} \partial \boldsymbol{F}} : \mathcal{H} \geq 0,$$

$$\mathcal{H} : \frac{\partial^2 \Psi}{\partial \mathrm{cof}\, \boldsymbol{F} \partial \mathrm{cof}\, \boldsymbol{F}} : \mathcal{H} \geq 0,$$

here, $\mathrm{cof}\, \boldsymbol{F}$ represents the cofactors of the deformation gradient tensor $\boldsymbol{F}$.

There are two main approaches to model this strain energy potential: *strain-based* and *invariant-based*, which will be discussed in the next section.

2.3.1 Strain-Based Formulation

In the strain-based approach, the strain energy density function Ψ is expressed in terms of a suitable strain measure, such as Green's strain ε^G in the reference configuration:

$$\Psi = \Psi(\varepsilon^G)$$

This expression can be further decomposed into its deviatoric and volumetric parts:

$$\Psi = \Psi\left(\bar{\varepsilon}^G, J\right)$$

Here, $\bar{\varepsilon}^G$ represents the modified Green's tensor defined as $\bar{\varepsilon}^G = \frac{1}{2}\left(\bar{\boldsymbol{C}} - \boldsymbol{I}\right)$, where $\bar{\boldsymbol{C}} = J^{-\frac{2}{3}}\boldsymbol{C}$ is the deviatoric part of the right Cauchy-Green strain tensor, $\boldsymbol{C} = \boldsymbol{F}^T \cdot \boldsymbol{F}$. Additionally, $J = \|\boldsymbol{F}\|$ denotes the volume change.

A crucial assumption within this approach is that the preferred material directions are initially aligned with the orthogonal coordinate system in the reference configuration. These directions may become non-orthogonal in the deformed state or the current configuration.

Examples of this approach include the Saint-Venant Kirchhoff model, represented as $\Psi = \frac{1}{2}\varepsilon^G :$ $\boldsymbol{C}^* : \varepsilon^G$, and the generalized Fung-type form, given as $\Psi = \frac{c}{2}\left(e^Q - 1\right) + \frac{1}{D}\left(\frac{J^2-1}{2} - \ln J\right)$, where $Q = \bar{\varepsilon}^G : \boldsymbol{C}^* : \bar{\varepsilon}^G$, and c, D, and $\boldsymbol{C}^*$ are material parameters.

The variation in Ψ can be expressed as:

$$\delta\Psi = \bar{\boldsymbol{F}} \cdot \frac{\partial\Psi}{\partial\bar{\varepsilon}^G} \cdot \bar{\boldsymbol{F}}^T : \delta\boldsymbol{e} + \frac{\partial\Psi}{\partial J}\delta J$$

Here, $\delta\boldsymbol{e} := \delta\boldsymbol{d} - \frac{1}{3}\delta\varepsilon^{vol}\boldsymbol{I}$ represents the *virtual deviatoric strain rate*, and $\boldsymbol{l}$ is the spatial velocity gradient as defined in 2.2.15. The variation in J can also be expressed in terms of $\boldsymbol{l}$, as $\dot{J} = J\mathrm{tr}\left(\boldsymbol{l}\right)$, which further simplifies to $\delta J = J\mathrm{tr}\left(\delta\boldsymbol{d}\right)$, where $\boldsymbol{d}$ is the symmetric part of $\boldsymbol{l}$ and is known as the rate of deformation tensor, as defined in 2.2.13. Moreover, $\bar{\boldsymbol{F}} = J^{-\frac{1}{3}}\boldsymbol{F}$ represents the distortional

part of the deformation gradient. The virtual rate of change of volume per the current volume (*virtual volumetric strain rate*) is denoted as $\delta\varepsilon^{vol} := \mathrm{tr}\,(\delta\boldsymbol{d})$.

The variation in Ψ can be expressed as:

$$\delta\Psi = \bar{\boldsymbol{F}} \cdot \frac{\partial\Psi}{\partial\bar{\boldsymbol{\varepsilon}}^G} \cdot \bar{\boldsymbol{F}}^T : \delta\boldsymbol{e} + \frac{\partial\Psi}{\partial J} J \delta\varepsilon^{vol} \tag{2.3.1}$$

This variation in the strain energy potential is employed in the principle of virtual work as:

$$\delta W = \int_V \delta\Psi\ dv = \int_{V^0} J\left(\tilde{\boldsymbol{\sigma}} : \delta\boldsymbol{e} - p\delta\varepsilon^{vol}\right)\ dV^0 \tag{2.3.2}$$

Here, $\boldsymbol{\sigma}$ represents the Cauchy stress, and $p = -\frac{1}{3}\mathrm{trace}\{\boldsymbol{\sigma}\}$ is the hydrostatic part of the Cauchy stress tensor.

By comparing Equation 2.3.2 with Equation 2.3.1, we can establish the following relationships:

$$\tilde{\boldsymbol{\sigma}} = \frac{1}{J}\mathrm{DEV}\left(\bar{\boldsymbol{F}} \cdot \frac{\partial\Psi}{\partial\bar{\boldsymbol{\varepsilon}}^G} \cdot \bar{\boldsymbol{F}}^T\right)$$

$$p = -\frac{\partial\Psi}{\partial J}$$

In these equations, $\boldsymbol{\sigma} = \tilde{\boldsymbol{\sigma}} - p\boldsymbol{I}$.

2.3.2   Invariant based formulation

Another intriguing approach is the invariant-based formulation, rooted in the theory of fiber-reinforced composites developed by Spencer [38]. This method expresses the strain energy in terms of the invariants of the deformation tensor and fiber directions. Suppose there are N fibers within the composite material,influencing its response along N different directions. These fibers can be represented by unit vectors $\boldsymbol{A}_\alpha$ where $\alpha = 1, \ldots, N$ denotes fiber number, in the reference configuration. The Helmholtz free energy function Ψ can be formulated as:

$$\Psi = \Psi(\boldsymbol{C}, \boldsymbol{A}_\alpha) \qquad\qquad \alpha = 1, \ldots, N.$$

Based on the principle of objectivity, the material's strain must remain unchanged when both the matrix and fibers undergo rigid body rotations. Spencer proposed that the strain energy can be expressed as an isotropic function of an irreducible set of scalar invariants that form the integrity basis of the tensor $\boldsymbol{C}$ and the vectors $\boldsymbol{A}_\alpha$.

$$\Psi = \Psi\left(\bar{I}_1, \bar{I}_2, \bar{I}_3, \bar{I}_{4_{(\alpha\beta)}}, \bar{I}_{5_{(\alpha\beta)}}\right), \qquad\qquad \alpha = 1, \ldots, N; \beta = 1, \ldots, \alpha. \tag{2.3.3}$$

Where:

- $\bar{I}_1, \bar{I}_2$ are the first and second principal invariants of $\bar{b}$.

- $\bar{I}_3 = J$ represents the volume ratio, and J is the measure of volume change.

- $\bar{I}_{4(\alpha\beta)}$ and $\bar{I}_{5(\alpha\beta)}$ are pseudo-invariants of $\bar{C}$, defined as:

$$
\begin{aligned}
\bar{I}_1 &= \mathrm{tr}\left(\bar{b}\right) \\
\bar{I}_2 &= \frac{1}{2}\left(\bar{I}_1^2 - \mathrm{tr}\left(\bar{b}\cdot\bar{b}\right)\right) \\
I_3 &= J = \|\boldsymbol{F}\| \\
\bar{I}_{4_{(\alpha\beta)}} &= \boldsymbol{A}_\alpha \cdot \bar{\boldsymbol{C}} \cdot \boldsymbol{A}_\beta && \alpha = 1,\dots,N; \beta = 1,\dots,\alpha && (2.3.4) \\
\bar{I}_{5_{(\alpha\beta)}} &= \boldsymbol{A}_\alpha \cdot \bar{\boldsymbol{C}}^2 \cdot \boldsymbol{A}_\beta && \alpha = 1,\dots,N; \beta = 1,\dots,\alpha \\
\bar{\xi}_{(\alpha\beta)} &= \boldsymbol{A}_\alpha \cdot \boldsymbol{A}_\beta && \alpha = 1,\dots,N; \beta = 1,\dots,\alpha
\end{aligned}
$$

Here, $\bar{b} = \bar{F} \cdot \bar{F}^T$ is the distortional part of the left Cauchy-Green strain tensor, and $\bar{\xi}_{(\alpha\beta)}$ represents geometrical constants equal to the cosine of the angle between the directions of any two families of fibers in the reference configuration.

One of the main advantages of the invariant-based approach is that it doesn't require the fibers in the reference configuration to be orthogonal to each other. Examples of this type of potential function include the Holzapfel-Gasser-Ogden (HGO) form [20].

The variation in Ψ can be expressed as:

$$
\delta\Psi = \frac{\partial\Psi}{\partial\bar{I}_1}\delta\bar{I}_1 + \frac{\partial\Psi}{\partial\bar{I}_2}\delta\bar{I}_2 + \frac{\partial\Psi}{\partial J}\delta J + \sum_{\alpha=1}^{N}\sum_{\beta=1}^{\alpha}\left(\frac{\partial\Psi}{\partial\bar{I}_{4_{(\alpha\beta)}}}\delta\bar{I}_{4_{(\alpha\beta)}} + \frac{\partial\Psi}{\partial\bar{I}_{5_{(\alpha\beta)}}}\delta\bar{I}_{5_{(\alpha\beta)}}\right) \qquad (2.3.5)
$$

Before calculating variations of invariants, we have to develop derivatives of invariants with respect to $\boldsymbol{b}$ and $\boldsymbol{C}$. In the following, the derivatives $\frac{\partial I_i}{\partial\boldsymbol{b} \text{ or } \partial\boldsymbol{C}}$ will be calculated. Then the relationship between $\bar{I}_i$ and I_i will be established. Thereafter, the time derivatives of $\boldsymbol{b}$ and $\boldsymbol{C}$ will be expressed. Finally, the variations of $\delta\bar{I}_i$ will be derived, and then will be used to derive the relationship of Cauchy stress $\boldsymbol{\sigma}$.

$$
\frac{\partial I_1}{\partial\boldsymbol{b}} = \frac{\boldsymbol{I} : \boldsymbol{b}}{\partial\boldsymbol{b}} = \boldsymbol{I} \qquad\qquad\qquad \frac{\partial I_1}{b_{ij}} = \delta_{ij}
$$

$$
\begin{aligned}
\frac{\partial I_2}{\partial\boldsymbol{b}} &= \frac{1}{2}\frac{\partial}{\partial\boldsymbol{b}}\left(\mathrm{tr}\left(\boldsymbol{b}\right)^2 - \mathrm{tr}\left(\boldsymbol{b}\cdot\boldsymbol{b}\right)\right) \\
&= \frac{1}{2}\left(2\mathrm{tr}\left(\boldsymbol{b}\right)\boldsymbol{I} - 2\boldsymbol{b}\right) \\
&= I_1\boldsymbol{I} - \boldsymbol{b} \qquad\qquad\qquad\qquad \frac{\partial I_2}{b_{ij}} = I_1\delta_{ij} - b_{ij}
\end{aligned}
$$

$$\frac{\partial J}{\partial \boldsymbol{b}} = \frac{J}{2}\boldsymbol{b}^{-1} \qquad\qquad \frac{\partial J}{b_{ij}} = \frac{1}{2}b_{ij}^{-1}$$

For $N = 1$,

$$\frac{\partial I_4}{\partial \boldsymbol{C}} = \boldsymbol{A}_1 \otimes \boldsymbol{A}_1 \qquad\qquad \frac{\partial I_4}{\partial C_{IJ}} = A_{1_I}A_{1_J}$$

$$\frac{\partial I_5}{\partial \boldsymbol{C}} = \boldsymbol{A}_1 \otimes \boldsymbol{C} \cdot \boldsymbol{A}_1 + \boldsymbol{C} \cdot \boldsymbol{A}_1 \otimes \boldsymbol{A}_1 \qquad\qquad \frac{\partial I_5}{\partial C_{IJ}} = A_{1_I}C_{JK}A_{1_K} + C_{IK}A_{1_K}A_{1_J}$$

$$\frac{\partial \bar{\boldsymbol{b}}}{\partial \boldsymbol{b}} = J^{-\frac{2}{3}}\left(\mathbb{I} - \frac{1}{3}\boldsymbol{b} \otimes \boldsymbol{b}^{-1}\right) \qquad\qquad \left(\frac{\partial \bar{\boldsymbol{b}}}{\partial \boldsymbol{b}}\right)_{ijkl} = J^{-\frac{2}{3}}\left(\frac{\delta_{ik}\delta_{jl} + \delta_{jk}\delta_{il}}{2} - \frac{1}{3}b_{ij}b_{kl}^{-1}\right)$$

The relationship between $\bar{I}_i$ and I_i can be expressed as,

$$\bar{I}_1 = J^{-\frac{2}{3}}I_1, \qquad\qquad \bar{I}_2 = J^{-\frac{4}{3}}I_2, \qquad\qquad \bar{I}_3 = 1,$$

$$\bar{I}_4 = J^{-\frac{2}{3}}I_4, \qquad\qquad \bar{I}_5 = J^{-\frac{4}{3}}I_5.$$

For the further derivation, let's first split $\boldsymbol{d} = \dot{\boldsymbol{e}} + \dot{\varepsilon}^{vol}\boldsymbol{I}$, where $\dot{\boldsymbol{e}}$ is the deviatoric part of the $\boldsymbol{d}$, and $\dot{\varepsilon}^{vol}$ is the trace of $\boldsymbol{d}$. Then find the derivative of $\bar{\boldsymbol{F}}$,

$$\begin{aligned}
\dot{\bar{\boldsymbol{F}}} &= \frac{d}{dt}J^{-\frac{1}{3}}\boldsymbol{F} \\
&= -\frac{1}{3}J^{-\frac{1}{3}}\mathrm{tr}\left(\boldsymbol{d}\right) \cdot \boldsymbol{F} + J^{-\frac{1}{3}}\boldsymbol{l} \cdot \boldsymbol{F} \\
&= -\frac{1}{3}\mathrm{tr}\left(\boldsymbol{d}\right)\bar{\boldsymbol{F}} + \boldsymbol{d} \cdot \bar{\boldsymbol{F}} + \boldsymbol{w} \cdot \bar{\boldsymbol{F}} \\
&= \dot{\boldsymbol{e}} \cdot \bar{\boldsymbol{F}} + \boldsymbol{w} \cdot \bar{\boldsymbol{F}} \qquad\qquad\qquad\qquad (2.3.6)
\end{aligned}$$

The derivative of $\bar{\boldsymbol{b}}$ becomes:

$$\begin{aligned}
\dot{\bar{\boldsymbol{b}}} &= \dot{\bar{\boldsymbol{F}}} \cdot \bar{\boldsymbol{F}}^T + \bar{\boldsymbol{F}} \cdot \dot{\bar{\boldsymbol{F}}}^T \\
&= \dot{\boldsymbol{e}} \cdot \bar{\boldsymbol{F}} \cdot \bar{\boldsymbol{F}}^T + \boldsymbol{w} \cdot \bar{\boldsymbol{F}} \cdot \bar{\boldsymbol{F}}^T + \bar{\boldsymbol{F}} \cdot \bar{\boldsymbol{F}}^T \cdot \dot{\boldsymbol{e}}^T - \bar{\boldsymbol{F}} \cdot \bar{\boldsymbol{F}}^T \cdot \boldsymbol{w} \\
&= \dot{\boldsymbol{e}} \cdot \bar{\boldsymbol{b}} + \bar{\boldsymbol{b}} \cdot \dot{\boldsymbol{e}} - \bar{\boldsymbol{b}} \cdot \boldsymbol{w} + \boldsymbol{w} \cdot \bar{\boldsymbol{b}} \qquad\qquad (2.3.7)
\end{aligned}$$

Since, $\mathrm{tr}\left(\boldsymbol{A} \cdot \boldsymbol{B}\right) = \boldsymbol{A} : \boldsymbol{B}^T = \boldsymbol{A}^T : \boldsymbol{B}$, $\mathrm{tr}\left(\dot{\bar{\boldsymbol{b}}}\right)$ becomes,

$$\mathrm{tr}\left(\dot{\bar{\boldsymbol{b}}}\right) = 2\bar{\boldsymbol{b}} : \dot{\boldsymbol{e}} \qquad\qquad\qquad\qquad (2.3.8)$$

Similarly, the derivative for $\bar{b} \cdot \bar{b}$ can be derived as,

$$\frac{d}{dt}\bar{b} \cdot \bar{b} = \dot{\bar{b}} \cdot \bar{b} + \bar{b} \cdot \dot{\bar{b}}$$

$$= \dot{e} \cdot \bar{b} \cdot \bar{b} + \bar{b} \cdot \dot{e} \cdot \bar{b} - \bar{b} \cdot w \cdot \bar{b} + w \cdot \bar{b} \cdot \bar{b} + \bar{b} \cdot \dot{e} \cdot \bar{b} + \bar{b} \cdot \bar{b} \cdot \dot{e} - \bar{b} \cdot \bar{b} \cdot w + \bar{b} \cdot w \cdot \bar{b}$$

$$(2.3.9)$$

Its trace becomes:

$$\mathrm{tr}\left(\frac{d}{dt}\bar{b} \cdot \bar{b}\right) = \bar{b} \cdot \bar{b} : \dot{e} + \bar{b} : \bar{b} \cdot \dot{e} + \bar{b} : w \cdot \dot{e} - \bar{b} : w \cdot \dot{e} + \bar{b} : \bar{b} \cdot \dot{e} + \bar{b} \cdot \bar{b} : \dot{e} + \bar{b} : \bar{b} \cdot w - \bar{b} \cdot \bar{b} : w$$

$$= 4\bar{b} \cdot \bar{b} : \dot{e} \qquad (2.3.10)$$

Similarly, the derivatives of $\bar{C}$, and $\bar{C} \cdot \bar{C}$ can be found as,

$$\dot{\bar{C}} = \dot{\bar{F}}^T \cdot \bar{F} + \bar{F} \cdot \dot{\bar{F}}$$

$$= \bar{F}^T \cdot \dot{e}^T \cdot \bar{F} - \bar{F}^T \cdot w \cdot \bar{F} + \bar{F}^T \cdot \dot{e} \cdot \bar{F} + \bar{F}^T \cdot w \cdot \bar{F}$$

$$= \bar{F}^T \cdot \dot{e}^T \cdot \bar{F} + \bar{F}^T \cdot \dot{e} \cdot \bar{F} \qquad (2.3.11)$$

$$\frac{d}{dt}\bar{C} \cdot \bar{C} = \dot{\bar{C}} \cdot \bar{C} + \bar{C} \cdot \dot{\bar{C}}$$

$$= \bar{F}^T \cdot \left(\dot{e} + \dot{e}^T\right) \cdot \bar{F} \cdot \bar{F}^T \cdot \bar{F} + \bar{F}^T \cdot \bar{F} \cdot \bar{F}^T \cdot \left(\dot{e} + \dot{e}^T\right) \cdot \bar{F}$$

$$= \bar{F}^T \cdot \left(\left(\dot{e} + \dot{e}^T\right) \cdot \bar{b} + \bar{b} \cdot \left(\dot{e} + \dot{e}^T\right)\right) \cdot \bar{F} \qquad (2.3.12)$$

By using Equation 2.3.8, the first variation of $\bar{I}_1$ becomes:

$$\delta \bar{I}_1 = 2\bar{b} : \delta e \qquad (2.3.13)$$

By the use of Equation 2.3.10, and Equation 2.3.8, the first variation of $\bar{I}_2$ becomes:

$$\delta \bar{I}_2 = \frac{1}{2}\left(2\bar{I}_1\left(2\bar{b} : \delta e\right) - 4\bar{b} \cdot \bar{b} : \delta e\right)$$

$$= 2\left(\bar{I}_1\bar{b} - \bar{b} \cdot \bar{b}\right) : \delta e \qquad (2.3.14)$$

Let's assume $\bar{a}_\alpha = F \cdot A_\alpha$, the variation in fourth invariant can be derived as by using Equation 2.3.11:

$$\delta \bar{I}_{4_{(\alpha\beta)}} = \bar{F} \cdot A_\alpha \cdot \left(\delta e + \delta e^T\right) \cdot \bar{F} \cdot A_\beta$$

$$= \bar{a}_\alpha \cdot \delta e \cdot \bar{a}_\beta + \bar{a}_\alpha \cdot \delta e^T \cdot \bar{a}_\beta$$

$$= \left(\bar{a}_\alpha \otimes \bar{a}_\beta + \bar{a}_\beta \otimes \bar{a}_\alpha\right) : \delta e \qquad (2.3.15)$$

Similarly, the first variation for the fifth invariant can be derived by using Equation 2.3.12:

$$\delta \bar{I}_{5_{(\alpha\beta)}} = \bar{a}_\alpha \cdot \left(\left(\delta e + \delta e^T\right) \cdot \bar{b} + \bar{b} \cdot \left(\delta e + \delta e^T\right)\right) \cdot \bar{a}_\beta$$

$$= \bar{a}_\alpha \cdot \delta e \cdot \bar{a}'_\beta + \bar{a}_\alpha \cdot \delta e^T \cdot \bar{a}'_\beta + \bar{a}'_\alpha \cdot \delta e \cdot \bar{a}_\beta + \bar{a}'_\alpha \cdot \delta e^T \cdot \bar{a}_\beta$$

$$= \left(\bar{a}_\alpha \otimes \bar{a}'_\beta + \bar{a}'_\alpha \otimes \bar{a}_\beta + \bar{a}_\beta \otimes \bar{a}'_\alpha + \bar{a}'_\beta \otimes \bar{a}_\alpha\right) : \delta e, \qquad (2.3.16)$$

where $\bar{a}'_\alpha = \bar{a}_\alpha \cdot \bar{b}$, and $\bar{a}'_\beta = \bar{b} \cdot \bar{a}_\beta$

After substituting equations 2.3.13, 2.3.14, 2.3.15, 2.3.16 into 2.3.5, and by comparing with Equation 2.3.2, we obtain:

$$
\begin{aligned}
\tilde{\sigma} = {}& \frac{2}{J} \left(\frac{\partial \Psi}{\partial \bar{I}_1} + \bar{I}_1 \frac{\partial \Psi}{\partial \bar{I}_2} \right) \mathrm{DEV} \left(\bar{b} \right) \\
& - \frac{2}{J} \frac{\partial \Psi}{\partial \bar{I}_2} \mathrm{DEV} \left(\bar{b} \cdot \bar{b} \right) \\
& + \sum_{\alpha=1}^{N} \sum_{\beta=1}^{\alpha} \left(\frac{\partial \Psi}{\partial \bar{I}_{4_{(\alpha\beta)}}} \mathrm{DEV} \left(\bar{a}_\alpha \otimes \bar{a}_\beta + \bar{a}_\beta \otimes \bar{a}_\alpha \right) \right) \\
& + \sum_{\alpha=1}^{N} \sum_{\beta=1}^{\alpha} \left(\frac{\partial \Psi}{\partial \bar{I}_{5_{(\alpha\beta)}}} \mathrm{DEV} \left(\bar{a}_\alpha \otimes \bar{a}'_\beta + \bar{a}'_\alpha \otimes \bar{a}_\beta + \bar{a}_\beta \otimes \bar{a}'_\alpha + \bar{a}'_\beta \otimes \bar{a}_\alpha \right) \right)
\end{aligned}
$$

where $\bar{a}_\alpha = \bar{F} \cdot A_\alpha$, $\bar{a}'_\beta = \bar{a}_\beta \cdot \bar{b}$, and $\bar{a}'_\alpha = \bar{b} \cdot \bar{a}_\alpha$,and

$$
p = -\frac{\partial \Psi}{\partial J}
$$

This expression of stress is valid for N fibers in different directions. The stress σ, calculated as $\sigma = \tilde{\sigma} - pI$.

Chapter 3

Micromechanics modeling

The fundamental goal of employing micromechanics is to homogenize material properties at a macroscopic scale, determining the effective properties of a heterogeneous material on the micro scale through homogenization.

Two primary approaches, the *average-field theory* and the *homogenization theory*, are utilized to understand the response of such materials. The former establishes a connection between experimentally measured quantities at the macroscopic level and volume averages at the microscopic scale, while the latter relates micro fields to macro fields through a perturbation method.

Homogenization theory commonly employs a periodic microstructure model, particularly suitable for composite materials with regularly or semi-regularly arranged microstructures. In contrast, the average-field theory often uses simpler microstructure models, like an isolated inclusion within an unbounded body, to determine effective properties.

Although both theories predict the same results, they are based on different principles. This section briefly discusses homogenization theory, followed by the exploration of various models through theoretical homogenization and a detailed discussion on numerical homogenization. Additionally, an equation for estimating effective properties in the case of linear anisotropy is developed. The chapter further delves into equations for applying periodicity, providing a detailed discussion and modifications necessary for ABAQUS. Subsequently, a plugin is introduced to automate the homogenization process in ABAQUS, concluding with a comparison of results between numerical and theoretical homogenization.

3.1   Representative volume elements (RVE)

Continuum mechanics deals with continuum in which infinitesimal part of the material retains the properties of the bulk material. However, all real materials, at some scale show heterogeneity. The use of micromechanical theory allows to take into account the effects of heterogeneity at the micro scale, and turn these results into effective properties which can be used at the macro scale. Micromechanics is able to do it by using the idea of representative volume element (RVE).

RVE is a volume of a material whose effective behaviour represents the material as whole. It should be small enough so that its infinitesimal behavior can be captured. On the other hand, it should be large enough that it would capture the essence of the microstructure from a statistical point of view. In other words, probability of finding a phase at a point does not depend on the point in the body. Then, if the displacement or traction boundary conditions are applied to RVE, we will get the same response that really represents the material. Hill (1963)[16] defined RVE based on the requirement that strain energy densities induced by applying homogeneous traction and equivalent homogeneous displacement boundary conditions must be essentially equivalent.

Let body $\mathcal{B}$ consists of heterogeneous materials. Let L be the characteristic length of the structural element at which experiment is conducted, and D is the size of RVE; d be the typical length scale of the micro constituent as shown in Figure 3.1.1. Typically the size of the RVE as such that these ratios of $\frac{d}{D}$, and $\frac{D}{L}$ must be less than 1; consequently, the response of the RVE represent the response of the composite material, and this response should be insensitive to the boundary conditions.

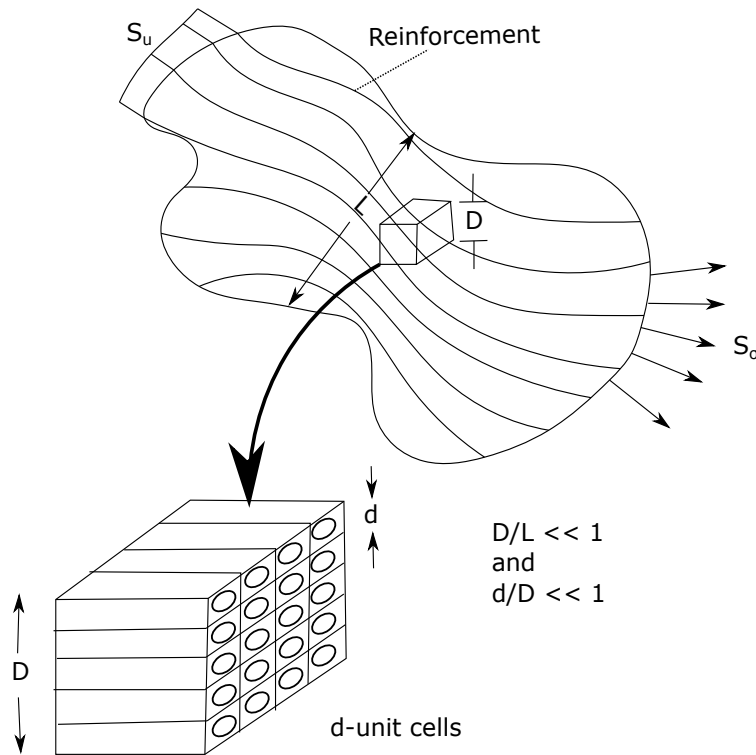Figure 3.1.1: Illustration of the relations between different scales; L is the scale of the structure, D is the scale of the RVE, d is the scale of the constituent; s_u, and s_σ are the boundary conditions of displacement and traction.

Definition 3.1.1 (Homogeneous boundary condition). *Let ε_{ij}^0, and σ_{ij}^0 are constant strain and constant stress tensors applied on the boundary $\partial\Omega$ of the homogeneous body. Then homogeneous displacement u_i, and traction t_i are defined as:*

$$u_i|_{\partial\Omega} = \varepsilon_{ij}^0 X_j,$$
$$t_i|_{\partial\Omega} = \sigma_{ij}^0 n_j,$$

where n_j is unit outward normal vector, and X_j is the position vector in the initial configuration.

Definition 3.1.2 (Volume averaging). *Let V be the volume of the RVE which is imposed by a homogeneous stress or deformation field, the average stress and strain tensors are defined by:*

$$\langle\sigma_{ij}\rangle = \frac{1}{V}\int_V \sigma_{ij}dV,$$
$$\langle\varepsilon_{ij}\rangle = \frac{1}{V}\int_V \varepsilon_{ij}dV.$$

Definition 3.1.3 (Average strain theorem). *Let ε_{ij}^0 be the constant applied strain on the RVE. Now assuming there is no displacement jump between the interface of constituents,*

$$\langle\varepsilon_{ij}\rangle = \varepsilon_{ij}^0.$$

Proof. Let there are two constituents consisting of volume Ω_1, and Ω_2 such that $\Omega = \Omega_1 \cup \Omega_2$. By using the definition 2.1.10 linearizerd strain,

$$\langle\boldsymbol{\varepsilon}\rangle = \frac{1}{\|\Omega\|}\int_\Omega \boldsymbol{\varepsilon}\ dV$$

$$= \frac{1}{\|\Omega\|}\left(\int_{\Omega_1} \boldsymbol{\varepsilon}\ dV + \int_{\Omega_2} \boldsymbol{\varepsilon}\ dV\right)$$

$$= \frac{1}{2\|\Omega\|}\left(\int_{\Omega_1}\left(\boldsymbol{\nabla u} + \boldsymbol{\nabla u}^T\right)dV + \int_{\Omega_2}\left(\boldsymbol{\nabla u} + \boldsymbol{\nabla u}^T\right)dV\right)$$

$$= \text{(By using Gauss theorem)}\frac{1}{2\|\Omega\|}\left(\int_{\partial\Omega_1}\left(\boldsymbol{u}\otimes\boldsymbol{n} + \boldsymbol{n}\otimes\boldsymbol{u}\right)dA + \int_{\partial\Omega_2}\left(\boldsymbol{u}\otimes\boldsymbol{n} + \boldsymbol{n}\otimes\boldsymbol{u}\right)dA\right)$$

$$= \frac{1}{2\|\Omega\|}\left(\int_{\partial\Omega_1\cup\partial\Omega_2\backslash\Gamma_{1-2}}\left(\boldsymbol{u}\otimes\boldsymbol{n} + \boldsymbol{n}\otimes\boldsymbol{u}\right)dA + \int_{\Gamma_{1-2}}\left(\llbracket\boldsymbol{u}\rrbracket\otimes\boldsymbol{n} + \boldsymbol{n}\otimes\llbracket\boldsymbol{u}\rrbracket\right)dA\right)$$

$\Gamma_{1-2} = \partial\Omega_1 \cap \partial\Omega_2$, by using definition $\boldsymbol{u} = \boldsymbol{\varepsilon}^0\cdot\boldsymbol{X}$,

$$= \frac{1}{2\|\Omega\|}\left(\int_{\partial\Omega_1\cup\partial\Omega_2\backslash\Gamma_{1-2}}\left(\left(\boldsymbol{\varepsilon}^0\cdot\boldsymbol{X}\right)\otimes\boldsymbol{n} + \boldsymbol{n}\otimes\left(\boldsymbol{\varepsilon}^0\cdot\boldsymbol{X}\right)\right)dA + \int_{\Gamma_{1-2}}\left(\llbracket\boldsymbol{u}\rrbracket\otimes\boldsymbol{n} + \boldsymbol{n}\otimes\llbracket\boldsymbol{u}\rrbracket\right)dA\right)$$

$= \text{(By using Gauss theorem)}$

$$\frac{1}{2\|\Omega\|}\left(\int_{\Omega\backslash\Gamma_{1-2}}\left(\boldsymbol{\nabla}\left(\boldsymbol{\varepsilon}^0\cdot\boldsymbol{X}\right) + \boldsymbol{\nabla}\left(\boldsymbol{\varepsilon}^0\cdot\boldsymbol{X}\right)\right)^T dV + \int_{\Gamma_{1-2}}\left(\llbracket\boldsymbol{u}\rrbracket\otimes\boldsymbol{n} + \boldsymbol{n}\otimes\llbracket\boldsymbol{u}\rrbracket\right)dA\right)$$

By considering $\boldsymbol{\nabla}\left(\boldsymbol{\varepsilon}^0\cdot\boldsymbol{X}\right) = \boldsymbol{\varepsilon}^0$,

$$= \boldsymbol{\varepsilon}^0 + \frac{1}{2\|\Omega\|}\int_{\Gamma_{1-2}}\left(\llbracket\boldsymbol{u}\rrbracket\otimes\boldsymbol{n} + \boldsymbol{n}\otimes\llbracket\boldsymbol{u}\rrbracket\right)dA,$$

which shows, the result is only valid if and if displacement jump $\llbracket\boldsymbol{u}\rrbracket$ is zero. $\qquad\square$

Definition 3.1.4 (Average stress theorem). *Let σ_{ij}^0 be the constant applied stress on the RVE. Now assuming there is no body force,*

$$\langle \sigma_{ij} \rangle = \sigma_{ij}^0.$$

Proof. We can start the proof by considering only the static part of the equation 2.2.4 $(-\nabla \cdot \boldsymbol{\sigma} = \boldsymbol{b})$, and also by using the identity $\nabla \cdot (\boldsymbol{\sigma} \otimes \boldsymbol{X}) = (\nabla \cdot \boldsymbol{\sigma}) \otimes \boldsymbol{X} + \boldsymbol{\sigma} \cdot \nabla \boldsymbol{X} = -\boldsymbol{b} \otimes \boldsymbol{X} + \boldsymbol{\sigma} \implies \boldsymbol{\sigma} = \nabla \cdot (\boldsymbol{\sigma} \otimes \boldsymbol{X}) + \boldsymbol{b} \otimes \boldsymbol{X}$. Then we can substitute into average stress definition,

$$\langle \boldsymbol{\sigma} \rangle = \frac{1}{\|\Omega\|} \left(\int_\Omega \nabla \cdot (\boldsymbol{\sigma} \otimes \boldsymbol{X}) + \boldsymbol{b} \otimes \boldsymbol{X} \right) dV$$

$$= (\text{By Gauss divergence theorem}) \frac{1}{\|\Omega\|} \int_{\partial\Omega} (\boldsymbol{\sigma} \otimes \boldsymbol{X}) \cdot \boldsymbol{n} \ dA + \frac{1}{\|\Omega\|} \int_\Omega \boldsymbol{b} \otimes \boldsymbol{X} \ dV,$$

since stress at boundary is assumed to be constant $\boldsymbol{\sigma}^0$,

$$= \frac{1}{\|\Omega\|} \boldsymbol{\sigma}^0 \int_{\partial\Omega} \boldsymbol{X} \cdot \boldsymbol{n} \ dA + \frac{1}{\|\Omega\|} \int_\Omega \boldsymbol{b} \otimes \boldsymbol{X} \ dV,$$

since $\int_{\partial\Omega} \boldsymbol{X} \cdot \boldsymbol{n} \ dA = \int_\Omega \nabla \cdot \boldsymbol{X} \ dV = \|\Omega\|,$

$$= \boldsymbol{\sigma}^0 + \frac{1}{\|\Omega\|} \int_\Omega \boldsymbol{b} \otimes \boldsymbol{X} \ dV,$$

which shows, the result is valid for $\boldsymbol{b} = 0$. It is important to see that this result is also valid for displacement jump. □

3.2 Determination of effective properties

The main goal of the micromechanics theory is to find the effective properties of the material which is made up of different materials. Let V_f be volume ratio of fiber, and let ξ be the parameter for taking into account the shape and geometric properties of reinforcement, and let $\mathbf{C}^m, \mathbf{C}^f$ be the stiffness of fiber and matrix. The main goal is to find the effective properties $\mathbf{C}$,

$$\mathbf{C} = \boldsymbol{f}\left(V_f, \mathbf{C}^m, \mathbf{C}^f, \xi\right).$$

There are four main approaches exist to find these effective properties such as:

1. analytical methods

2. numerical methods

3. semi-empirical methods

4. experimental

Analytical methodologies rely on a multitude of underlying assumptions, which will be briefly introduced in the subsequent section. In contrast, numerical approaches employ finite difference and finite element methods to yield highly precise results in proximity to experimental data, albeit necessitating substantial computational resources.

Semi-empirical techniques are founded upon analytical theories with a reduced emphasis on empirical experimentation. Notably, Barbero provides insights into certain semi-empirical methods, which require a range of parameters that may be determined via experimental means.

The experimental determination of effective material properties in diverse directions is a laborious and costly endeavor, chiefly due to the variability of these properties in relation to volume fraction and geometric arrangements.

A majority of analytical methods emanate from the concept of *equivalent eigen strain*, as proposed by [14], which addresses the scenario of a single ellipsoidal inclusion within an infinitely elastic matrix material. The interplay among such inclusions is elucidated through the application of the *Eshelby solution*, a concept elucidated by [33]. An alternative approach, known as the *self-consistent method*, was introduced by [17], considering a random distribution of inclusions within the infinite elastic material matrix.

The homogenization of heterogeneous materials with periodic microstructures has been accomplished through diverse methodologies, including an extension of the Eshelby inclusion problem as elucidated by [13], the Fourier series technique, and variational principles as exemplified by [6, 1]. Each of these methods provides approximations to the underlying micromechanical problem and establishes upper and lower bounds, which are determined through the utilization of variational principles.

For the investigation of nonlinear material behavior within heterogeneous materials characterized by periodic microstructures, finite element methods stand as the principal tool capable of elucidating interactions among inclusions and modeling inelastic responses.

3.2.1 Analytical Homogenization

The basic equation for all analytical models can be written as,

$$\mathbf{C} = \sum V_i \mathbf{C}^i \cdot \boldsymbol{A}^i \qquad\qquad \sum V_i \boldsymbol{A}^i = \boldsymbol{I}$$
$$\mathbf{S} = \sum V_i \mathbf{S}^i \cdot \boldsymbol{B}^i \qquad\qquad \sum V_i \boldsymbol{B}^i = \boldsymbol{I},$$

where $\mathbf{C}, \mathbf{S}$ are effective compliance and stiffness tensors. The $(\bullet)^i$ represents the properties of the i-th material. Similarly, V_i is the volume fraction of the i-th material. Moreover, $\boldsymbol{A}^i, \boldsymbol{B}^i$ are the strain and stress concentration tensors of the i-th phase, and $\boldsymbol{I}$ is the second order identity tensor.

3.2.2 Reuss Model

This is a quite simplified model also known as *rule of mixtures* based on the assumption that the strain produced in both fiber matrix is same. This makes the strain concentration tensor to be identity. For example if there are only two phases of the materials fiber and matrix, the equation becomes,

$$\mathbf{C} = V_f \mathbf{C}^f + \left(1 - V_f\right) \mathbf{C}^m.$$

3.2.3 Voigt Model

This method is also known *inverse rule of mixtures*, assumes that the stress tensors in both fiber and matrix is same which results into identity of stress concentration tensor.

$$\mathbf{S} = V_f \mathbf{S}^f + (1 - V_f) \, \mathbf{S}^m.$$

Both Reuss model and Voigt model give us the extremes of engineering constants. Reuss model can be interpreted as if fibers are in the direction 1, and Voigt model can be interpreted as if fibers are in the direction of 2. By using these simplified models, $E_1, \nu_{12}, E_2,$ and G_{12} can be roughly estimated. The detail derivation of these equations can be found at [23].

3.2.4 Periodic Microstructure Model

Microstructures can repeat themselves in a structure in a periodic manner or in an aperiodic manner. Some analytical solutions exist in a literature for periodic microstructures. For instance, Barbero and Luciano developed explicit formulas for a composite reinforced by isotropic, circular-cylindrical fibers, which are periodically arranged in a squared array(Figure).

In the following text, we always assume that the fibers are aligned with $x - axis$. These fibers are equally spaced with a distance $2a_2$ in the direction of $y - axis$, and with the distance of $2a_3$ in the direction of $z - axis$. For the case of square symmetry, we assume $2a_2 = 2a_3$. This leads to 6 unique components for the stiffness tensor.

Let λ_m and μ_m are the Lamé parameters for the matrix and λ_f and μ_f be the parameters for the fiber material. Let the volume fraction of the fiber to be denoted by V_f. The coefficients are written as given by Barbero and Luciano,

$$C^*{}_{1111} = \lambda_m + 2\mu_m - \frac{V_f}{D} \left(\frac{S_3^2}{\mu_m^2} - \frac{2S_6 S_3}{\mu_m^2 g} - \frac{aS_3}{\mu_m c} + \frac{S_6^2 - S_7^2}{\mu_m^2 g^2} + \frac{aS_6 + bS_7}{c\mu_m g} + \frac{a^2 - b^2}{4c^2} \right)$$

$$C^*{}_{1122} = \lambda_m + \frac{V_f b}{D} \left(\frac{S_3}{2c\mu_m} - \frac{S_6 - S_7}{2c\mu_m g} - \frac{a + b}{4c^2} \right)$$

$$C^*{}_{2233} = \lambda_m + \frac{V_f}{D} \left(\frac{aS_7}{2c\mu_m g} - \frac{ba + b^2}{4c^2} \right)$$

$$C^*{}_{2222} = \lambda_m + 2\mu_m - \frac{V_f}{D} \left(-\frac{aS_3}{2\mu_m c} + \frac{aS_6}{2c\mu_m g} + \frac{a^2 - b^2}{4c^2} \right)$$

$$C^*{}_{1212} = \mu_m - V_f \left(-\frac{2S_3}{\mu_m} + \frac{1}{\mu_m - \mu_f} + \frac{2S_7}{\mu_m (1 - \nu_m)} \right)^{-1}$$

$$C^*{}_{1313} = \mu_m - V_f \left(-\frac{S_3}{\mu_m} + \frac{1}{\mu_m - \mu_f} \right)^{-1}$$

where,

$$D = \frac{aS_3^2}{2\mu_m^2 c} - \frac{aS_6 S_3^2}{c\mu_m^2 g} + \frac{a \left(S_6^2 S_7^2 \right)}{2c\mu_m^2 g^2} + \frac{S_3 \left(b^2 - a^2 \right)}{2\mu_m c^2} + \frac{S_6 \left(a^2 - b^2 \right) + S_7 \left(ab + b^2 \right)}{2c^2 \mu_m^2 g} + \frac{a^3 - 2b^3 - 3ab^2}{8c^3}$$

and,

$$a = \mu_f - \mu_m - 2\mu_f\nu_m + 2\mu_m\nu_f$$
$$b = -\mu_m\nu_m + \mu_f\nu_f + 2\mu_m\nu_m\nu_f - 2\mu_f\nu_m\nu_f$$
$$c = (\mu_m - \mu_f)(\mu_f - \mu_m + \mu_f\nu_f - \mu_m\nu_m + 2\mu_m\nu_f - 2\mu_f\nu_m + 2\mu_m\nu_m\nu_f - 2\mu_f\nu_m\nu_f)$$
$$g = 2 - 2\nu_m$$

The constants S_3, S_6, and S_7 for the composite reinforced by long circular cylindrical fibers, periodically arranged in a square array, aligned with $x - axis$ with $a_2 = a_3$ given in [Ever. Babero]

$$S_3 = 0.49247 - 0.47603V_f - 0.02748V_f^2$$
$$S_6 = 0.36844 - 0.14944V_f - 0.27152V_f^2$$
$$S_7 = 0.12346 - 0.32035V_f + 0.23517V_f^2$$

The tensor C^* needs only 6 components because of the square symmetry. This tensor can be transformed into more general result which would be applicable for the trnasverse isotropic composite material.

Let T be the coordinate transformation matrix, and rotation θ about $x - axis$ yields,

$$B(\theta) = T^T(\theta)\,C^*T(\theta).$$

Then the equivalent transversely isotropic tensor is obtained by averaging,

$$\bar{B} = \frac{1}{\pi}\int_0^\pi B(\theta)\ d\theta$$

Then, using the relations between the engineering constants and the components of $\bar{B}$, the following engneering constants can be obtained

$$E_1 = C^*_{1111} - \frac{2C^*_{1122}}{(C^*_{2222} + C^*_{2233})}$$
$$E_2 = \frac{(2C^*_{1111}C^*_{2222} + 2C^*_{1111}C^*_{2233} - 4C^*_{1122}C^*_{1122})(C^*_{2222} - C^*_{2233} + 2C^*_{1212})}{3C^*_{1111}C^*_{2222} + C^*_{1111}C^*_{2233} + 2C^*_{1111}C^*_{1212} - 4C^*_{1122}C^*_{1122}}$$
$$G_{12} = G_{13} = C^*_{1313} \qquad\qquad (3.2.1)$$
$$\nu_{12} = \nu_{13} = \frac{C^*_{1122}}{C^*_{2222} + C^*_{2233}}$$
$$\nu_{23} = \frac{C^*_{1111}C^*_{2222} + 3C^*_{1111}C^*_{2233} - 2C^*_{1111}C^*_{1212} - 4C^*_{1122}C^*_{1122}}{3C^*_{1111}C^*_{2222} + C^*_{1111}C^*_{2233} + 2C^*_{1111}C^*_{1212} - 4C^*_{1122}C^*_{1122}}$$
$$G_{23} = \frac{E_2}{2(1 + \nu_{23})} \qquad\qquad (3.2.2)$$

These equations are implemented in Python, and can be found at https://github.com/Jamal-dev/Periodic-Microstructure.

3.3   Numerical Homogenization

Achieving homogenization using finite element method can be considered as the numerical ho-
mogenization. In this section, we first discuss a particular case in which fibers are considered of
infinite length which are embedded in the matrix material, as shown in Figure 3.3.1. Then, the
analysis will be tailored for the air springs.
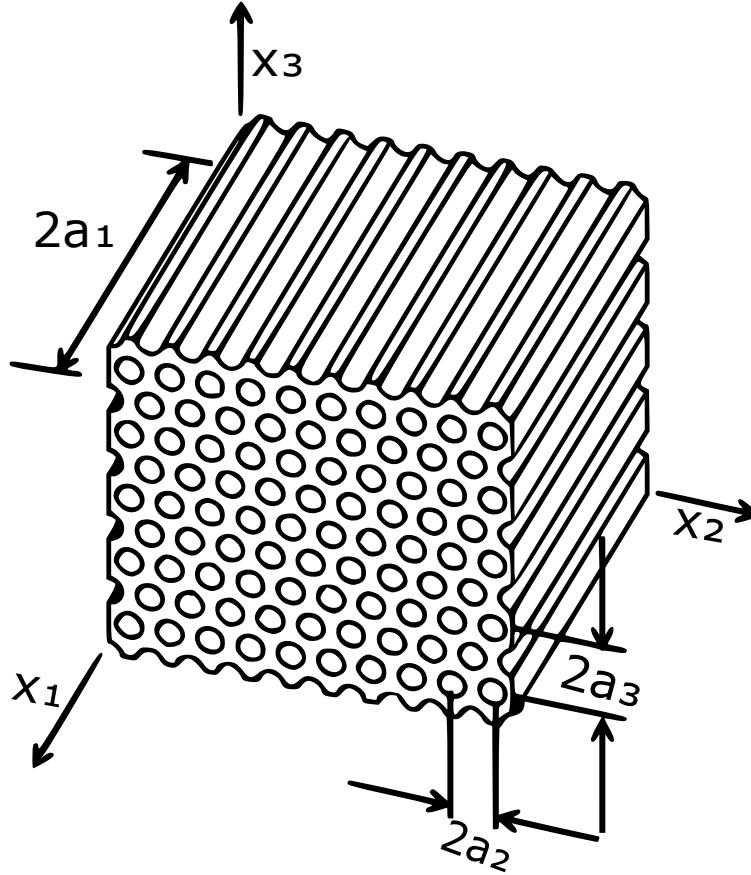
Figure 3.3.1: Periodic heterogeneous material with hexagonal symmetry. Fibers are aligned with
x_1 axis. $2a_2$ is the length between the fibers in x_2 axis. Similarly, $2a_3$ is the length between the
fibers in x_3 direction.

The plane orthogonal to the fiber axis shows hexagonal symmetry of the microstrucutre, which
is shown in Figure 3.3.2. Because of the periodicity, one can establish a $3 - D$ RVE, as shown
in Figure 3.3.3.
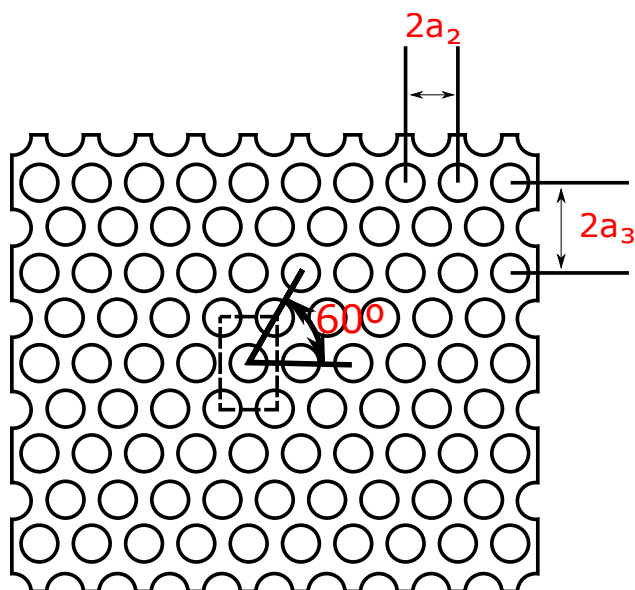
Figure 3.3.2: Cross-sectional view of the fiber axis
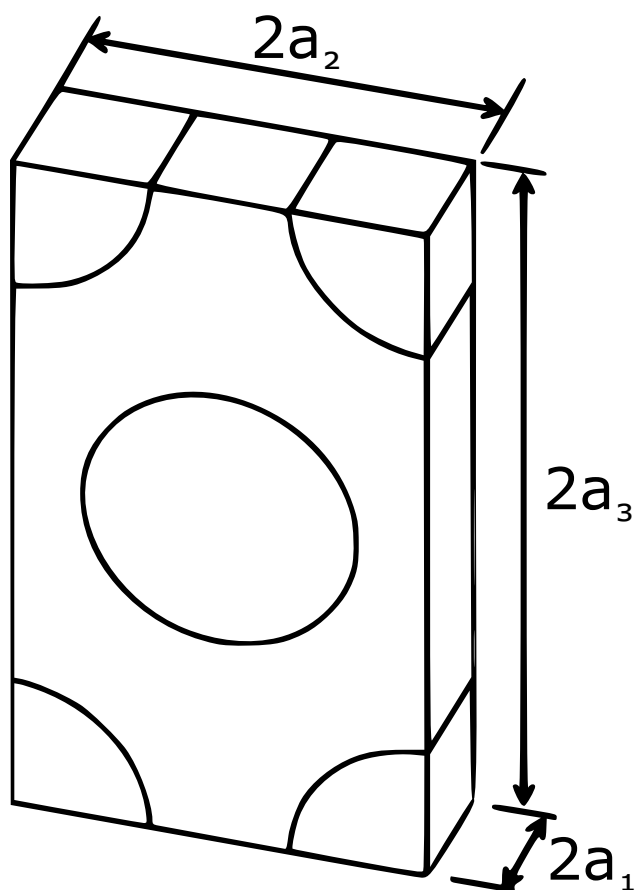
Figure 3.3.3: Representative volume element (RVE) for hexagonal symmetry

3.3.1 Average properties

If the linear elastic model allows us to establish a connection between the average stress and average strain, we can express this relationship through the following equations:

$$
\begin{bmatrix}
\langle \sigma_{11} \rangle \\
\langle \sigma_{22} \rangle \\
\langle \sigma_{33} \rangle \\
\langle \sigma_{12} \rangle \\
\langle \sigma_{13} \rangle \\
\langle \sigma_{23} \rangle
\end{bmatrix}
=
\begin{bmatrix}
C^*_{1111} & C^*_{1122} & C^*_{1133} & C^*_{1112} & C^*_{1113} & C^*_{2323} \\
C^*_{2211} & C^*_{2222} & C^*_{3333} & C^*_{1212} & C^*_{1313} & C^*_{2323} \\
C^*_{3311} & C^*_{33}22 & C^*_{3333} & C^*_{33}12 & C^*_{3313} & C^*_{3323} \\
C^*_{1211} & C^*_{12}22 & C^*_{1233} & C^*_{1212} & C^*_{1213} & C^*_{1223} \\
C^*_{1311} & C^*_{13}22 & C^*_{1333} & C^*_{1312} & C^*_{1313} & C^*_{1323} \\
C^*_{2311} & C^*_{23}22 & C^*_{2333} & C^*_{2312} & C^*_{2313} & C^*_{2323}
\end{bmatrix}
\begin{bmatrix}
\langle \varepsilon_{11} \rangle \\
\langle \varepsilon_{22} \rangle \\
\langle \varepsilon_{33} \rangle \\
\langle \varepsilon_{12} \rangle \\
\langle \varepsilon_{13} \rangle \\
\langle \varepsilon_{23} \rangle
\end{bmatrix}
\tag{3.3.1}
$$

here, the tensor C^* is the effective compliance tensor.

Upon accepting the validity of Equation 3.3.1, we can determine the unknowns within C^* by considering six independent loading scenarios, as shown in figures [3.3.4,3.3.5]. In accordance with the definition of average strain provided in 3.1.3, one can relate the average strain within the Representative Volume Element (RVE) to the applied loading conditions on the RVE. Consequently, it is necessary to establish six independent cases, as follows:

$$
\varepsilon^0 \text{ or } \boldsymbol{\sigma}^0 =
\begin{bmatrix} \beta & 0 & 0 \\ 0 & 0 & 0 \\ 0 & 0 & 0 \end{bmatrix},
\begin{bmatrix} 0 & 0 & 0 \\ 0 & \beta & 0 \\ 0 & 0 & 0 \end{bmatrix},
\begin{bmatrix} 0 & 0 & 0 \\ 0 & 0 & 0 \\ 0 & 0 & \beta \end{bmatrix},
\begin{bmatrix} 0 & \beta & 0 \\ \beta & 0 & 0 \\ 0 & 0 & 0 \end{bmatrix},
\begin{bmatrix} 0 & 0 & 0 \\ 0 & 0 & \beta \\ 0 & \beta & 0 \end{bmatrix},
\begin{bmatrix} 0 & 0 & \beta \\ 0 & 0 & 0 \\ \beta & 0 & 0 \end{bmatrix},
\tag{3.3.2}
$$

where β is a scalar number. First three loading are simple tension or compression in the RVE. Similarly, the last three ladings are different cases for pure shear. It can be seen if $\beta = 1$, the loading case 1 will yield the unknowns for the first column of C^* matrix. In the same way, the other columns of this matrix can be found out.

This approach can be extended to calculate all 36 unknowns. To determine these constants, let $\langle \sigma^i_{11} \rangle$ represent the stress component (average stress within the RVE) for the loading case i, and correspondingly, let $\langle \varepsilon^i_{11} \rangle$ denote the strain component (average strain within the RVE). The relationship between these quantities can be expressed as:

$$
\begin{bmatrix}
\langle \sigma^1_{11} \rangle \\
\langle \sigma^2_{11} \rangle \\
\langle \sigma^3_{11} \rangle \\
\langle \sigma^4_{11} \rangle \\
\langle \sigma^5_{11} \rangle \\
\langle \sigma^6_{11} \rangle
\end{bmatrix}
=
\begin{bmatrix}
\langle \varepsilon^1_{11} \rangle & \langle \varepsilon^1_{22} \rangle & \langle \varepsilon^1_{33} \rangle & \langle \varepsilon^1_{12} \rangle & \langle \varepsilon^1_{13} \rangle & \langle \varepsilon^1_{23} \rangle \\
\langle \varepsilon^2_{11} \rangle & \langle \varepsilon^2_{22} \rangle & \langle \varepsilon^2_{33} \rangle & \langle \varepsilon^2_{12} \rangle & \langle \varepsilon^2_{13} \rangle & \langle \varepsilon^2_{23} \rangle \\
\langle \varepsilon^3_{11} \rangle & \langle \varepsilon^3_{22} \rangle & \langle \varepsilon^3_{33} \rangle & \langle \varepsilon^3_{12} \rangle & \langle \varepsilon^3_{13} \rangle & \langle \varepsilon^3_{23} \rangle \\
\langle \varepsilon^4_{11} \rangle & \langle \varepsilon^4_{22} \rangle & \langle \varepsilon^4_{33} \rangle & \langle \varepsilon^4_{12} \rangle & \langle \varepsilon^4_{13} \rangle & \langle \varepsilon^4_{23} \rangle \\
\langle \varepsilon^5_{11} \rangle & \langle \varepsilon^5_{22} \rangle & \langle \varepsilon^5_{33} \rangle & \langle \varepsilon^5_{12} \rangle & \langle \varepsilon^5_{13} \rangle & \langle \varepsilon^5_{23} \rangle \\
\langle \varepsilon^6_{11} \rangle & \langle \varepsilon^6_{22} \rangle & \langle \varepsilon^6_{33} \rangle & \langle \varepsilon^6_{12} \rangle & \langle \varepsilon^6_{13} \rangle & \langle \varepsilon^6_{23} \rangle
\end{bmatrix}
\begin{bmatrix}
C^*_{1111} \\
C^*_{1122} \\
C^*_{1133} \\
C^*_{1112} \\
C^*_{1113} \\
C^*_{1123}
\end{bmatrix}
$$

Let

$$
b(\sigma_{11}) = \begin{bmatrix} \langle \sigma^1_{11} \rangle & \langle \sigma^2_{11} \rangle & \langle \sigma^3_{11} \rangle & \langle \sigma^4_{11} \rangle & \langle \sigma^5_{11} \rangle & \langle \sigma^6_{11} \rangle \end{bmatrix}^T
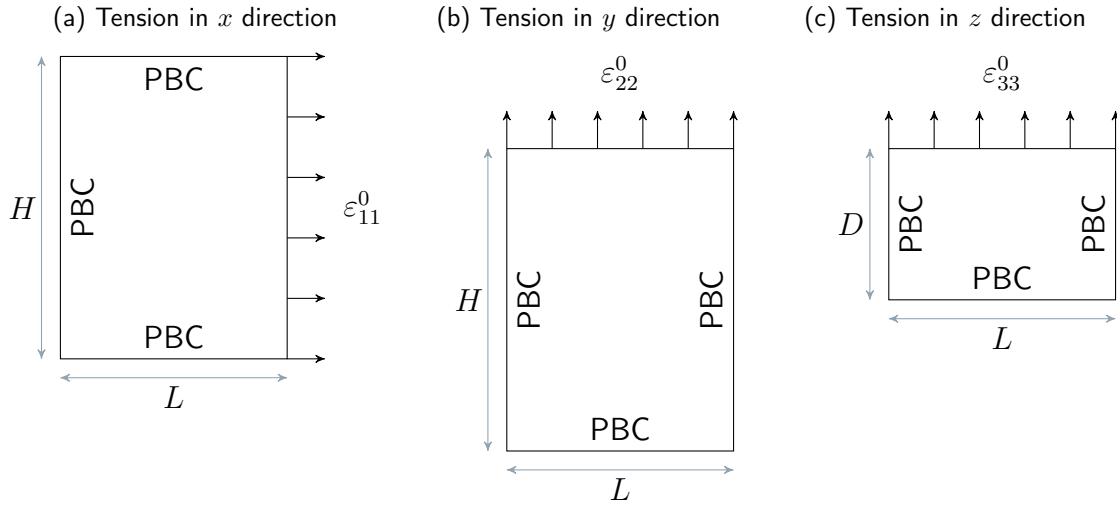$$

Figure 3.3.4: Normal strain loading cases. L, H, D are the length, width, and depth of the RVE. PBC here stands for periodic boundary condition.

$$\mathbf{\Gamma}\left(\boldsymbol{\varepsilon}\right) = \begin{bmatrix} \langle\varepsilon_{11}^1\rangle & \langle\varepsilon_{22}^1\rangle & \langle\varepsilon_{33}^1\rangle & \langle\varepsilon_{12}^1\rangle & \langle\varepsilon_{13}^1\rangle & \langle\varepsilon_{23}^1\rangle \\ \langle\varepsilon_{11}^2\rangle & \langle\varepsilon_{22}^2\rangle & \langle\varepsilon_{33}^2\rangle & \langle\varepsilon_{12}^2\rangle & \langle\varepsilon_{13}^2\rangle & \langle\varepsilon_{23}^2\rangle \\ \langle\varepsilon_{11}^3\rangle & \langle\varepsilon_{22}^3\rangle & \langle\varepsilon_{33}^3\rangle & \langle\varepsilon_{12}^3\rangle & \langle\varepsilon_{13}^3\rangle & \langle\varepsilon_{23}^3\rangle \\ \langle\varepsilon_{11}^4\rangle & \langle\varepsilon_{22}^4\rangle & \langle\varepsilon_{33}^4\rangle & \langle\varepsilon_{12}^4\rangle & \langle\varepsilon_{13}^4\rangle & \langle\varepsilon_{23}^4\rangle \\ \langle\varepsilon_{11}^5\rangle & \langle\varepsilon_{22}^5\rangle & \langle\varepsilon_{33}^5\rangle & \langle\varepsilon_{12}^5\rangle & \langle\varepsilon_{13}^5\rangle & \langle\varepsilon_{23}^5\rangle \\ \langle\varepsilon_{11}^6\rangle & \langle\varepsilon_{22}^6\rangle & \langle\varepsilon_{33}^6\rangle & \langle\varepsilon_{12}^6\rangle & \langle\varepsilon_{13}^6\rangle & \langle\varepsilon_{23}^6\rangle \end{bmatrix}$$

$$I = \{11, 22, 33, 12, 13, 23\}$$

$$\begin{aligned} C_{11i}^* &= \mathbf{\Gamma}^{-1}\left(\boldsymbol{\varepsilon}\right) b(\sigma_{11}) & \forall i \in I \\ C_{22i}^* &= \mathbf{\Gamma}^{-1}\left(\boldsymbol{\varepsilon}\right) b(\sigma_{22}) & \forall i \in I \\ C_{33i}^* &= \mathbf{\Gamma}^{-1}\left(\boldsymbol{\varepsilon}\right) b(\sigma_{33}) & \forall i \in I \\ C_{12i}^* &= \mathbf{\Gamma}^{-1}\left(\boldsymbol{\varepsilon}\right) b(\sigma_{12}) & \forall i \in I \\ C_{13i}^* &= \mathbf{\Gamma}^{-1}\left(\boldsymbol{\varepsilon}\right) b(\sigma_{13}) & \forall i \in I \\ C_{23i}^* &= \mathbf{\Gamma}^{-1}\left(\boldsymbol{\varepsilon}\right) b(\sigma_{23}) & \forall i \in I \end{aligned}$$

This relationship can be further simplified as follows:

$$\mathbf{\Gamma}\left(\boldsymbol{\sigma}\right) = \begin{bmatrix} \langle\sigma_{11}^1\rangle & \langle\sigma_{22}^1\rangle & \langle\sigma_{33}^1\rangle & \langle\sigma_{12}^1\rangle & \langle\sigma_{13}^1\rangle & \langle\sigma_{23}^1\rangle \\ \langle\sigma_{11}^2\rangle & \langle\sigma_{22}^2\rangle & \langle\sigma_{33}^2\rangle & \langle\sigma_{12}^2\rangle & \langle\sigma_{13}^2\rangle & \langle\sigma_{23}^2\rangle \\ \langle\sigma_{11}^3\rangle & \langle\sigma_{22}^3\rangle & \langle\sigma_{33}^3\rangle & \langle\sigma_{12}^3\rangle & \langle\sigma_{13}^3\rangle & \langle\sigma_{23}^3\rangle \\ \langle\sigma_{11}^4\rangle & \langle\sigma_{22}^4\rangle & \langle\sigma_{33}^4\rangle & \langle\sigma_{12}^4\rangle & \langle\sigma_{13}^4\rangle & \langle\sigma_{23}^4\rangle \\ \langle\sigma_{11}^5\rangle & \langle\sigma_{22}^5\rangle & \langle\sigma_{33}^5\rangle & \langle\sigma_{12}^5\rangle & \langle\sigma_{13}^5\rangle & \langle\sigma_{23}^5\rangle \\ \langle\sigma_{11}^6\rangle & \langle\sigma_{22}^6\rangle & \langle\sigma_{33}^6\rangle & \langle\sigma_{12}^6\rangle & \langle\sigma_{13}^6\rangle & \langle\sigma_{23}^6\rangle \end{bmatrix}$$

Furthermore, it can be modified as:

$$\boldsymbol{C}^* = \mathbf{\Gamma}^T\left(\boldsymbol{\sigma}\right) \mathbf{\Gamma}^{-T}\left(\boldsymbol{\varepsilon}\right) \tag{3.3.3}$$

(a) Loading ε_{12}

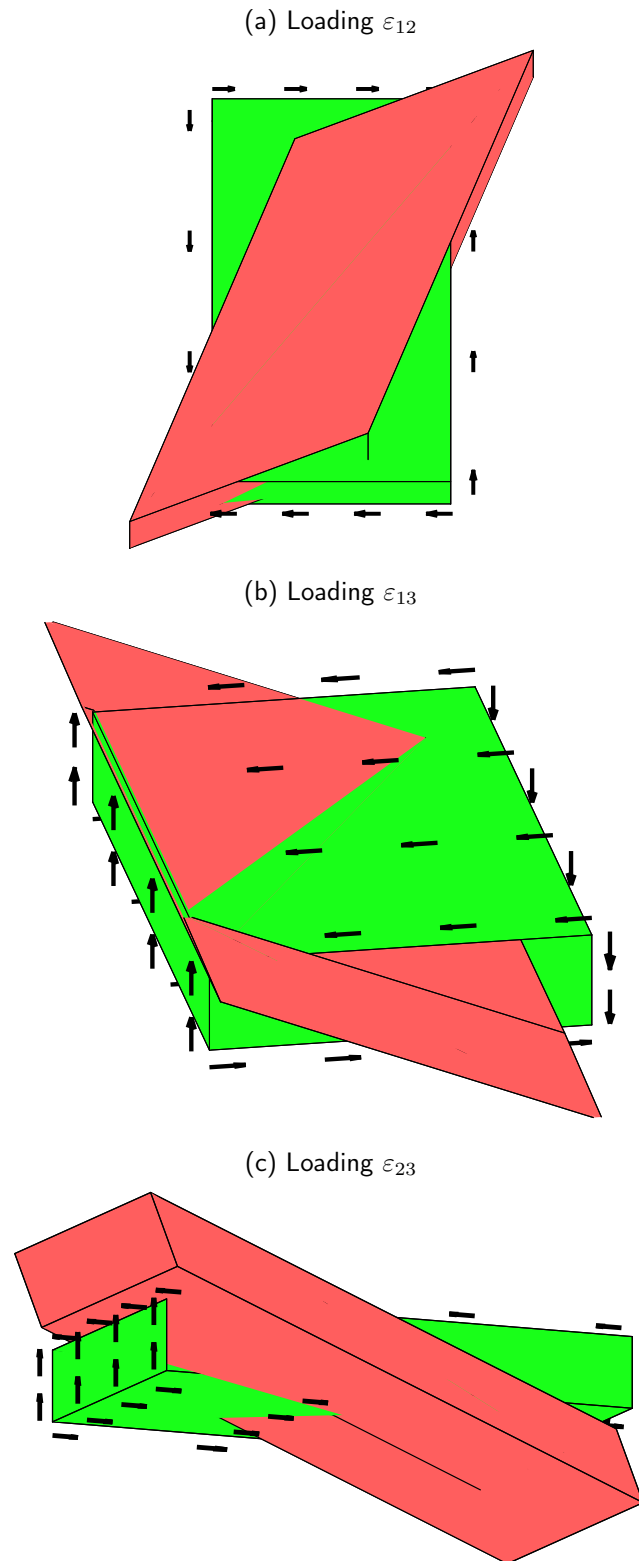(b) Loading ε_{13}

(c) Loading ε_{23}

Figure 3.3.5: Loading cases for shear. Here body in green is in the initial configuration; while, red is in the current configuration after applying the shear loading

In this expression, $\mathbf{\Gamma}\left(\boldsymbol{\sigma}\right)$ and $\mathbf{\Gamma}\left(\boldsymbol{\varepsilon}\right)$ are stacks of average stress and average strain for 6 loading cases. This relationship is fundamental in determining the effective compliance tensor $\boldsymbol{C}^*$, which characterizes the material's response to external loads within the RVE. For the verification of this equation, we shall establish an example in which properties will be first predicted by the periodic microstructure theory, and then the results will be compared with this equation. To achieve this, first we have to implement this equation in ABAQUS.

3.3.2 Periodic boundary condition

As shown in Figure 3.1.1, the structure is composed of RVE. Consequently, we have to apply a special boundary condition which is known as *periodic boundary condition*. The first task is to transform the Equation 3.3.2 into the results of displacement and traction because FEM codes usually follow only these boundary conditions; then, we have to use the idea of periodicity. The basic idea of the periodicity is that the displacement of nodes of two opposite faces must be same given that there is no applied strain on them. We can label the faces of RVE, as shown in Figure 3.3.6. This rectangular parallelepiped exhibits six distinct faces, each precisely labeled as follows: left, right, top, bottom, front, and back. In the context of the coordinate axes (x_1, x_2, x_3), the displacement at the front face is described by the function $u_i\left(a_1, x_2, x_3\right)$. Correspondingly, the expressions $u_i\left(-a_1, x_2, x_3\right)$, $u_i\left(x_1, -a_2, x_3\right)$, $u_i\left(x_1, a_2, x_3\right)$, $u_i\left(x_1, x_2, a_3\right)$, and $u_i\left(x_1, x_2, -a_3\right)$ denote the displacement functions associated with the back, left, right, top, and bottom faces, respectively.

For the periodicity, the strain and stress fields both need to be periodic. We can decompose the stress and strain into their average part and in the periodic part as,

$$\boldsymbol{\varepsilon}\left(x_1, x_2, x_3\right) = \boldsymbol{\varepsilon}^0 + \boldsymbol{\varepsilon}^P\left(x_1, x_2, x_3\right)$$
$$\boldsymbol{\sigma}\left(x_1, x_2, x_3\right) = \boldsymbol{\sigma}^0 + \boldsymbol{\sigma}^P\left(x_1, x_2, x_3\right),$$

where $\boldsymbol{\varepsilon}^0$, $\boldsymbol{\sigma}^0$ are average strain and strain as per definition 3.1.2, and $\boldsymbol{\varepsilon}^P$, $\boldsymbol{\sigma}^P$ are V-periodic defined as the parts of the strain and stress fields with null average in V,

$$\int_V \boldsymbol{\varepsilon}^P \, dV = 0,$$
$$\int_V \boldsymbol{\sigma}^P \, dV = 0. \tag{3.3.4}$$

By using the definition 3.1.1,

$$u_i\left(x_1, x_2, x_3\right) = \varepsilon_{ij}^0 x_j + u_i^p\left(x_1, x_2, x_3\right), \tag{3.3.5}$$
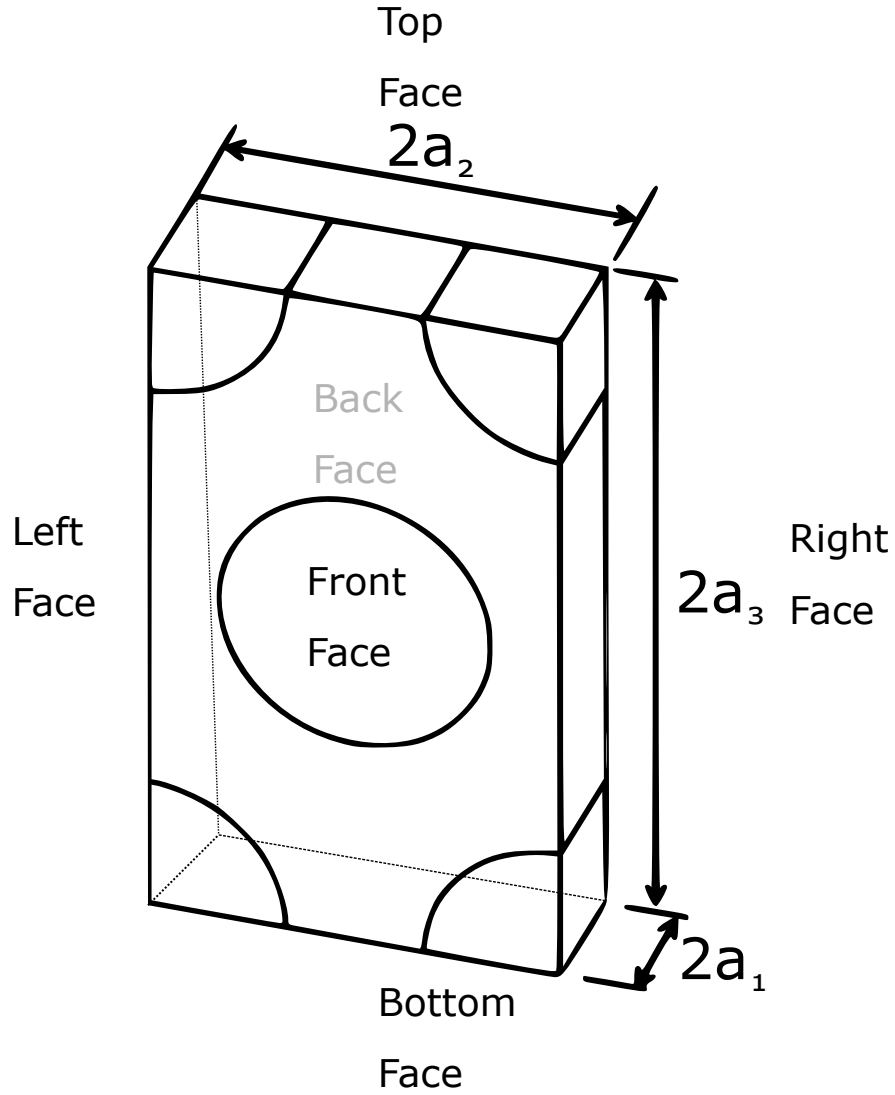
Figure 3.3.6: Labeling of Faces on a Rectangular Parallelepiped.Labeling of Faces.

in which $u_i^p (x_1, x_2, x_3)$ is periodic part of the displacement, and it must satisfy Equation 3.3.4. Now considering, continuity of $u_i^p (x_1, x_2, x_3)$, the following conditions must satisfy on the boundary ∂V of the RVE.

$$u_i^p (-a_1, x_2, x_3) = u_i^p (a_1, x_2, x_3) \qquad \begin{array}{l} \forall x_2 \in [-a_2, a_2] \\ \forall x_3 \in [-a_3, a_3] \end{array}$$

$$u_i^p (x_1, -a_2, x_3) = u_i^p (x_1, a_2, x_3) \qquad \begin{array}{l} \forall x_1 \in [-a_1, a_1] \\ \forall x_3 \in [-a_3, a_3] \end{array} \qquad (3.3.6)$$

$$u_i^p (x_1, x_2, -a_3) = u_i^p (x_1, x_2, a_3) \qquad \begin{array}{l} \forall x_1 \in [-a_1, a_1] \\ \forall x_2 \in [-a_2, a_2] \end{array}$$

By taking Equation 3.3.5, the continuity condition in Equation 3.3.7 becomes:

$$u_i\left(a_1, x_2, x_3\right) - u_i\left(-a_1, x_2, x_3\right) = 2a_1\varepsilon_{i1}^0 \qquad \begin{aligned} &\forall x_2 \in [-a_2, a_2] \\ &\forall x_3 \in [-a_3, a_3] \end{aligned}$$

$$u_i\left(x_1, a_2, x_3\right) - u_i\left(x_1, -a_2, x_3\right) = 2a_2\varepsilon_{i2}^0 \qquad \begin{aligned} &\forall x_1 \in [-a_1, a_1] \\ &\forall x_3 \in [-a_3, a_3] \end{aligned} \qquad (3.3.7)$$

$$u_i\left(x_1, x_2, a_3\right) - u_i\left(x_1, x_2, -a_3\right) = 2a_3\varepsilon_{i3}^0 \qquad \begin{aligned} &\forall x_1 \in [-a_1, a_1] \\ &\forall x_2 \in [-a_2, a_2] \end{aligned}$$

This is the fundamental equation for applying the displacement boundary condition on the RVE. The factor $2a_j\varepsilon_{ij}^0$, is the displacement necessary to enforce a strain ε_{ij}^0 over a distance $2a_j$.

3.4 Implementation in Abaqus

The equations defined in 3.3.7 can be effectively implemented in Abaqus by leveraging its *constraint equations* (CE) module, as detailed in the Abaqus Standard User Manual [34]. It is essential to recognize that any linear constraint can be expressed as a linear equation. This entails specifying coefficients, denoted as $A_1, A_2, \ldots, A_n$, associated with displacement nodes labeled as $P, Q, \ldots, R$. Concurrently, i, j, k represent the degrees of freedom for nodes $P, Q, \ldots, R$. The formulation of a linear constraint is thus articulated as follows:

$$A_1 u_i^P + A_2 u_j^Q + \ldots A_n u_k^R = 0.$$

However, it is important to address two key challenges. The first challenge arises when the same node, such as u_i^P, is employed in one constraint, precluding its use in another. This dilemma is notably prominent along the edges of the Representative Volume Element (RVE), which are shared between two adjacent faces. Similarly, the vertices of the RVE are shared among three faces, amplifying the constraint conflict. Furthermore, using the first constraint from the equation set in 3.3.7 precludes its concurrent application in subsequent constraints.

The second challenge pertains to the precise positioning of the nodes. Ensuring that nodes on opposite faces of the RVE align perfectly necessitates meticulous mesh configuration within the RVE. To tackle the first challenge, we need to modify the equations within the set in 3.3.7. In contrast, to address the second challenge, the mesh within the RVE must be structured in such a way that it meticulously aligns nodes on opposite faces.

3.4.1 Modification in periodic boundary condition

The fundamental concept revolves around establishing relationships between edges and vertices that are diagonally opposite to one another. These equations can be derived by introducing Eq_{1i}, Eq_{2i}, and Eq_{3i} as follows:

$$\text{Eq}_{1i}(x_1, x_2, x_3) := u_i(a_1, x_2, x_3) - u_i(-a_1, x_2, x_3) = 2a_1\varepsilon_{i1}^0$$
$$\text{Eq}_{2i}(x_1, x_2, x_3) := u_i(x_1, a_2, x_3) - u_i(x_1, -a_2, x_3) = 2a_2\varepsilon_{i2}^0$$
$$\text{Eq}_{3i}(x_1, x_2, x_3) := u_i(x_1, x_2, a_3) - u_i(x_1, x_2, -a_3) = 2a_3\varepsilon_{i3}^0$$

In the Representative Volume Element (RVE), there are a total of 16 edges. Correspondingly, eight constraints can be formulated between these edges. We can categorize these constraints based on the orientation of the edges:

Edges Parallel to the x_1 Axis:

$$\text{Eq}_{2i}(x_1, a_2, a_3) - \text{Eq}_{3i}(x_1, a_2, a_3) \quad \text{for } \forall x_1 \in (-a_1, a_1)$$
$$\text{Eq}_{2i}(x_1, -a_2, a_3) + \text{Eq}_{31}(x_1, -a_2, a_3) \quad \text{for } \forall x_1 \in (-a_1, a_1)$$

This results into,

$$-u_1(x_1, -a_2, a_3) + u_1(x_1, a_2, -a_3) = 2a_2\varepsilon_{12} - 2a_3\varepsilon_{13} \qquad \forall x_1 \in (-a1, a1)$$
$$-u_2(x_1, -a_2, a_3) + u_2(x_1, a_2, -a_3) = 2a_2\varepsilon_{22} - 2a_3\varepsilon_{23} \qquad \forall x_1 \in (-a1, a1)$$
$$-u_3(x_1, -a_2, a_3) + u_3(x_1, a_2, -a_3) = 2a_2\varepsilon_{32} - 2a_3\varepsilon_{33} \qquad \forall x_1 \in (-a1, a1)$$
$$-u_1(x_1, -a_2, -a_3) + u_1(x_1, a_2, a_3) = 2a_2\varepsilon_{12} + 2a_3\varepsilon_{13} \qquad \forall x_1 \in (-a1, a1)$$
$$-u_2(x_1, -a_2, -a_3) + u_2(x_1, a_2, a_3) = 2a_2\varepsilon_{22} + 2a_3\varepsilon_{23} \qquad \forall x_1 \in (-a1, a1)$$
$$-u_3(x_1, -a_2, -a_3) + u_3(x_1, a_2, a_3) = 2a_2\varepsilon_{32} + 2a_3\varepsilon_{33} \qquad \forall x_1 \in (-a1, a1)$$

Edges Parallel to the x_2 Axis:

$$\text{Eq}_{1i}(a_1, x_2, a_3) - \text{Eq}_{3i}(a_1, x_2, a_3) \quad \text{for } \forall x_2 \in (-a_2, a_2)$$
$$\text{Eq}_{1i}(-a_1, x_2, a_3) + \text{Eq}_{31}(-a_1, x_2, a_3) \quad \text{for } \forall x_2 \in (-a_2, a_2)$$

Which results into,

$$-u_1(-a_1, x_2, a_3) + u_1(a_1, x_2, -a_3) = 2a_1\varepsilon_{11} - 2a_3\varepsilon_{13} \qquad \forall x_2 \in (-a2, a2)$$
$$-u_2(-a_1, x_2, a_3) + u_2(a_1, x_2, -a_3) = 2a_1\varepsilon_{21} - 2a_3\varepsilon_{23} \qquad \forall x_2 \in (-a2, a2)$$
$$-u_3(-a_1, x_2, a_3) + u_3(a_1, x_2, -a_3) = 2a_1\varepsilon_{31} - 2a_3\varepsilon_{33} \qquad \forall x_2 \in (-a2, a2)$$
$$-u_1(-a_1, x_2, -a_3) + u_1(a_1, x_2, a_3) = 2a_1\varepsilon_{11} + 2a_3\varepsilon_{13} \qquad \forall x_2 \in (-a2, a2)$$
$$-u_2(-a_1, x_2, -a_3) + u_2(a_1, x_2, a_3) = 2a_1\varepsilon_{21} + 2a_3\varepsilon_{23} \qquad \forall x_2 \in (-a2, a2)$$
$$-u_3(-a_1, x_2, -a_3) + u_3(a_1, x_2, a_3) = 2a_1\varepsilon_{31} + 2a_3\varepsilon_{33} \qquad \forall x_2 \in (-a2, a2)$$

Edges Parallel to the x_3 Axis:

$$\text{Eq}_{1i}(a_1, a_2, x_3) - \text{Eq}_{2i}(a_1, a_2, x_3) \quad \text{for } \forall x_3 \in (-a_3, a_3)$$
$$\text{Eq}_{1i}(-a_1, a_2, x_3) + \text{Eq}_{21}(-a_1, a_2, x_3) \quad \text{for } \forall x_3 \in (-a_3, a_3)$$

This makes, x_3 Edges parallel to height with $x_1 = a_1$, and $x_2 = a_2$

$$-u_1(-a_1, a_2, x_3) + u_1(a_1, -a_2, x_3) = 2a_1\varepsilon_{11} + 2a_2\varepsilon_{12} \qquad \forall x_3 \in (-a3, a3)$$
$$-u_2(-a_1, a_2, x_3) + u_2(a_1, -a_2, x_3) = 2a_1\varepsilon_{21} - 2a_2\varepsilon_{22} \qquad \forall x_3 \in (-a3, a3)$$
$$-u_3(-a_1, a_2, x_3) + u_3(a_1, -a_2, x_3) = 2a_1\varepsilon_{31} - 2a_2\varepsilon_{32} \qquad \forall x_3 \in (-a3, a3)$$
$$-u_1(-a_1, -a_2, x_3) + u_1(a_1, a_2, x_3) = 2a_1\varepsilon_{11} + 2a_2\varepsilon_{12} \qquad \forall x_3 \in (-a3, a3)$$
$$-u_2(-a_1, -a_2, x_3) + u_2(a_1, a_2, x_3) = 2a_1\varepsilon_{21} + 2a_2\varepsilon_{22} \qquad \forall x_3 \in (-a3, a3)$$
$$-u_3(-a_1, -a_2, x_3) + u_3(a_1, a_2, x_3) = 2a_1\varepsilon_{31} + 2a_2\varepsilon_{32} \qquad \forall x_3 \in (-a3, a3)$$

Similarly, equations for vertices can be derived, with a total of eight vertices in the RVE. Consequently, four constraints can be established between these vertices. To illustrate these constraints, we provide examples between points shared by specific pairs of faces:

Constraints between Points Shared by Front-Right-Top and Back-Left-Bottom Faces:

$$\text{Eq}_{3i}\left(a_1, a_2, -a_3\right) + \text{Eq}_{1i}\left(a_1, a_2, -a_3\right) + \text{Eq}_{2i}\left(-a_1, -a_2, -a_3\right),$$

which results,

$$-u_1(-a_1, -a_2, -a_3) + u_1(a_1, a_2, a_3) = 2a_1\varepsilon_{11} + 2a_2\varepsilon_{12} + 2a_3\varepsilon_{13}$$
$$-u_2(-a_1, -a_2, -a_3) + u_2(a_1, a_2, a_3) = 2a_1\varepsilon_{21} + 2a_2\varepsilon_{22} + 2a_3\varepsilon_{23}$$
$$-u_3(-a_1, -a_2, -a_3) + u_3(a_1, a_2, a_3) = 2a_1\varepsilon_{31} + 2a_2\varepsilon_{32} + 2a_3\varepsilon_{33}$$

Constraints between Points Shared by Back-Left-Top and Front-Right-Bottom Faces:

$$\text{Eq}_{3i}\left(a_1, -a_2, a_3\right) + \text{Eq}_{1i}\left(a_1, -a_2, a_3\right) - \text{Eq}_{3i}\left(a_1, a_2, -a_3\right),$$

which makes,

$$-u_1(-a_1, -a_2, a_3) + u_1(a_1, a_2, -a_3) = 2a_1\varepsilon_{11} + 2a_2\varepsilon_{12} - 2a_3\varepsilon_{13}$$
$$-u_2(-a_1, -a_2, a_3) + u_2(a_1, a_2, -a_3) = 2a_1\varepsilon_{21} + 2a_2\varepsilon_{22} - 2a_3\varepsilon_{23}$$
$$-u_3(-a_1, -a_2, a_3) + u_3(a_1, a_2, -a_3) = 2a_1\varepsilon_{31} + 2a_2\varepsilon_{32} - 2a_3\varepsilon_{33}$$

Constraints between Points Shared by Back-Right-Top and Front-Left-Bottom Faces:

$$-\text{Eq}_{1i}\left(a_1, a_2, a_3\right) + \text{Eq}_{3i}\left(a_1, a_2, a_3\right) + \text{Eq}_{2i}\left(a_1, -a_2, -a_3\right),$$

which results into,

$$u_1(-a_1, a_2, a_3) - u_1(a_1, -a_2, -a_3) = -2a_1\varepsilon_{11} + 2a_2\varepsilon_{12} + 2a_3\varepsilon_{13}$$
$$u_2(-a_1, a_2, a_3) - u_2(a_1, -a_2, -a_3) = -2a_1\varepsilon_{21} + 2a_2\varepsilon_{22} + 2a_3\varepsilon_{23}$$
$$u_3(-a_1, a_2, a_3) - u_3(a_1, -a_2, -a_3) = -2a_1\varepsilon_{31} + 2a_2\varepsilon_{32} + 2a_3\varepsilon_{33}$$

Constraints between Points Shared by Back-Right-Bottom and Front-Left-Top Faces:

$$-\text{Eq}_{2i}\left(a_1, -a_2, -a_3\right) + \text{Eq}_{3i}\left(a_1, -a_2, -a_3\right) + \text{Eq}_{1i}\left(-a_1, a_2, -a_3\right),$$

and

$$-u_1(-a_1, a_2, -a_3) + u_1(a_1, -a_2, a_3) = 2a_1\varepsilon_{11} - 2a_2\varepsilon_{12} + 2a_3\varepsilon_{13}$$
$$-u_2(-a_1, a_2, -a_3) + u_2(a_1, -a_2, a_3) = 2a_1\varepsilon_{21} - 2a_2\varepsilon_{22} + 2a_3\varepsilon_{23}$$
$$-u_3(-a_1, a_2, -a_3) + u_3(a_1, -a_2, a_3) = 2a_1\varepsilon_{31} - 2a_2\varepsilon_{32} + 2a_3\varepsilon_{33}$$

This approach systematically addresses constraints between edges and vertices, providing a comprehensive framework for implementing the required relationships within the Abaqus environment. For convenience all equations can be summarized again.

3.4.1.1 Equations for faces

$$u_i(a_1, x_2, x_3) - u_i(-a_1, x_2, x_3) = 2a_1\varepsilon_{i1}^0 \qquad \begin{array}{l} \forall x_2 \in (-a_2, a_2) \\ \forall x_3 \in (-a_3, a_3) \end{array}$$

$$u_i(x_1, a_2, x_3) - u_i(x_1, -a_2, x_3) = 2a_2\varepsilon_{i2}^0 \qquad \begin{array}{l} \forall x_1 \in (-a_1, a_1) \\ \forall x_3 \in (-a_3, a_3) \end{array}$$

$$u_i(x_1, x_2, a_3) - u_i(x_1, x_2, -a_3) = 2a_3\varepsilon_{i3}^0 \qquad \begin{array}{l} \forall x_1 \in (-a_1, a_1) \\ \forall x_2 \in (-a_2, a_2) \end{array}$$

3.4.1.2 Equations for edges

$$-u_i(x_1, -a_2, a_3) + u_i(x_1, a_2, -a_3) = 2a_2\varepsilon_{i2} - 2a_3\varepsilon_{i3} \qquad \forall x_1 \in (-a1, a1)$$
$$-u_i(x_1, -a_2, -a_3) + u_i(x_1, a_2, a_3) = 2a_2\varepsilon_{i2} + 2a_3\varepsilon_{i3} \qquad \forall x_1 \in (-a1, a1)$$
$$-u_i(-a_1, x_2, a_3) + u_i(a_1, x_2, -a_3) = 2a_1\varepsilon_{i1} - 2a_3\varepsilon_{i3} \qquad \forall x_2 \in (-a2, a2)$$
$$-u_i(-a_1, x_2, -a_3) + u_i(a_1, x_2, a_3) = 2a_1\varepsilon_{i1} + 2a_3\varepsilon_{i3} \qquad \forall x_2 \in (-a2, a2)$$
$$-u_i(-a_1, a_2, x_3) + u_i(a_1, -a_2, x_3) = 2a_1\varepsilon_{i1} - 2a_2\varepsilon_{i2} \qquad \forall x_3 \in (-a3, a3)$$
$$-u_i(-a_1, -a_2, x_3) + u_i(a_1, a_2, x_3) = 2a_1\varepsilon_{i1} + 2a_2\varepsilon_{i2} \qquad \forall x_3 \in (-a3, a3)$$

3.4.1.3 Equations for vertices

$$-u_i(-a_1, -a_2, -a_3) + u_i(a_1, a_2, a_3) = 2a_1\varepsilon_{i1} + 2a_2\varepsilon_{i2} + 2a_3\varepsilon_{i3}$$
$$-u_i(-a_1, -a_2, a_3) + u_i(a_1, a_2, -a_3) = 2a_1\varepsilon_{i1} + 2a_2\varepsilon_{i2} - 2a_3\varepsilon_{i3}$$
$$u_i(-a_1, a_2, a_3) - u_i(a_1, -a_2, -a_3) = -2a_1\varepsilon_{i1} + 2a_2\varepsilon_{i2} + 2a_3\varepsilon_{i3}$$
$$-u_i(-a_1, a_2, -a_3) + u_i(a_1, -a_2, a_3) = 2a_1\varepsilon_{i1} - 2a_2\varepsilon_{i2} + 2a_3\varepsilon_{i3}$$

3.4.2 Plugin for analysis

As discussed in the previous section, the manual implementation of these equations can be a laborious process. Establishing connections between a single node and its three distinct degrees

of freedom (DOFs) with the node on the opposite face is time-consuming. To streamline this task, we have developed a custom plugin for Abaqus, which automates this process. To validate the code and assess the results produced by this plugin, we utilize Equation 3.3.3 for homogenization, and the outcomes are compared with those derived from Equation 3.2.1.

The plugin operates through six main steps. Firstly, the user specifies the parameters for both the fiber and matrix materials. Next, the plugin creates the necessary geometry based on the predefined sizing parameters for the hexagonal structure. Following this, the plugin generates a mesh that ensures nodes are positioned consistently on opposite faces. Subsequently, it defines the static linear perturbation step. It then implements periodic boundary conditions. Finally, the plugin submits the job for analysis, and in the last step, post-processing is performed. A visual representation of this workflow can be found in Figure 3.4.1.
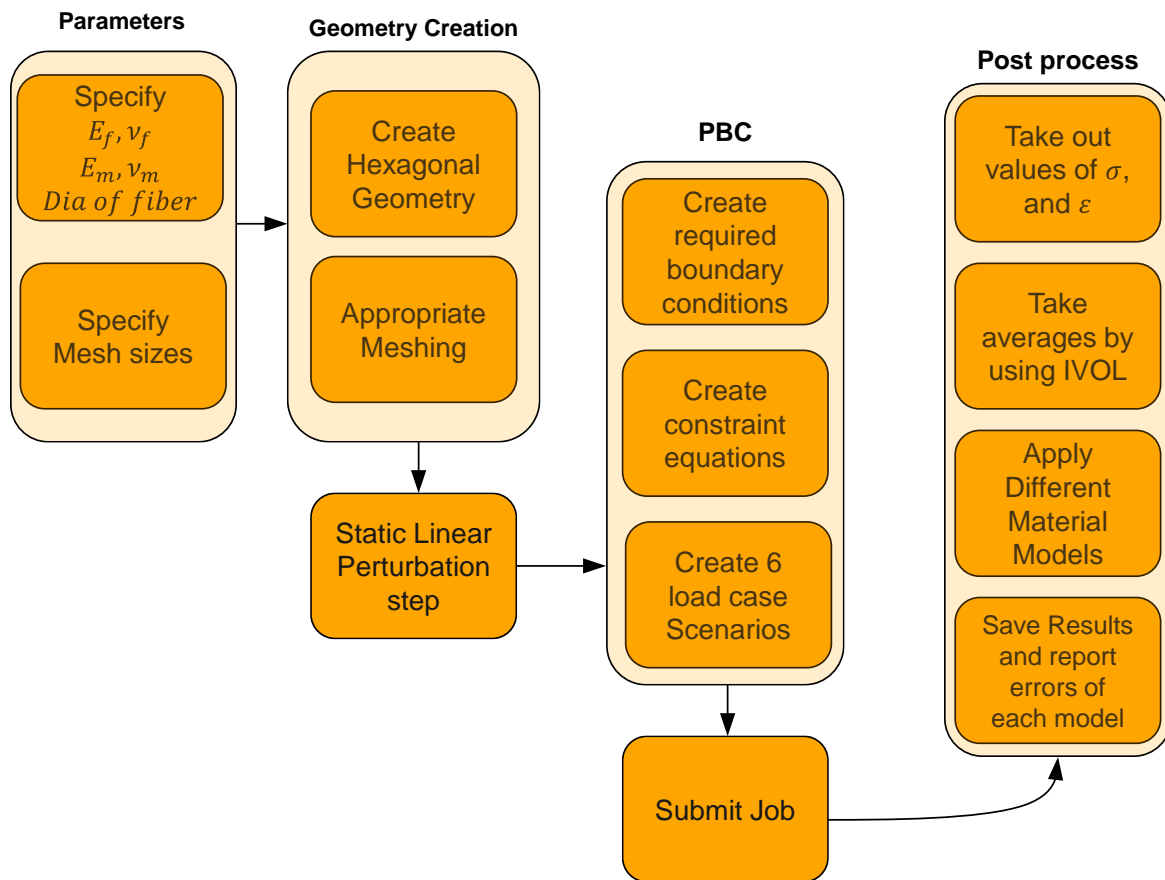
Figure 3.4.1: Flow diagram of the plugin for the linear analysis

Now the details of each step is given in the following sections.

3.4.2.1 Parameters

In parameters, we have to specify the material properties of the fiber and matrix material. Moreover, we have to specify the dimensions of RVE. Instead of specifying the dimensions of RVE explicitly, we can express them in terms of volume fraction of fiber and the diameter of fiber.

Let us define the volume of the RVE as $Vol_{RVE} = 2a_1 \times 2a_2 \times 2a_3$. The values for the parameters a_1, a_2, and a_3 can be determined based on other parameters. Suppose we have the number of fibers in the RVE denoted as n. In this context, we can specify the diameter of a single fiber as d_f. The volume of an individual fiber, Vol_f, can be calculated as:

$$Vol_f = n\pi \left(\frac{d_f}{2}\right)^2 a_1$$

Now, let's introduce the concept of the volume fraction of the fibers, denoted as V_f, defined by the equation:

$$V_f = \frac{Vol_f}{Vol_{RVE}} = \frac{n\pi \left(\frac{d_f}{2}\right)^2 a_1}{8a_1 a_2 a_3}$$

Utilizing hexagonal symmetry, as illustrated in Figure 3.3.2, we can deduce that:

$$\tan 60° = \frac{a_3}{a_2} = \sqrt{3} \implies a_3 = \sqrt{3}a_2$$

Given that there are two fibers, as shown in Figure 3.3.6, we can express a_2 as follows:

$$a_2 = \sqrt{\frac{\pi}{2\sqrt{3}Vol_f} \times \left(\frac{d_f}{2}\right)^2}$$

The final dimension, a_1, is a parameter that can be chosen arbitrarily. In this context, we have set it as:

$$a_1 = \frac{a_2}{4}$$

This approach allows for the determination of the RVE dimensions based on the specified number of fibers, fiber diameter, and volume fraction of fiber.

3.4.2.2 Geometry Creation Module

This module is dedicated to the creation of the RVE geometry, which is dependent on the specified dimensions of the RVE and the diameter of the fibers. Additionally, this step involves generating the appropriate mesh according to user sizes. Once these steps are completed, the geometry is prepared for subsequent analysis.

3.4.2.3 Analysis Step

At this stage, the primary focus is on a static linear perturbation analysis, which is a linear analysis method supported by Abaqus [37]. Within this analysis, it is crucial to specify the desired *field output variables* [34]. In our work, the following variables were used in sequence: 'NE', 'LE', 'E', 'S', 'U', and 'IVOL'.

- 'NE' corresponds to the nominal strain, defined within Abaqus conventions as $NE = \boldsymbol{v} - \boldsymbol{I}$, where $\boldsymbol{v}$ represents the left stretch 2.1.11.

- 'LE' represents the logarithmic strain, denoted as $LE = \ln \boldsymbol{v}$.

- 'E' denotes the total strain, a parameter calculated by Abaqus through the integration of the strain rate in the material frame of reference. It can be expressed as:

$$\varepsilon^{n+1} = \Delta \boldsymbol{R} \cdot \varepsilon^n \cdot \Delta \boldsymbol{R}^T + \Delta \varepsilon$$

  Here, ε^{n+1} and ε^n represent the total strains at increments $n+1$ and n, respectively. $\Delta \boldsymbol{R}$ is the incremental rotation tensor, and $\Delta \varepsilon$ is the total strain increment from increment n to $n+1$. The latter is obtained through integration.

$$\Delta \varepsilon = \int_{t^n}^{t^{n+1}} \boldsymbol{d} \, dt$$

  , where $\boldsymbol{d}$ is the symmetric part of the $\boldsymbol{l}$ 2.2.15.

- 'S' refers to the Cauchy stress 2.1.13.

- 'U' accounts for the displacements in all three axes.

- 'IVOL' represents the integration point volume. It is pivotal for calculating the averages of stress and strain. 'IVOL' is the volume associated with a specific integration point. In the case of a reduced integration element (i.e., an element with only one integration point), 'IVOL' equates to the element's volume. For fully integrated elements, 'IVOL' represents some fraction of the element volume.

3.4.2.4 Periodic Boundary Condition (PBC) Module

This module addresses the setup of essential boundary conditions. Boundary conditions are specified at reference points within the geometry [36]. To create these conditions, nine reference points are established. Unit displacement boundary conditions are applied to these reference points for normal loading cases, while pure shear loading cases are assigned 0.5 displacement boundary conditions. These boundary conditions are specified using the load cases module in Abaqus [35].

To proceed, a pair function is created to determine two sets: 'master nodes' and 'slave nodes.' These nodes should be arranged such that nodes with the same positions are correlated with each other. The pair function operates as follows:

- It calculates the bounding box of the 'slave nodes' and establishes an absolute search tolerance based on the relative tolerance and the bounding box's size.

- The function then computes the coordinates to search for in the 'master nodes' by sub-tracting the periodicity vector from each coordinate in the 'slave nodes.'

- It searches for the closest nodes in the 'master nodes' for each of these coordinates within the specified search tolerance. If there is no match, an error is raised. In the case of multiple matches, an error is also raised. Otherwise, the matched nodes are appended to the 'matched master nodes set,' and the 'slave nodes' are added to the 'matched slave nodes set.'

- Finally, the function returns both lists as a tuple [41].

The pair function is iterated for all three pairs, namely, front and back faces, left and right faces, and top and bottom faces. From these faces, edges and vertices are extracted, and the necessary pair sets are created as detailed in section 3.4.1.

With the required sets containing ordered nodes in place, constraint equations can be established. The code snippet for creating constraint equations is provided in 1. After that, the job can be submitted.

3.4.2.5 Post processing

This module is designed for the evaluation of material homogenization scenarios, specifically for mechanical analysis in the context of engineering applications. The code performs a series of steps to derive simplified material models based on stress and strain data extracted from an output database (ODB) file generated by Abaqus. These are the main steps and functionalities of this module:

- Data Extraction from Abaqus ODB: The first step involves extracting stress and strain data from the ODB file. This data represents the response of a complex, anisotropic material model subjected to various loads and conditions.

- IVOL Property Averaging: The code uses the IVOL property to calculate the average stress and strain values from the extracted data. This is a crucial step in the homogenization process to obtain representative material properties.

- Homogenization Equations: Utilizing mathematical equations for material homogenization Equation 3.3.3, the code constructs a linear anisotropic material model. This model captures the behavior of the original complex material and serves as a reference for comparison.

- Simplified Material Models: The code proceeds to simplify the linear anisotropic material model. It derives several simpler material models, including:

  - Monotropic model (One plane symmetry, 13 unknowns)

  - Orthotropic model (Two orthogonal planes symmetry, 9 unknowns)

  - Transverse isotropic model for each of the three principal axes (x, y, z) (Symmetry about one axis, 5 unknowns)

  - Isotropic model (No prefered direction, 2 unknowns)

Listing 1 Code snippet for creating constraints between two sets

```python
def equation_constraint_create_faces(Model,master_set_name, slave_set_name,
                                     prefix_constraint ,
                                     coef_eps,eps_column):
    """
        Create equation constraint betweeen faces

        Inputs:
            Model - A model object from a Model Database
            master_set_name - The name of the master set name
            slave_set_name  - The name of the slave set name
            prefix_constraint - Prefix that will be added in the definition of
    ↪   the constraint
            coef_eps - The coefficent that will appear for the DOF1, DOF2, and
    ↪   DOF3
            eps_column - The index of epsij where j is the eps_column, it can
    ↪   be 1,2,3
    """
    # Here terms are defined in tuples it can be any number but here we have
    ↪    defined 4 terms
    # This tuple is arranged as (coefficent, set_name, DOF)
    coef_master = -1.0
    coef_slave  = 1.0
    for dof in [1,2,3]:
        constraint_name = prefix_constraint + '_DOF_' + str(dof)
        strain_name = 'eps' + str(dof) + str(eps_column) # epsir
        Model.Equation(name=constraint_name, terms=(
                (coef_master, master_set_name, dof),
                (coef_slave,  slave_set_name,  dof),
                (coef_eps, strain_name, 1),
                ))
```

- Error Measurement: To evaluate the quality of these simplified material models, the code measures the differences between the simplified material properties and the anisotropic material model properties. These differences, or errors, provide insights into how well the simplified models approximate the complex behavior. The error is measured as,

$$Error = \frac{\|\mathbf{C} - \mathbf{C}_{aniso}\|_{L_2}}{\|\mathbf{C}_{aniso}\|_{L_2}}$$

- CSV File Summary: The code compiles a summary of the results, including error values, for each of the derived material models. This summary is saved in a CSV (Comma-Separated Values) file, providing a clear overview of the performance of each simplified material model in relation to the original anisotropic material.

In summary, this code automates the process of evaluating various homogenization scenarios for material properties. It leverages stress and strain data from finite element simulations, applies mathematical homogenization equations, simplifies the material models into different categories, and quantifies the errors introduced by these simplifications. The results are then organized and saved in a CSV file for further analysis and reference. This tool is valuable for engineers and researchers working with complex materials and seeking to develop accurate yet computationally efficient material models for their simulations.

3.4.3 Example Problem

At this section the results of plugin and Equation 3.2.1 will be compared. For this an example problem will be set. The properties are defined in Table 3.4.1.

Young's moduli	Poisson's ratio	
$E_f = 240\,\text{GPa}$	$\nu_f = 0.2$	$V_f = 0.4$
$E_m = 3.12\,\text{GPa}$	$\nu_m = 0.38$	$d_f = 7\,\mu\text{m}$

Table 3.4.1: Example material data. V_f is the volume fraction of fiber and d_f is the diameter of the fiber.

Here the fiber material and matrix are assumed to be isotropic but their values are quite different from each other. By using Equation 3.2.1, we can obtain results as shown in Table 3.4.2.

Young's moduli	Poisson's ratio	Shear Moduli
$E_1 = 98\,306\,\text{MPa}$	$\nu_{12} = 0.298$	$G_{12} = 2594\,\text{MPa}$
$E_2 = 6552\,\text{MPa}$	$\nu_{23} = 0.6$	$G_{13} = G_{12}$
$E_3 = E_2$	$\nu_{13} = \nu_{12}$	

Table 3.4.2: Results by analytical homogenization.

Coming to the numerical homogenization part, the parameters a_1, a_2, and a_3 for RVE will become:

$$a_1 = 1.3175\,\mu\text{m},$$
$$a_2 = 5.270\,\mu\text{m},$$
$$a_3 = 9.128\,\mu\text{m}.$$

First looking at the anisotropy, and see which material simplification can be used.

The table 3.4.3 shows that the transverse isotropy about $2-3$ plane is good enough because the error between orthotropy and the transverse isotropy about $2-3$ plane is negligible. The next step is to compare the values of material constants with respect to the number of elements in RVE. The results are shown in Table 3.4.4. It can be seen that the results are converging towards values of theoretical homogenization.

Material Model	Error
Transverse isotropy about $2-3$ plane	5.48×10^{-6}
Transverse isotropy about $1-3$ plane	0.91
Transverse isotropy about $1-2$ plane	0.75
Isotropy	0.81
Orthotropy	1.9×10^{-6}
Monotropy	1.9×10^{-6}

Table 3.4.3: Comparisons of different material models.

Number of elements	E_1	E_2	ν_{12}	ν_{23}	G_{12}
5152	98011.99171	7491.609319	0.29899	0.538909	2586.435671
13104	98182.26208	7472.784428	0.298905	0.540458	2583.182615
22400	98201.86388	7470.192299	0.298896	0.540653	2582.64296
56800	98270.90616	7470.363608	0.298921	0.540692	2582.163526

Table 3.4.4: Results by numerical homogenization.

This provides assurance that the developed code and equations yield accurate results. The deformation modes for the six loading cases are illustrated in (3.4.2, 3.4.3, 3.4.4, 3.4.5, 3.4.6, 3.4.7).
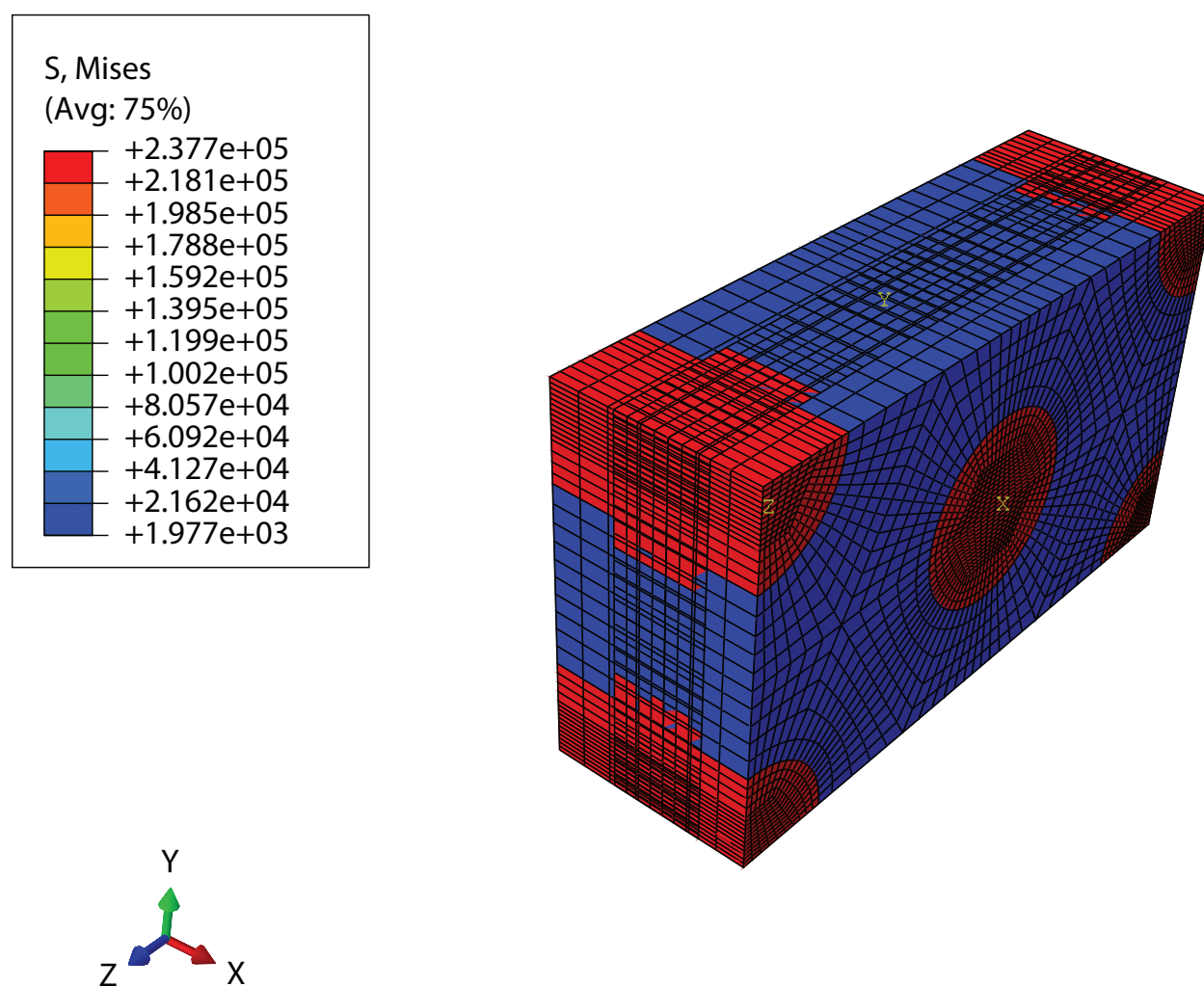
Figure 3.4.2: Mode of deformation for the loading case 1 $\left(\varepsilon_{11}^0\right)$
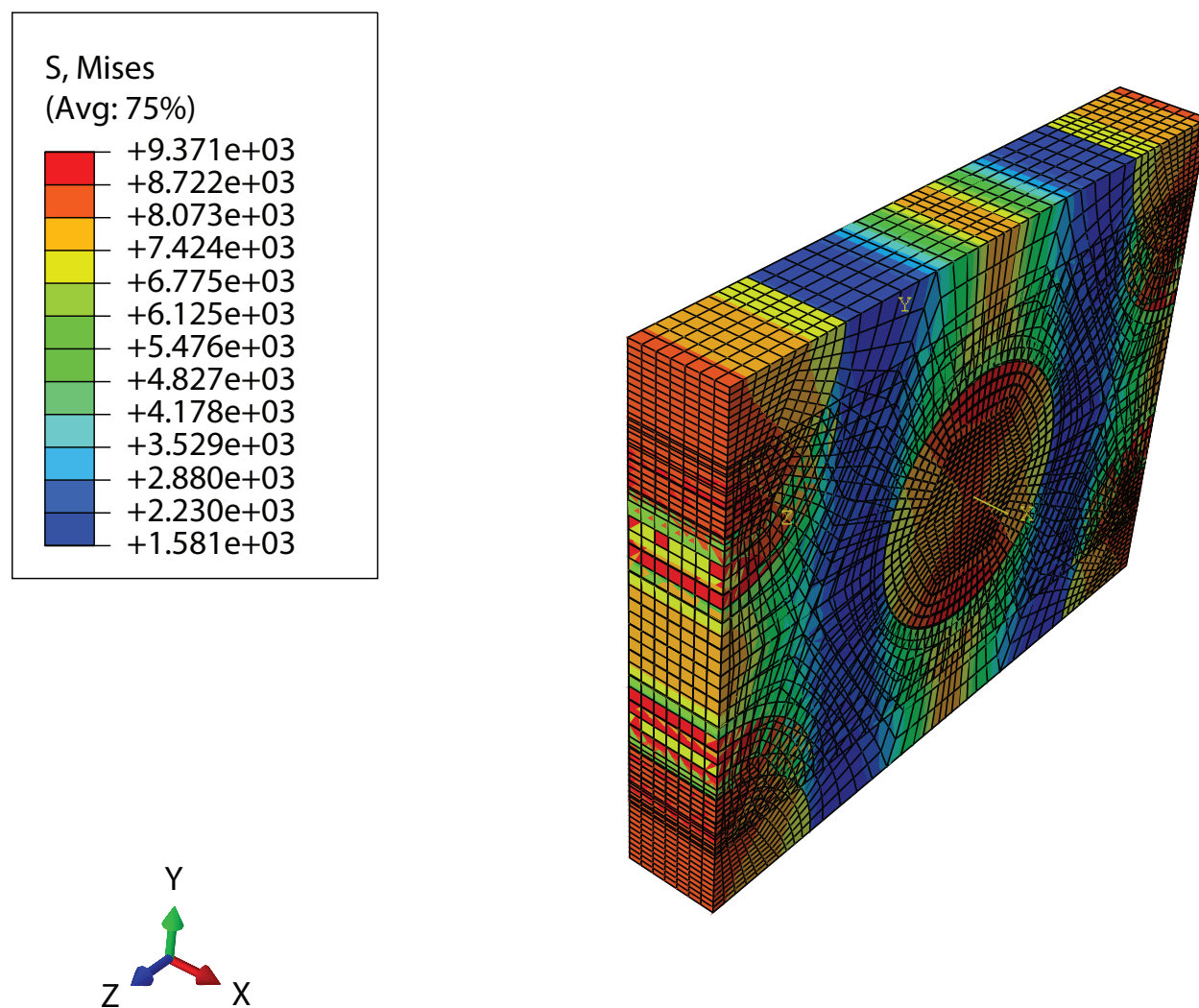
Figure 3.4.3: Mode of deformation for the loading case 2 ε_{22}^0
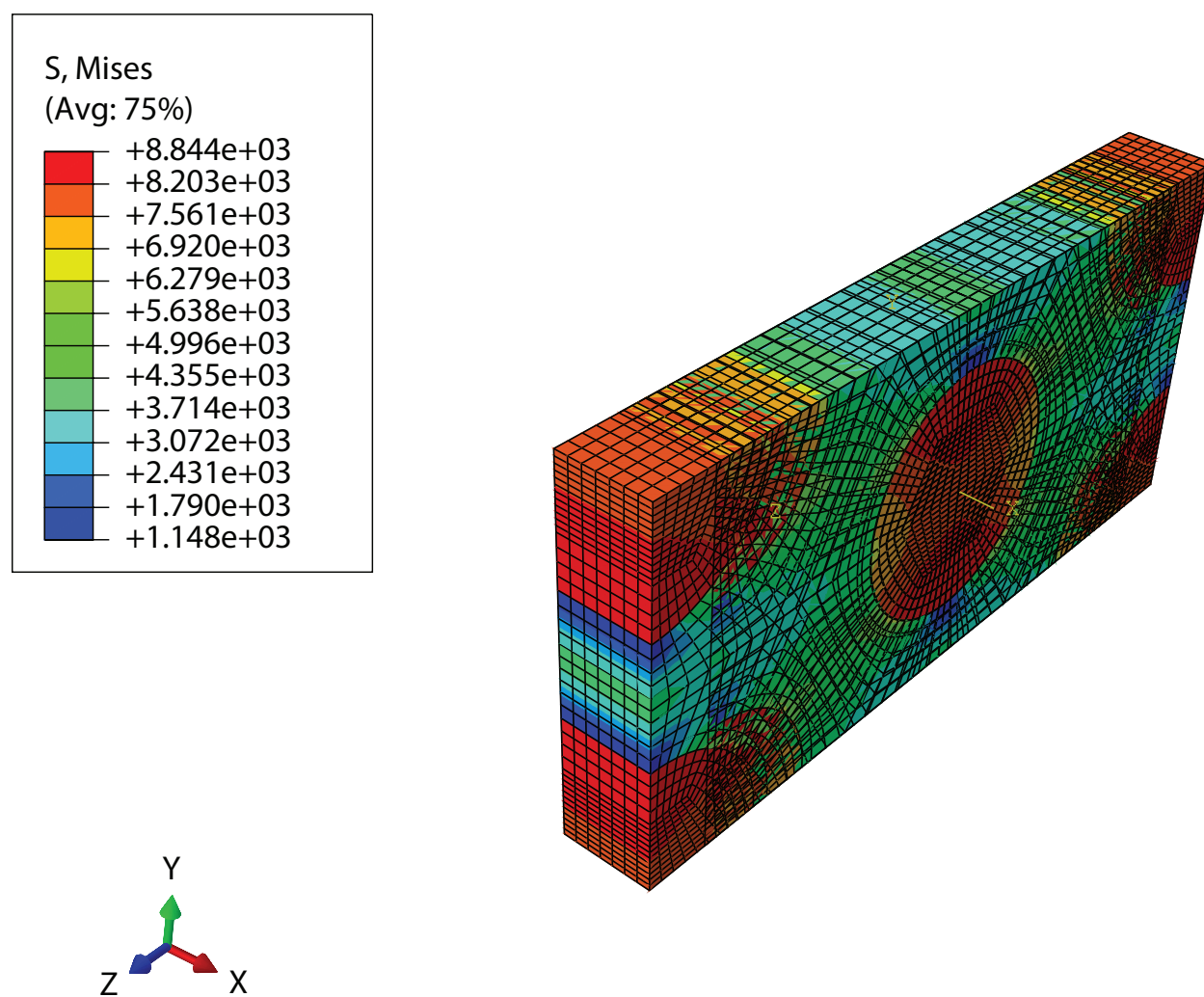
Figure 3.4.4: Mode of deformation for the loading case 3 ε_{33}^0

S, Mises
(Avg: 75%)

	+6.608e+03
	+6.064e+03
	+5.521e+03
	+4.977e+03
	+4.433e+03
	+3.890e+03
	+3.346e+03
	+2.803e+03
	+2.259e+03
	+1.716e+03
	+1.172e+03
	+6.289e+02
	+8.537e+01
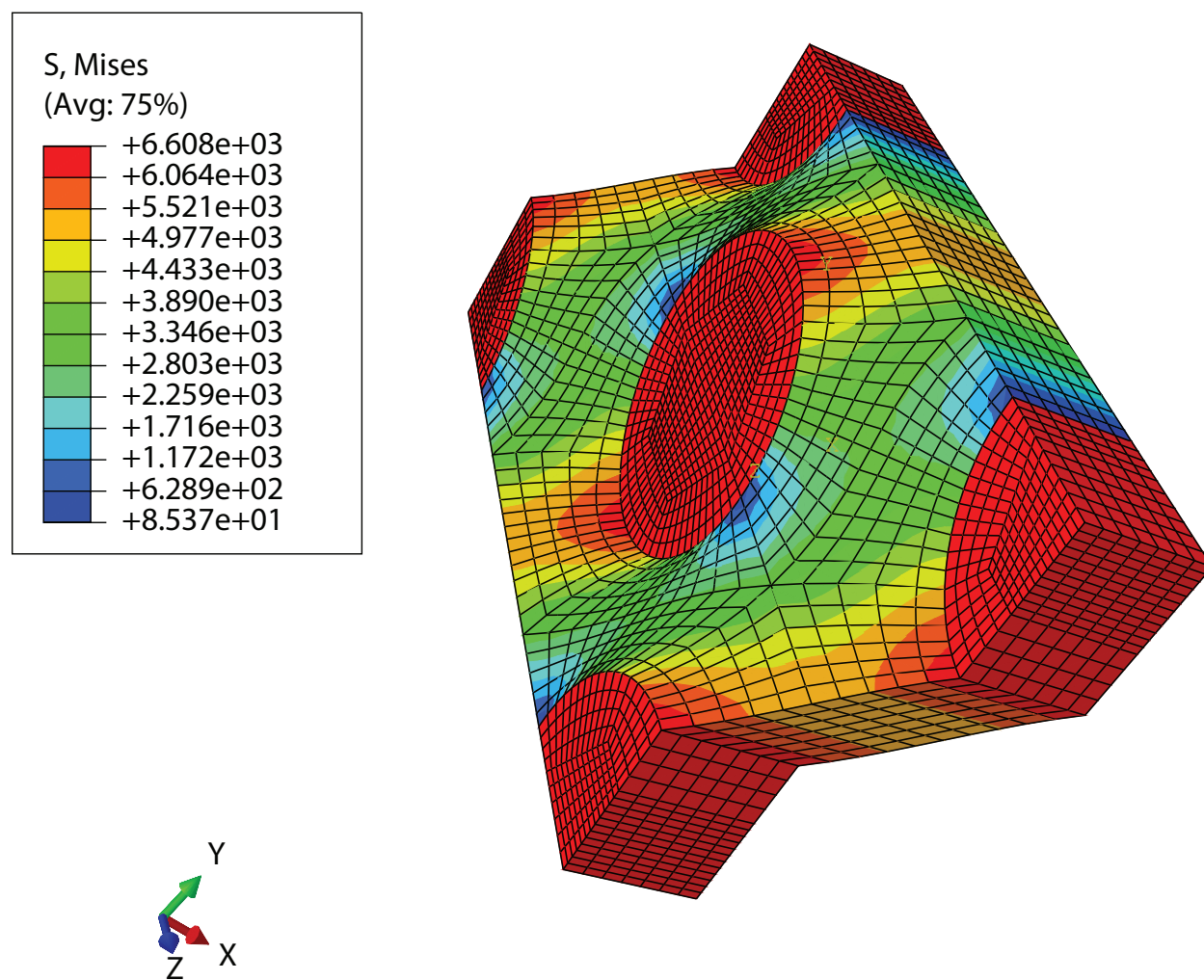
Figure 3.4.5: Mode of deformation for the loading case 4 ε_{12}^0
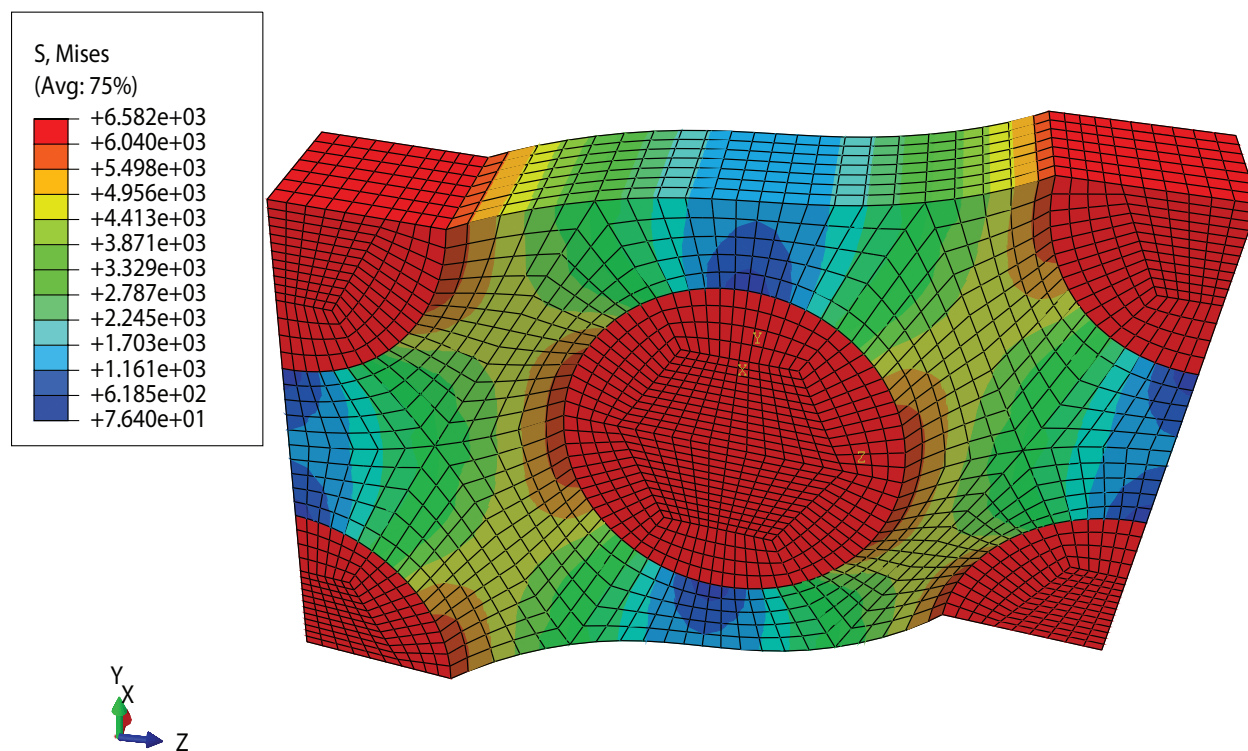
Figure 3.4.6: Mode of deformation for the loading case 5 ε_{13}^0
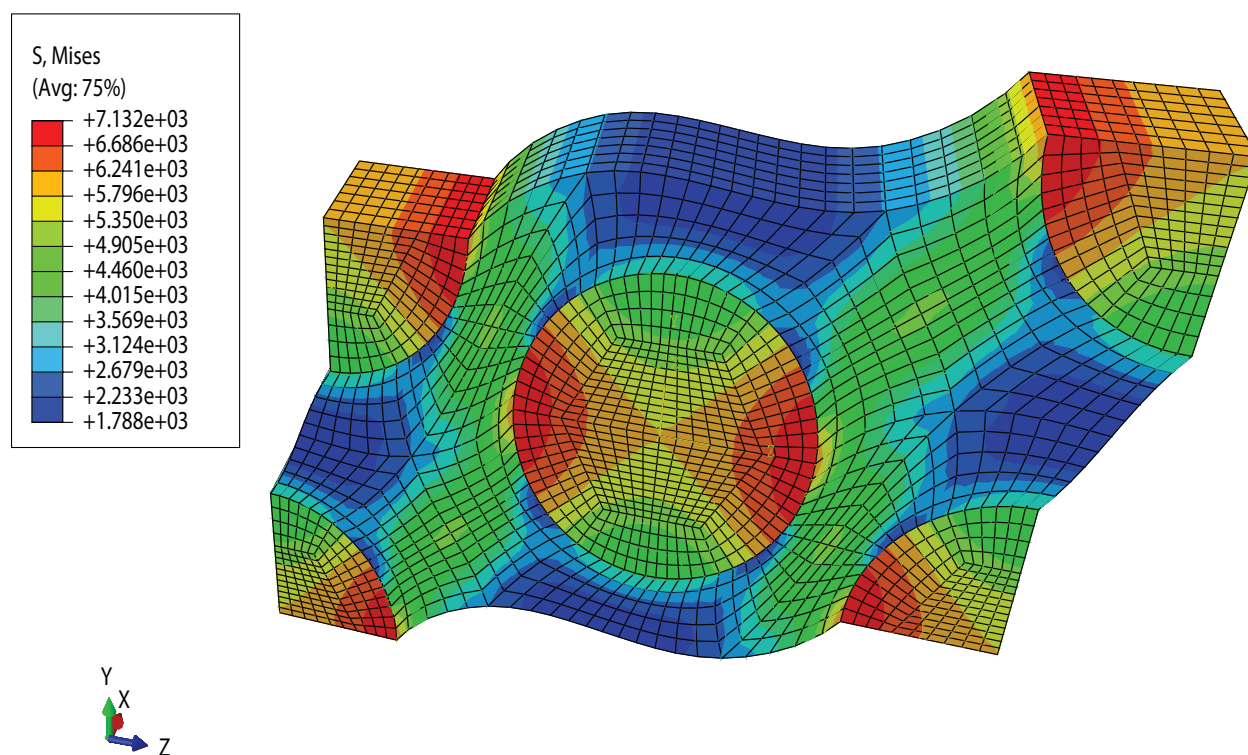
Figure 3.4.7: Mode of deformation for the loading case 6 ε_{23}^0

Chapter 4

Modeling of Air springs

This chapter commences by introducing air springs, providing insights into their operational mechanisms and applications. It subsequently delves into the modeling of the bellow component. The chapter then focuses on necessary modifications to the plugin, specifically addressing the incorporation of nonlinear hyperelastic responses. A brief discussion follows concerning material models for both rubber and chord materials. The linear strain-based anisotropic model is presented, showcasing its results. The chapter further explores the outcomes of the nonlinear strain-based anisotropic model and proceeds to depict the results derived from different models based on invariant-based modeling.

4.1   Introduction

Air springs are kind of the suspension system which are used in the vehicles. The roads on which vehicle moves are always uneven and often cause vehicles to vibrate, making them less safe and uncomfortable. These vibrations modes can arise in all six degree of freedom of the vehicle, as shown in Figure 4.1.1. Yet the vertical one is the most relevant. However, the lateral vibration mode is also relevant for the rail-bound vehicles.

One of the main the main advantage of using air springs suspension system that it can adapt itself according to the load. The vibration response of the vehicle is quite different when the vehicle is fully loaded or empty. This effect is more paramount in light vehicles since the difference of mass between empty and fully loaded vehicle is quite large.

The fundamental concept of this system is elucidated in Figure 4.1.2. A position sensor is affixed to the wheel axle, continuously monitoring the body's height—whether it's fully loaded or empty. This sensor incorporates a coil within its casing, housing a ferromagnetic core that moves vertically. When the distance between the axle and the vehicle body changes, the sensor lever rotates. The core's movement within the coil, driven by a crank mechanism, alters the coil's inductance. The electronic control unit measures this inductance and converts it into a proportional displacement signal. Utilizing height information, the control unit dynamically adjusts the solenoid, regulating the release of air into the air springs. By adding or removing air, the system aligns the actual height with the target height and achieves the desired stiffness in the air spring.
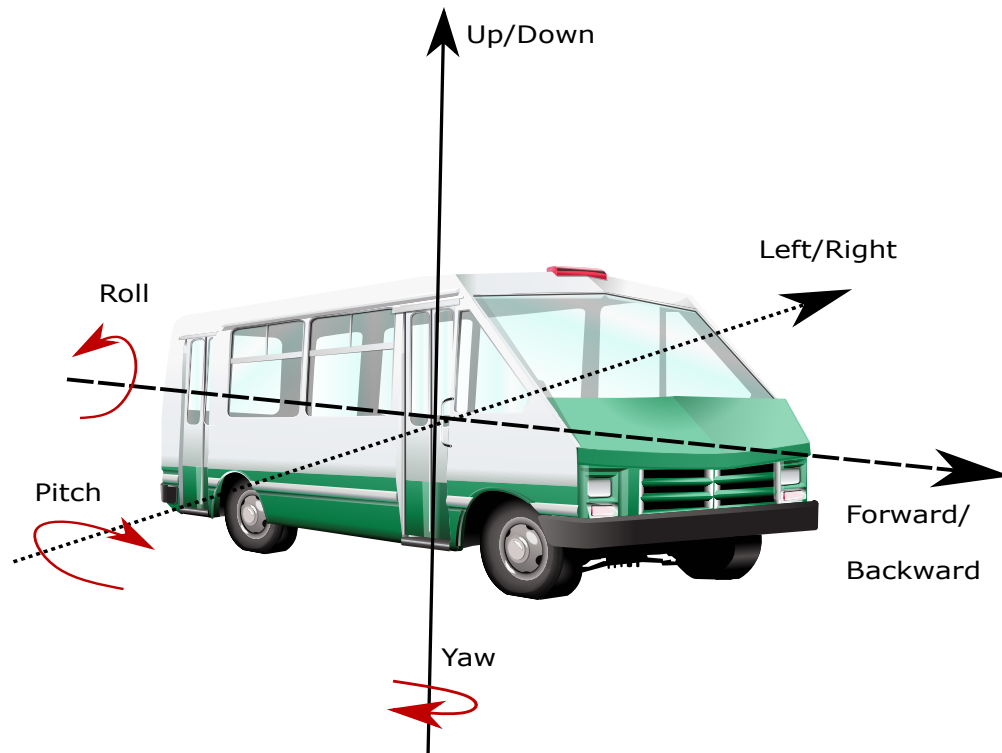
Figure 4.1.1: Types of vibration modes for a vehicle

The primary elements of the air spring are illustrated in Figure 4.1.3. This figure presents a cross-sectional view below, revealing a structure comprising two fabric layers enclosed by two elastomer layers. The functions of each component are succinctly outlined in the figure. The vertical motion of the piston responds to the applied load, encountering resistance from the air-filled bellows. This resistance can be elucidated through the ideal gas theory, where pressure and volume exhibit an inverse relationship. Hence, an augmentation of air within the bellows induces a movement of the piston in the opposite direction.

Air springs find diverse applications across various industries, showcasing their versatility and benefits:

1. **Buses:** Globally, the demand for optimal ride comfort has led to the widespread incorporation of air springs in buses. Nearly 100

2. **Trucks:** Air springs are integral to truck bodies worldwide, particularly for transporting sensitive goods and facilitating the interchange of swap bodies and semi-trailers. Air suspension in trucks is commonly employed to adjust the vehicle body height during loading and unloading operations.

3. **Machine Suspension:** Air springs play a crucial role in stationary equipment, effectively isolating vibrations in sensitive machinery and measurement equipment from ambient factors. This not only protects the machinery but also prevents disruptive vibrations that could harm the environment. The suspension or bearings can be finely tuned to achieve a very low natural frequency.

Electronic unit   Sensor   Air spring

Air

Solenoid

Zoomed

Sleeve type air spring

Air

Bellow

Piston

Guided on outside
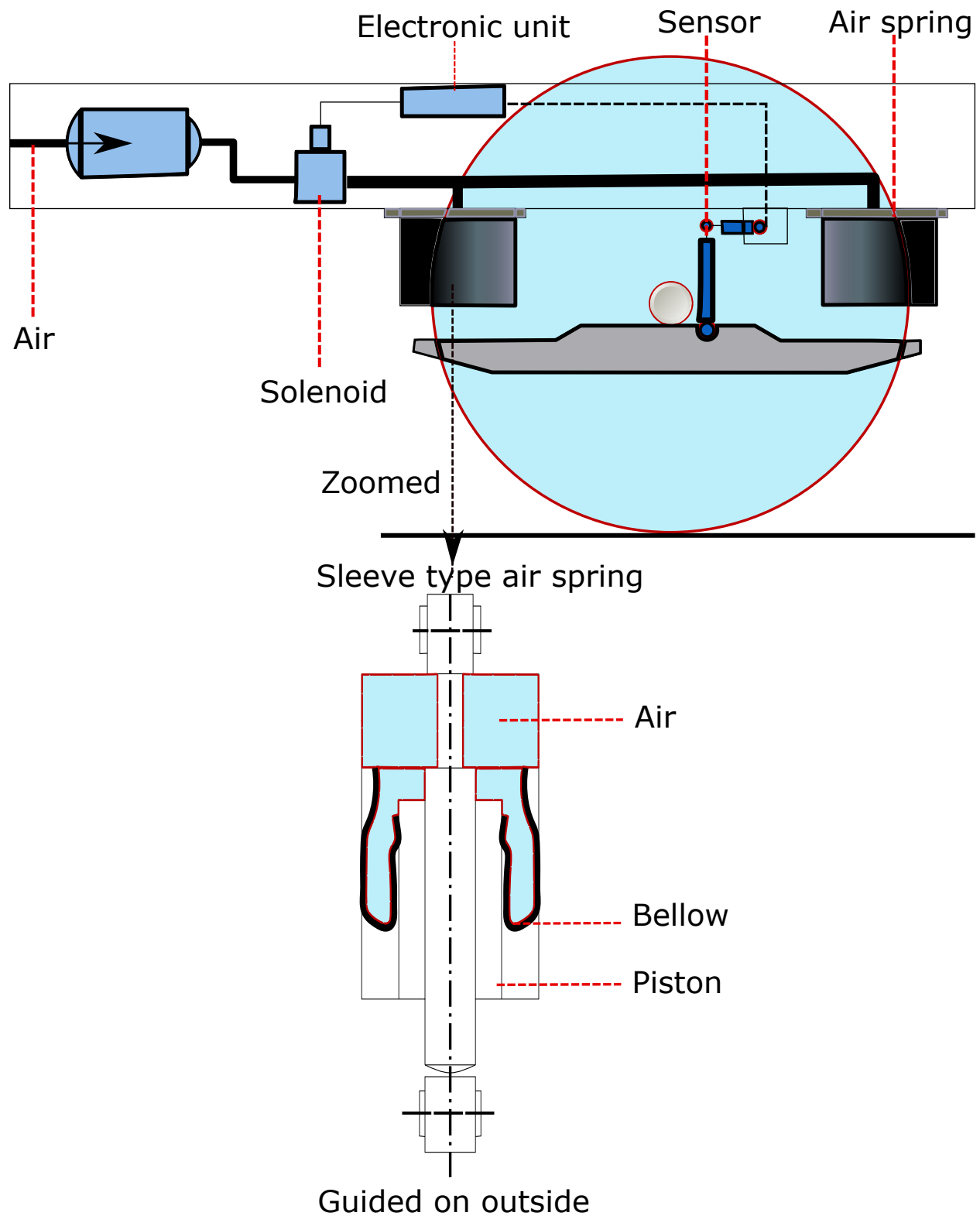
Figure 4.1.2: Schematic of electronic control system

Crimping: The method of permanently sealing the bellows to the bead plate.

Air Inlet: Provides the diaphragm with air.

Top Plate: Connects the air spring to the vehicle chasis.

Fixing Studs: Secures the air spring to the vehicle chasis.

Outer Cover: Made of elastomer rubber.

Second Ply: Fabric reinforced rubber layed opposite to first ply.

First Ply: Fabric reinforced rubber with chords at specific angle.

Inner Layer: Made of elastomer rubber.

Piston: Provides lower mouting arrangement for the air spring in the form of tapered holes or studs.

Figure 4.1.3: Main components of air spring

4. **Rail-bound Vehicles:** Air springs are extensively employed in trains across local transportation networks, including hybrid above-and-below-ground and subway trains, as well as long-distance trains worldwide. The superior ride comfort provided by air springs enables high-speed travel due to the smooth operation of bogies.

5. **Trailers and Semi-trailers:** Across the globe, trailers and semi-trailers are equipped with air springs to transport delicate cargo and safeguard the vehicle body. Similar to trucks, the ability to control air pressure enables load-dependent braking, and sophisticated control systems can raise axles when the vehicle is partially loaded or unloaded.

6. **Drivers' Seats:** The use of air-sprung driver's seats is a widespread practice globally. This approach not only enhances cab comfort but also plays a crucial role in preventing driver fatigue and maintaining their health.

7. **Cabs:** Certain commercial vehicle manufacturers enhance ride comfort and driver-friendliness by incorporating air springs in truck cabs, contributing to an improved overall driving experience.

8. **Cars:** While traditional steel springs were once complemented by air springs in the rear axle, modern vehicles increasingly feature fully load-bearing air springs, especially on the rear axle, which typically bears the most significant load difference. However, the full benefits of enhanced ride comfort are realized when both the front and rear axles boast full air suspension.

Some illustrations of their applications are shown in Figure 4.1.4, Figure 4.1.5.

Buses and Trucks
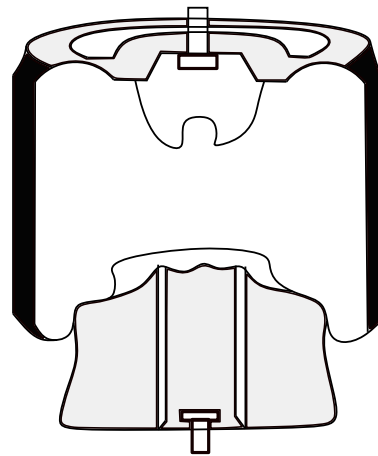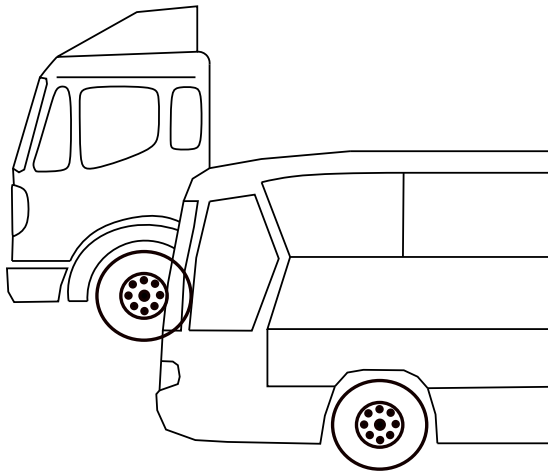
Machine Suspension
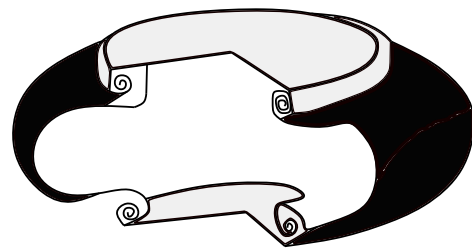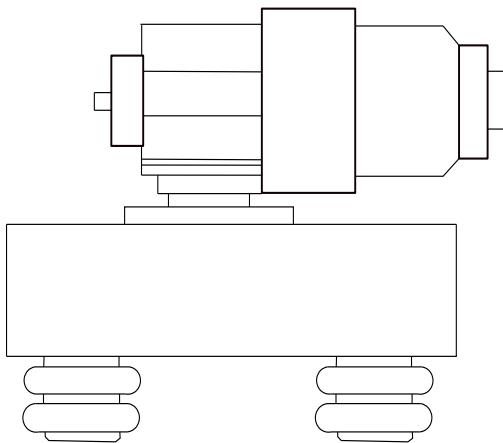
Rail-bound vehicles
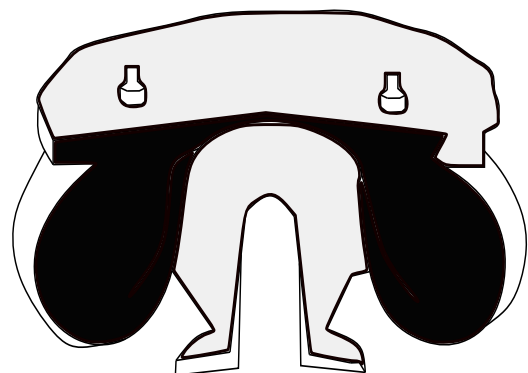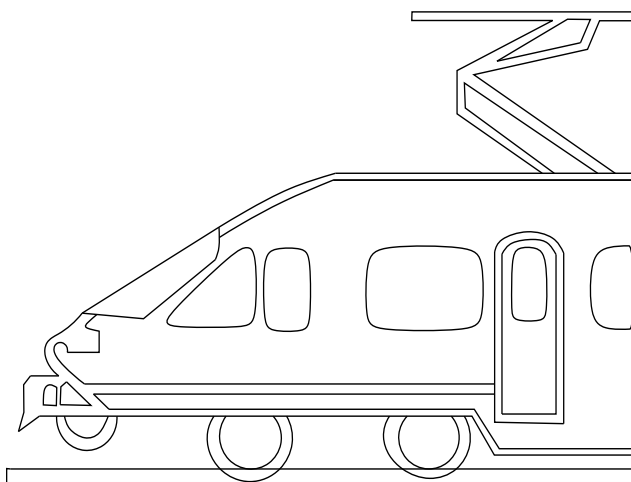
Figure 4.1.4: Different applications of air springs in buses and trucks, machines, and, rail-bound vehicles.
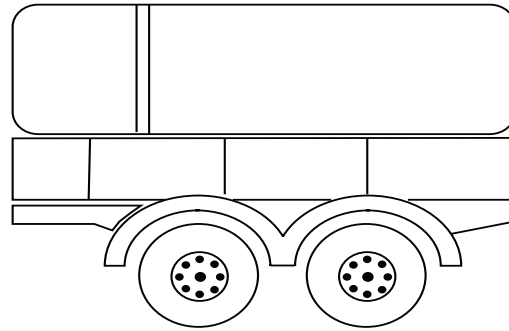
Trailers
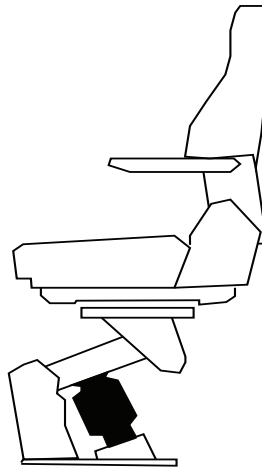
Driver's seats
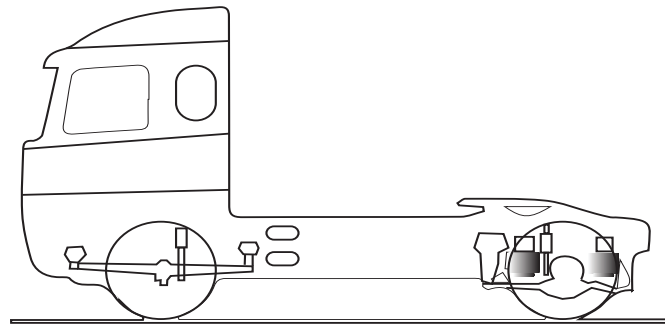
Cabs

Figure 4.1.5: Different applications of air springs in trailers, driver's seats, and cabs.

4.2   Design elements in air spring bellows

The damping effect of the air spring is primarily determined by the design of its bellows. Therefore, the materials used in its design should be durable.

The general construction of air spring bellows consists of the following structures:

- An outer and inner surface layer
- Reinforcement materials
- Bead rings made of steel cords.

4.2.1 Outer and inner layer material

Elastomers like rubber are used in the inner and outer layer of the bellow. The inner layer of the bellow is supposed to provide a very high degree of air proofing. This can be achieved by using a thick inner elastomer layer or using an elastomer material that provides better air proofing. Similarly, the outer layer requires resilience so as to resist weathering, temperature changes and contact with dust and oil in the air spring's normal range of use.

Two types of elastomer blends are used in the industry: Chloroprene and Natural rubber.

4.2.2 Reinforcement materials

Reinforcement materials help the bellows of the air springs absorb and damp the loading forces transmitted through the air in the bellow. The reinforcement fabric consists of cords placed parallel to each other. Also, the reinforcement fabric can only resist loading in the direction of the fibers. This is the reason that two fabric layers are criss-crossed over each other at a specific cord angle dictated by the unique design of the air spring.

Moreover, for rail vehicles, owing to demanding operating conditions, high burst resistance is desirable. For these air springs, reinforcement is typically achieved with the combination of a specific cord angle and number of cords in a layer measured in ends per inch.

Common materials used for the reinforcement fibers are: Polyamide PA 6.6, Polyester, aramid, steel cord, Fiber glass and carbon fiber. Amongst these, Polyamide and polyester are the most commonly used because of their strength characteristics. Fiber glass and carbon fiber have superior strength in the longitudinal direction, which could make them an attractive option for use as reinforcement cords. However, they break easily when bent which makes them less reliable choices for use in air springs.

4.2.3 Bead rings made of steel cords

In the context of air springs and tires, the term "bead" refers to a reinforced and rigid portion of the structure that helps the air spring maintain its shape and securely attach to the suspension system. The bead is typically made of steel wires or cords that are coated with rubber and woven or wrapped to form a strong, circular structure. The steel wires are generally vulcanized into the rubber material.

The name "bead" is derived from the fact that this reinforced portion of the air spring forms a kind of "bead" or circle. The bead is crucial for maintaining the integrity of the air spring, especially when the bellow is inflated when the air spring is in operation. It provides a stable foundation and ensures a secure fit on the rim or other components like pistons and plates in

the suspension system where it needs to provide damping. The use of beads with steel cords enhances the structural integrity and performance of the air spring.

Other than bead rings, the ends of the bellows can also be crimped to provide the same functionality as bead rings.

4.3 Manufacturing process of Air springs

There are 8 major steps in the manufacturing of air springs. Their short summary will be described in the next section.

- Blending the elastomer
- Fabric treatment
- Making the Cores
- Rubberising the fabric or Calendering
- Cutting fabric and rubber layers
- Layering or Building
- Curing or Vulcanization
- Assembly

4.3.0.1 Blending the elastomer

The elastomer is typically formed before the manufacturing of the air springs begin. The natural or synthetic rubber is blended with additives to achieve desired physical characteristics. These additives include plasticizers, accelerators, ozone inhibitors, light-colored fillers, and oil. This blend of rubber and additives is formed into large sheets rolled up in calendars for use in air spring's bellow manufacturing.

4.3.0.2 Fabric treatment

The fabric layer is made similar to how fabric is made for the textile industry. Initially, numerous thin filaments are spun to form a yarn. Two or three of these yarns are then brought together to form a twine or a braid. The weaving mill turns this twin or braid into a fabric. The fabric is then stretched and dipped into a solution called Retex (Resin and Latex). A coating of this solution helps the fabric bond well with the elastomer later in the manufacturing process.

4.3.0.3 Making the Cores

While the bellow is situated on the winding cylinder, the subsequent stage in the manufacturing process involves placing the inner and outer steel wire cores at the ends of the lay out. The remaining rubber section is folded over the steel core and compressed onto itself, creating a flap that secures the core in place.

The steel cores themselves are formed in different ways. Cores can be welded together to form a single cord, or cores can be welded together to form a cable. These cables can be wound multiple times to form a cable core.

4.3.0.4 Rubberising the fabric or Calendering

The Non-rubberised Retex treated fabric roll produced in the last step is then coated on both sides with elastomer, rubber in the case of air springs, with a process named calendaring. The 4-roll calendar can coat both sides of the fabric in one go, whereas a 3-roll calendar does this in 2 steps.

4.3.0.5 Cutting fabric and rubber layers

The rubber sheets from the first step are cut into rectangular sections according to the length of the bellow they are designed for. The rubberised fabric is also cut but the angle at which it is cut defines an important parameter called the cord angle. The cord angle is the angle between the cord and the longitudinal direction of the sheet roll. The α_0 is shown in Figure 4.3.1.
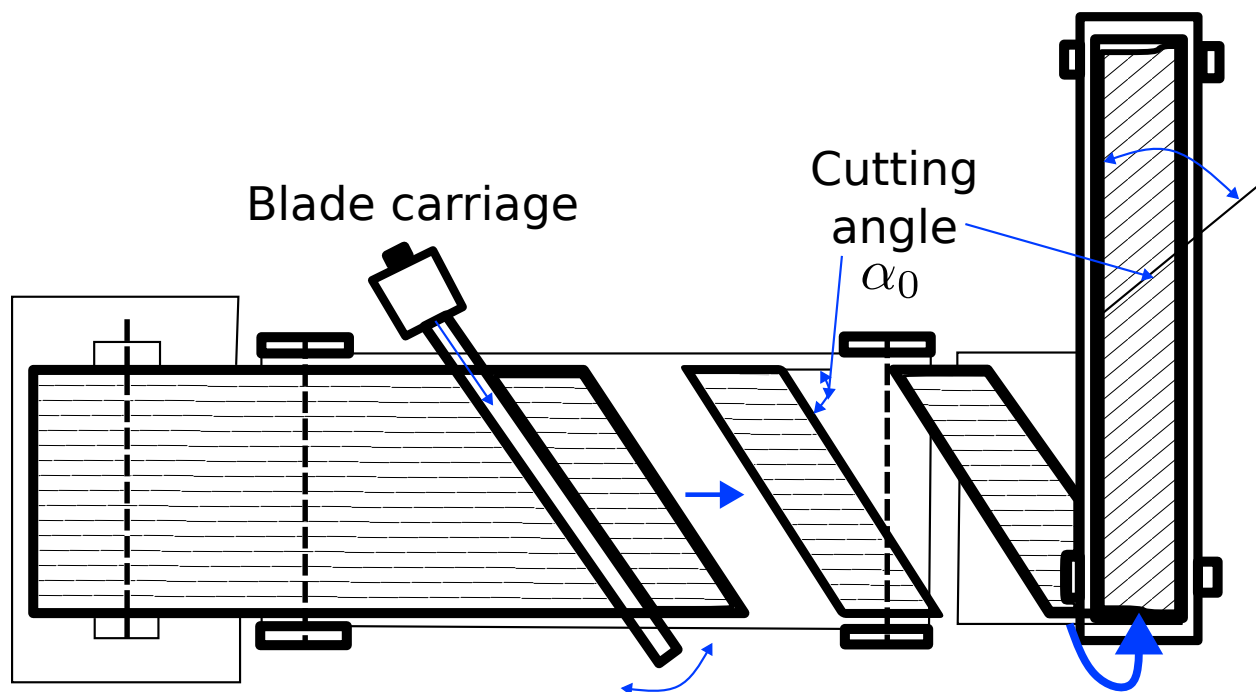
Figure 4.3.1: Cutting the fabric.

4.3.0.6 Layering or Building

After the cutting of fabric and rubber sheets in desired sizes, the bellow is built. The constituents of bellows are layered one by one on a custom metallic drum or a winding cylinder made according to the designed size of bellow. First, a layer of cut rubber sheet is rolled on the drum. Then two layers of fabric cut at an angle are laid on top of eachother in a criss-cross manner and rolled onto

the drum. Then the outer layer made of cut rubber sheet is rolled on top of the fabric layers, as shown in Figure 4.3.2.
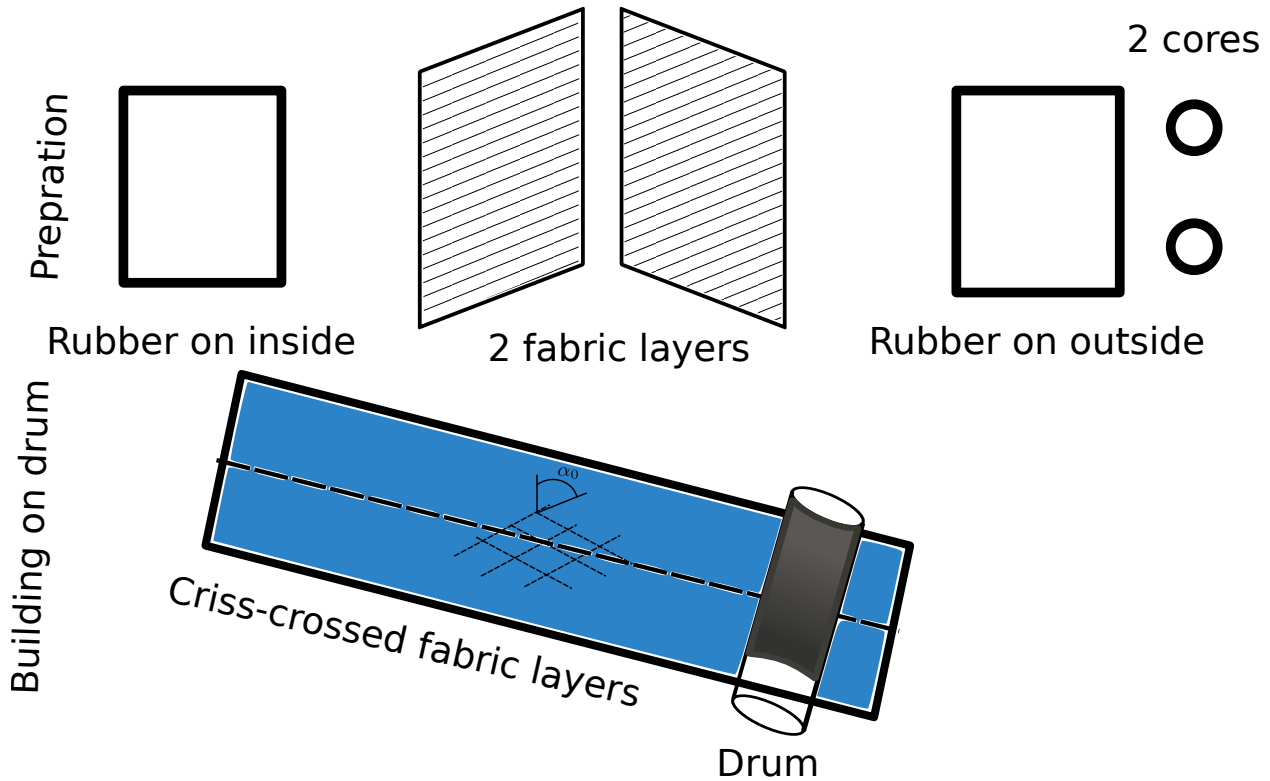
Figure 4.3.2: Finishing of the uncured product.

This roll of layers of rubber and fabric is then passed through pressure rollers that make sure that there is no air trapped between the layers and that the layers form a cohesive structure in the next step.

4.3.0.7   Curing or Vulcanization

The layered product formed in the last step is uncured. It is vulcanized in a mould for a period of time between 6 and 12 minutes and at a temperature between 160 degrees to 190 degrees depending on the specific blend of elastomer.

Pressure is applied in the internal cavity so that the product conforms to the contour of the mould without any creases. This step causes the diameter of the product to increase while at the same time causing the length to decrease. The angle of the cords in the fabric layers also changes from the winding angle in the layering step to a smaller value called the vulcanization angle. This step gives out a cured, rubber and fabric layered product that forms the bellow. This step is shown in the Figure 4.3.3.
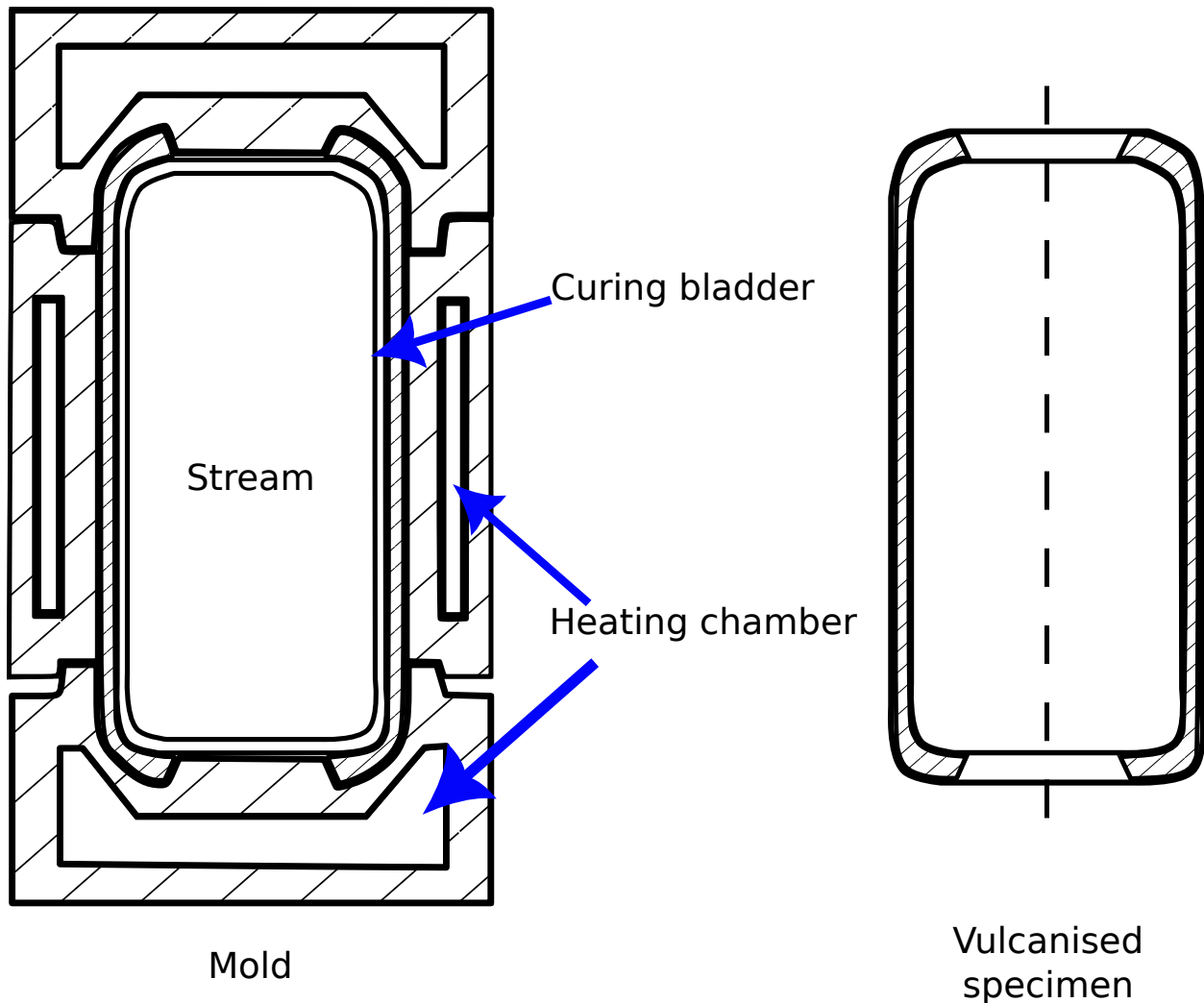
Figure 4.3.3: Vulcanisation process

4.3.0.8 Assembly

After the layers of elastomer and reinforced fabric are vulcanized in the shape of the bellow, they are fitted with metallic bead rings on both ends to form the desired bellow shape. They are then fitted with pistons and end plates to produce the final product.

Based on their fittings, there are three main types of air springs : crimped air springs, dismountable air springs, bead ring air springs and a rolling lobe air spring. Crimped air springs have bead plates permanently mounted or crimped to the top and bottom ends of the bellow with a mounting press. These air springs are not supposed to be disassembled or dismounted.

In the case of clampable or dismountable air springs, the end plates made of steel or aluminum are fitted to the bellow in a forming press. These end plates are clampable because of the fastener and threaded holes for mounting where required and hence these connected parts can be dismounted when required.

For the bead ring air springs, connecting parts are manufactured with studded or socket head bead rings without fitted end plates. They are supposed to be fitted directly on the machine surface with no additional seals. These air springs can be dismounted. Lastly, the rolling lobe air springs are the ones in which the bellows are crimped on one side and attached with a piston to the other side.

4.4   Modeling of bellow

The bellow can be effectively modeled as a composite material, given its composition of rubber layers and fiber layers. Notably, the bellow exhibits distinct material properties in the direction of the fibers, a characteristic response of reinforced materials.

One approach is to directly model it at the global scale, although this requires substantial computational power. Alternatively, homogenizing the fabric layer, which comprises both fiber and rubber materials, offers a more feasible solution. The subsequent discussion delves into the homogenization of the fabric layer.

The plugin developed in Section 3.4.2 was specifically designed for linear perturbation analysis. However, due to the use of rubber in air springs, employing linear analysis could yield inaccurate results given the hyperelastic response of rubber. Moreover, the model should be capable of handling both material and geometrical nonlinearity inherent in air springs. To address nonlinearity, modifying the plugin becomes essential.

Initially, the analysis type must shift from linear perturbation to general static analysis. Homogenization then needs to occur at each iteration when equilibrium is achieved. This involves collecting stress and strain data from the body, applying averages of these fields throughout the body, and storing this information in a list.

Additionally, as the information on stress and strain exceeds two points, and a static general analysis step is utilized, the conventional load cases of ABAQUScannot be applied. Instead, six different models corresponding to six loading cases need to be created. Each model will generate a comprehensive list of stress and strain data.

Adjustments to the post-processing of the plugin are necessary, considering the availability of information beyond two points. Options include using regression analysis to determine unknowns of the linear model or employing various homogenization scenarios involving the engineering of the strain energy function. To find the unknowns of these models, optimization algorithms are required. The schematic representation of this idea is presented in Figure 4.4.1.

For engineering the material model and determining its parameters, external software such as MATLAB or Python must be utilized. These programs fetch homogenization data, create the strain energy potential, and identify the unknowns or missing parameters of the engineered model.

To implement this custom model, UMAT in ABAQUS, which supports any custom model, must be employed. The entire pipeline needs to be meticulously crafted and implemented to achieve effective homogenization.
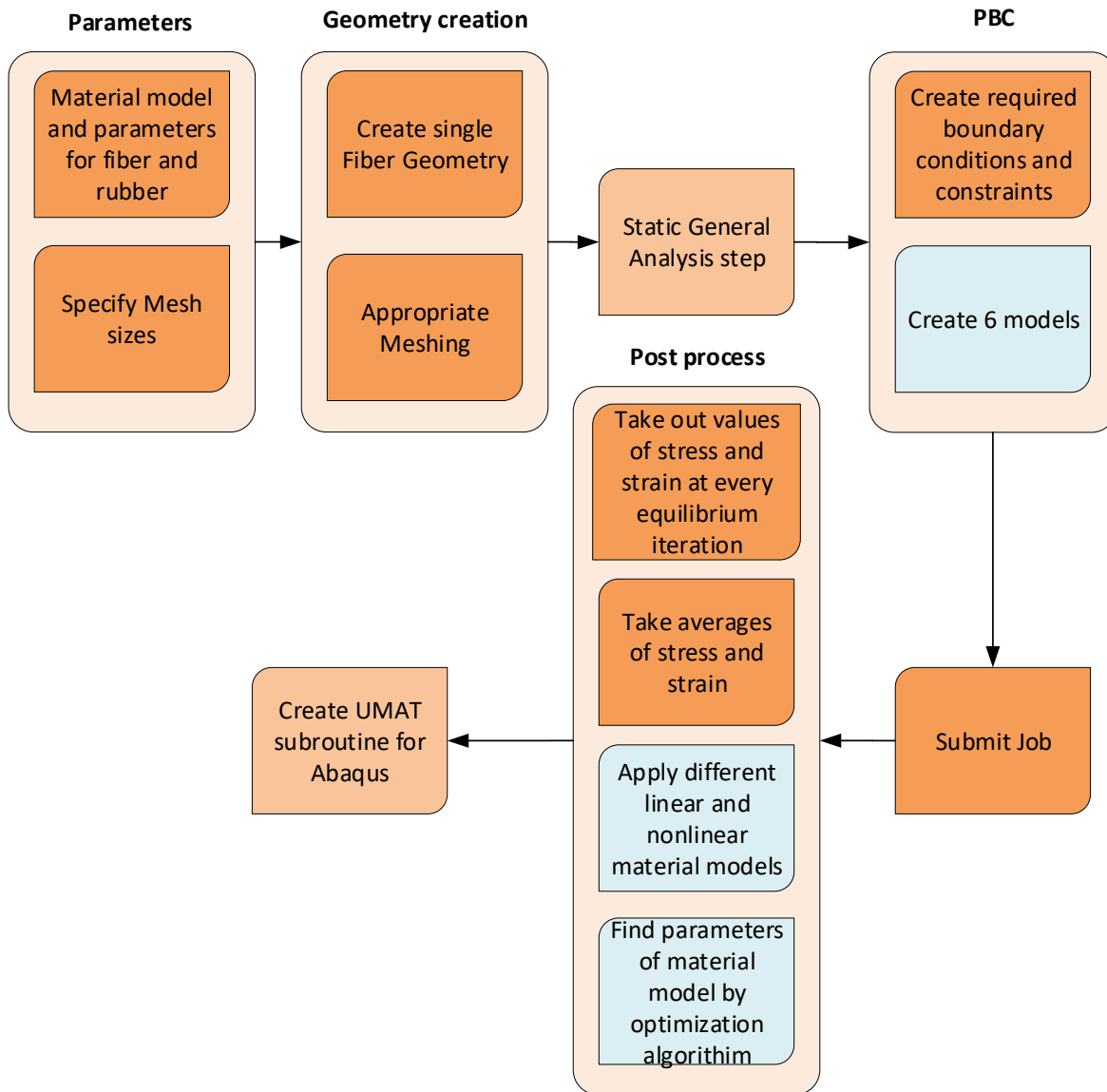
Figure 4.4.1: Modification in plugin

4.4.1 Material model for Rubber

The Mooney–Rivlin model is commonly employed for capturing the hyperelastic response of rubber. This model utilizes the first order of the first and second invariants and can be expressed as:

$$\Psi = C_{10} \left(\bar{I}_1 - 3 \right) + C_{01} \left(\bar{I}_2 - 3 \right) + \frac{1}{D_1} \left(J - 1 \right)^2 ,$$

where C_{10} and C_{01} are material constants influencing the isochoric part of the Helmholtz free energy function. The convention in Abaqus employs C_{i0} as the multiplier with the term $\left(\bar{I}_1 - 3\right)^i$, and similarly, C_{0i} is the multiplier with the term $\left(\bar{I}_2 - 3\right)^i$.

Similarly, the constants D_i can be associated with the term $(J - 1)^{2i}$. Notably, the term $\frac{1}{D_1}$ contributes solely to the volumetric part. For incompressible materials $(J = 1)$, only the deviatoric contribution from Ψ remains. These constants have physical interpretations and can be related to the bulk modulus (κ_0) and shear modulus (μ_0) as follows:

$$\mu_0 = 2\left(C_{10} + C_{01}\right), \quad \kappa_0 = \frac{2}{D_1}.$$

The determination of these model constants is typically achieved through experimental evaluation. Values from material databases [11] for the Mooney-Rivlin model applied to rubber are presented in Table 4.4.1.

C_{10}	C_{01}	D_1
0.42981	0.10745	0.005

Table 4.4.1: Mooney-Rivlin model for rubber

4.4.2   Material model for chord

The Marlow model, as proposed by Marlow [26], serves as a valuable tool for modeling the behavior of a chord. This model operates under the assumption that the Helmholtz free energy function depends solely on the first invariant. This approach, emphasizing the significance of the first invariant, is also shared by other models such as the Neo-Hookean model, Yeoh model [47], and various chain-stretch models [3]. The energy functional for the Marlow model takes the form:

$$\Psi = \Psi_{\text{iso}}(\bar{I}_1) + \Psi_{\text{vol}}(J),$$

where Ψ_{iso} represents the isochoric part of the Helmholtz free energy function, and Ψ_{vol} denotes the volumetric part.

The fundamental concept behind this model is derived from the definition of the first invariant. For an incompressible material, considering two independent stretches λ_1 and λ_2, the first invariant I_1 is expressed as:

$$I_1(\lambda_1, \lambda_2) = \lambda_1^2 + \lambda_2^2 + \frac{1}{\lambda_1^2 \lambda_2^2}.$$

The term $\frac{1}{\lambda_1^2 \lambda_2^2}$ arises due to the volume-preserving property of the incompressible material. For a uniaxial tension test, this simplifies to:

$$I_1(\lambda, \frac{1}{\sqrt{\lambda}}) = \lambda^2 + \frac{1}{\lambda},$$

where λ represents the stretch in the axial direction. It is noteworthy that I_1 takes values in the range $[3, +\infty)$. From this equation, given any value of I_1, we can determine the corresponding λ. The uniaxial strain ε is related to λ as:

$$\varepsilon = \lambda - 1.$$

Assuming experimental data provides uniaxial stress σ and ε, the isochoric part Ψ_{iso} is computed as:

$$\Psi_{\text{iso}}(I_1) = \int_0^{1-\lambda(I_1)} \sigma(\varepsilon) \, d\varepsilon.$$

This equation allows for the direct computation of the isochoric part of the Helmholtz free energy function without the need for curve fitting. The uniaxial data for the chord is shown in Figure 4.4.2.

Tensile test of chord
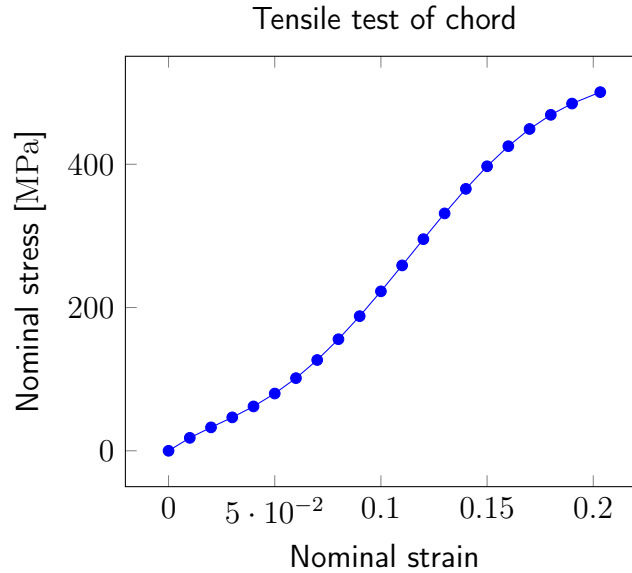
Figure 4.4.2: Uni-axial test of chord material

4.5 Single chord model

The size of the Representative Volume Element (RVE) is chosen to be $\frac{1}{100}$th of the original bellow height, positioning it midway between the spacing of the two chords. This RVE accommodates a single fiber, considering the parallel orientation of fibers in cylindrical bellows, thus treating them as a periodic structure. Opting for a single-cord rubber matrix in this small RVE ensures that,

when given a local orientation, it replicates its configuration on all neighboring RVEs in a global model. The choice of a single cord matrix implies the consideration of the boundary of a fabric layer comprising a lone cord with a specific orientation.

It's important to note that this micromechanical model doesn't account for fiber orientation; the RVE is orthogonal to the fiber direction, with its x-axis aligned along the fiber direction. Fiber orientation is factored in at the meso scale by enabling the orientation option in ABAQUS, where the local orientation induces the same effect as the defined fibers.

The dimensional data of the RVE is adopted from a prior study [4], where the cross-sectional area of the fiber was $0.282\,743\,\mathrm{mm}^2$, and the spacing between the two chords was $0.738\,111\,7\,\mathrm{mm}$.

This RVE model is subjected to the same boundary conditions as explained in the previous chapter. The simulation results are illustrated in figures (4.5.1, 4.5.2, and 4.5.3).

In the upcoming section, the stress and strain results will be exported to MATLAB. Subsequently, an attempt will be made to approximate the bellow of the air spring using both strain-based and invariant-based approaches.

4.5.1 Linear Anisotropic model

Our initial approach involved employing the Saint-Venant Kirchhoff model, a strain-based model that assumes linear anisotropy. The Helmholtz free energy function for this model is expressed as:

$$\Psi\left(\varepsilon^G\right) = \frac{1}{2}\varepsilon^G : \mathbf{C} : \varepsilon^G,$$

where $\mathbf{C}$ represents the fourth-order elasticity tensor, and ε^G denotes the Green's strain in the reference configuration as defined in 2.1.9. The derivatives concerning Green strain are provided by:

$$\frac{\partial \Psi}{\partial \varepsilon^G} = \mathbf{C} : \varepsilon^G,$$
$$\frac{\partial^2 \Psi}{\partial \varepsilon^G \partial \varepsilon^G} = \mathbf{C}.$$

By leveraging the argument of major symmetry and minor symmetry, we effectively reduce the number of unknowns associated with $\mathbf{C}$ to 21, as opposed to the original 81. Subsequently, the homogenized data needs to be loaded into Matlab for the application of linear regression. This regression process yields six functions: σ_{11}, σ_{22}, σ_{33}, σ_{12}, σ_{13}, and σ_{23}, each expressed as functions of the six Green strains ε_{11}, ε_{22}, ε_{33}, ε_{12}, ε_{13}, and ε_{23}.

The linear regression for σ_{11} takes the form (without bias term):

$$\sigma_{11}\left(\varepsilon_{11}, \varepsilon_{22}, \varepsilon_{33}, \varepsilon_{12}, \varepsilon_{13}, \varepsilon_{23}\right) = C_{1111}\varepsilon_{11} + C_{1122}\varepsilon_{22} + C_{1133}\varepsilon_{33} + C_{1112}\varepsilon_{12} + C_{1113}\varepsilon_{13} + C_{1123}\varepsilon_{23}.$$

(a) Von Mises stress of single chord model for normal strain in 1 direction.

S, Mises
(Avg: 75%)

+2.355e+03
+2.159e+03
+1.963e+03
+1.767e+03
+1.571e+03
+1.374e+03
+1.178e+03
+9.823e+02
+7.862e+02
+5.901e+02
+3.940e+02
+1.979e+02
+1.830e+00

(b) Von Mises stress of single chord model for normal strain in 1 direction.

S, Mises
(Avg: 75%)

+4.541e+02
+4.163e+02
+3.785e+02
+3.407e+02
+3.029e+02
+2.651e+02
+2.273e+02
+1.895e+02
+1.517e+02
+1.139e+02
+7.612e+01
+3.832e+01
+5.209e−01
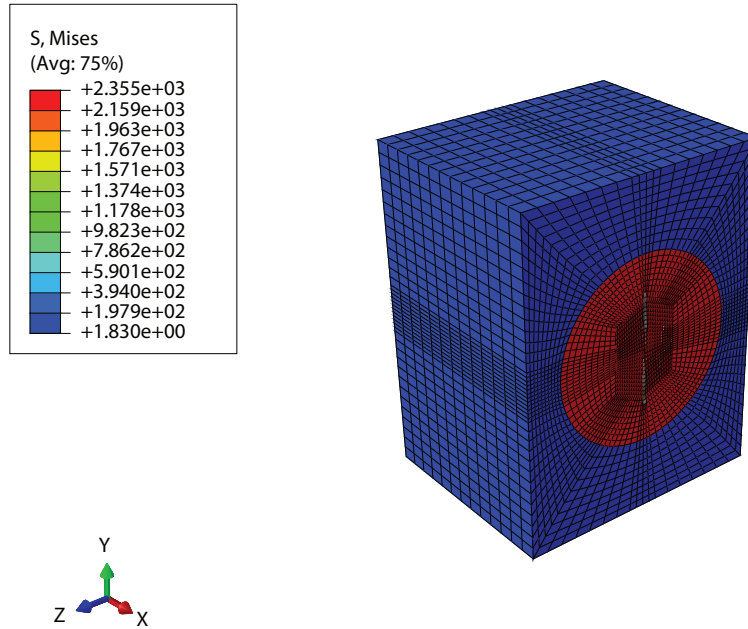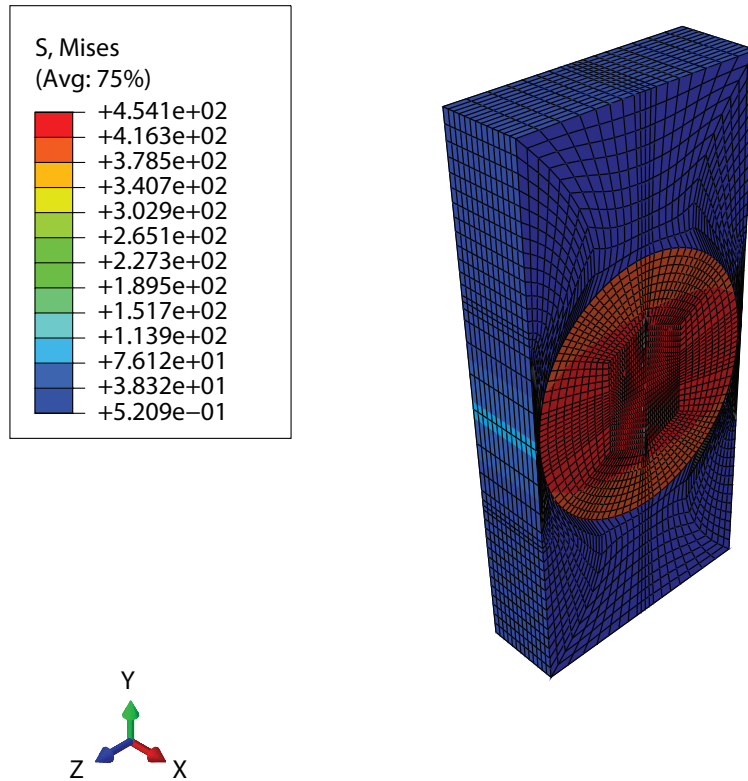
Figure 4.5.1: Von Mises stress of single chord model for normal strains in 1 and 2 direction.

(a) Von Mises stress of single chord model for normal strain in 3 direction.
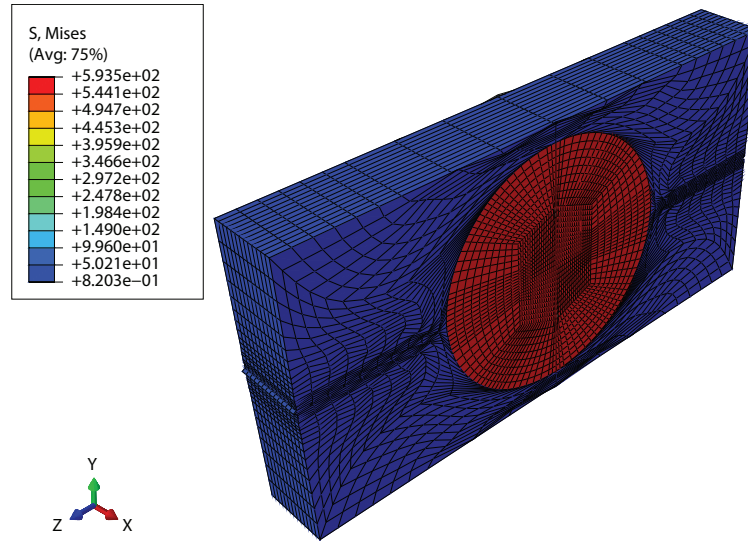
(b) Von Mises stress of single chord model for shear strain in 12 direction.
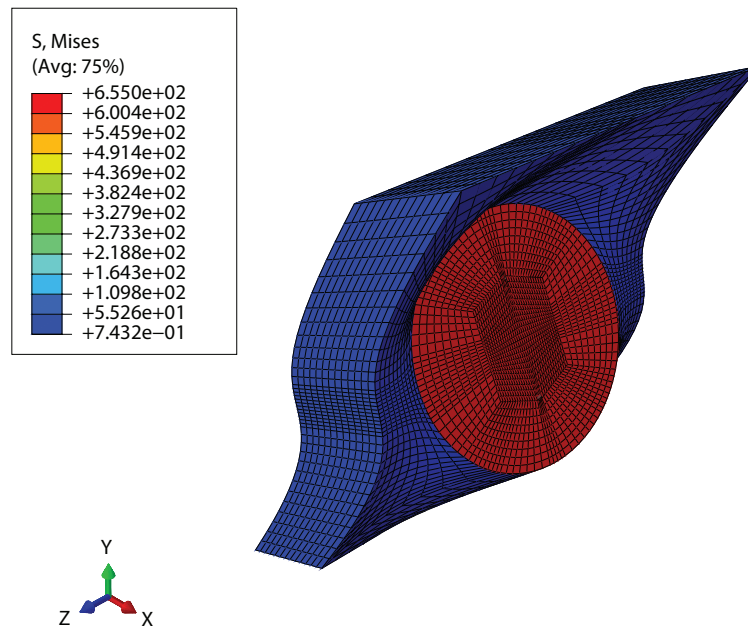
Figure 4.5.2: Von Mises stress of single chord model for normal strains in 1 and shear strain in 12 direction.

Thus, through the application of linear regression, we can determine these constants accurately. This process is explained in Figure 4.5.4.

(a) Von Mises stress of single chord model for shear strain in 13 direction.
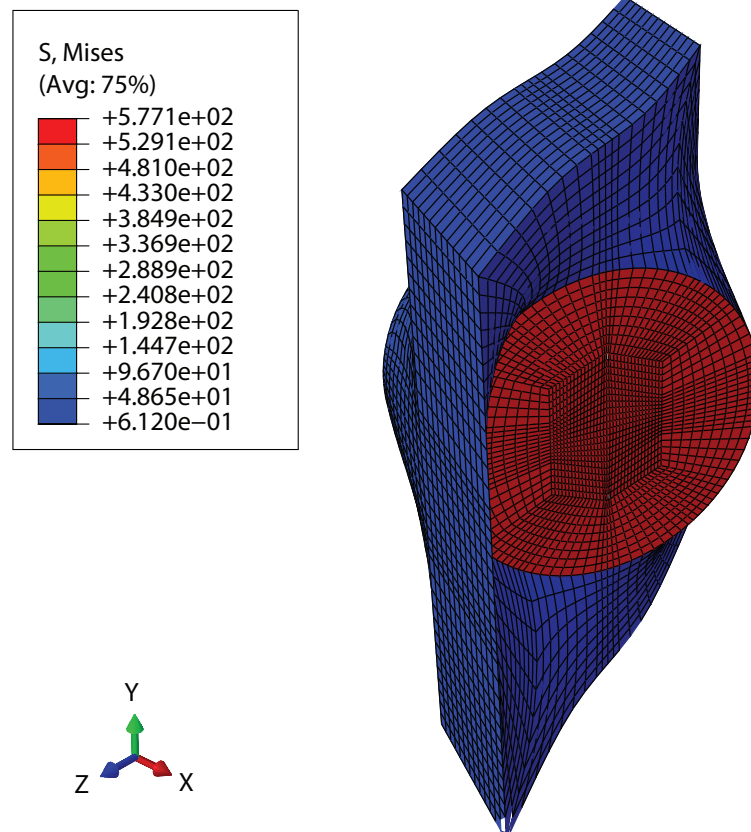
(b) Von Mises stress of single chord model for shear strain in 23 direction.
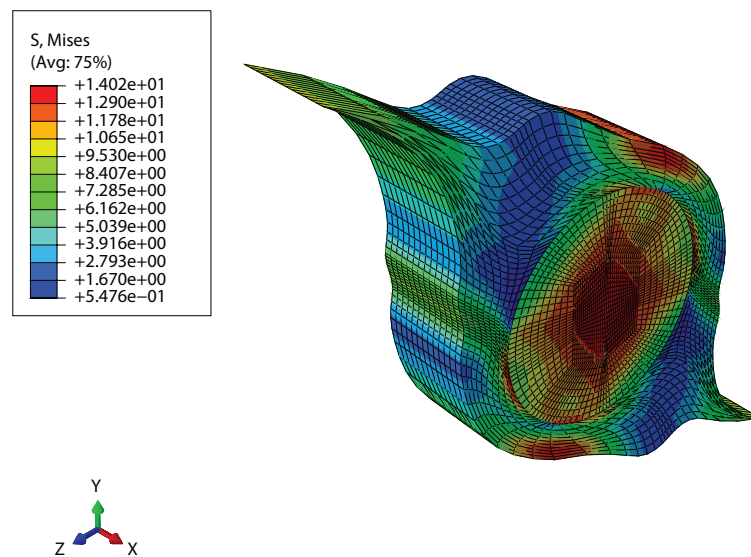
Figure 4.5.3: Von Mises stress of single chord model for shear strains in 13 and 23 direction.
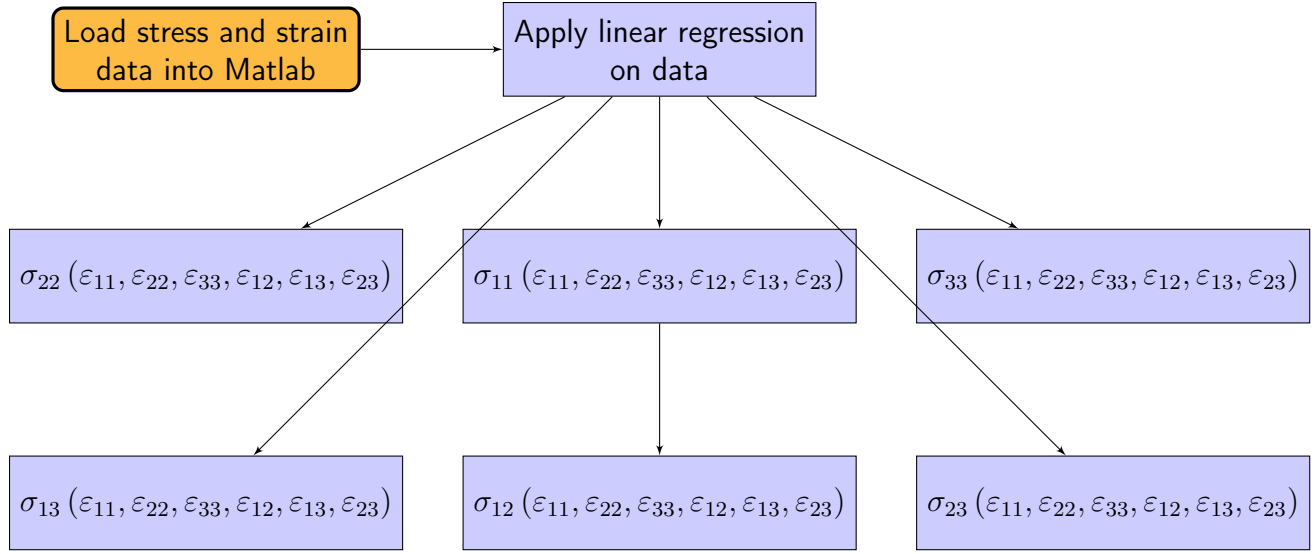
Figure 4.5.4: Pipeline to apply linear regression

The result is shown in Figure 4.5.5.

The C is determined to be:

$$
C = \begin{bmatrix}
560.0 & 19.0 & 21.0 & 0 & 0 & 0 \\
19.0 & 64.0 & 43.0 & 0 & 0 & 0 \\
21.0 & 43.0 & 64.0 & 0 & 0 & 0 \\
0 & 0 & 0 & 56.0 & 4.9 \times 10^{-5} & 4.9 \times 10^{-5} \\
0 & 0 & 0 & 4.9 \times 10^{-5} & 49.0 & 1.1 \times 10^{-7} \\
0 & 0 & 0 & 4.9 \times 10^{-5} & 1.1 \times 10^{-7} & 2.7
\end{bmatrix} \text{MPa}
$$

The figure shows the linear model performs poorly at the region of nonlinearity. Moreover, the regions of nonlinearity are dominant for the shear response. To implement in the ABAQUS subroutine, we have to add some more modifications which are discussed in the next section.

4.5.1.1   Implementation in ABAQUS

The incorporation of material models in simulations can be achieved through the utilization of the user subroutine *UMAT*. Within this subroutine, it is necessary to establish the relationship between stress and strain, along with defining the elasticity tensor. Another viable option offered by ABAQUS is the *UANISOHYPER_STRAIN* subroutine. In this context, the Helmholtz free energy function and its derivatives concerning the modified Green's strain ($\bar{\varepsilon}^G$) are crucial, as outlined below:
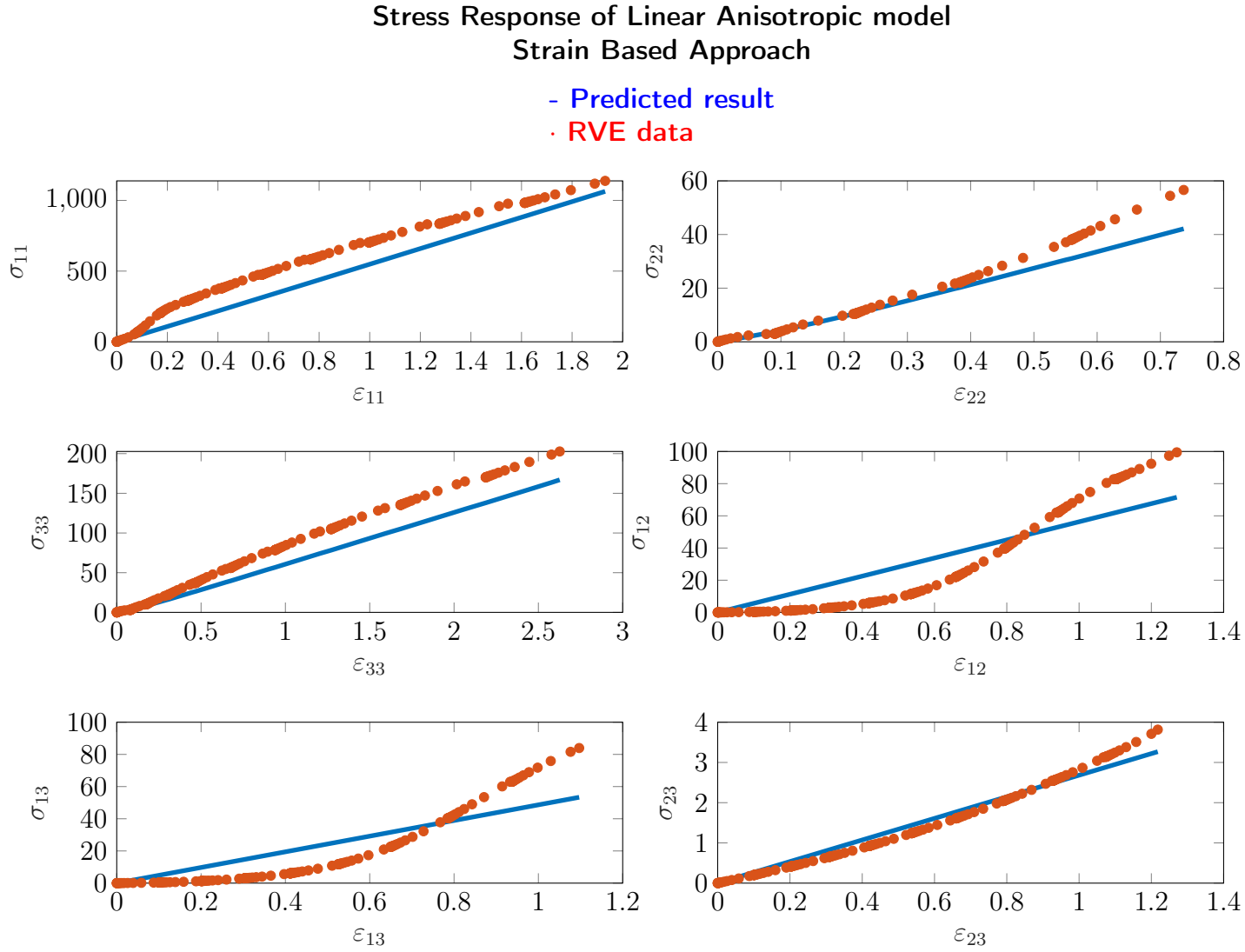
Figure 4.5.5: Results by a strain-based linear anisotropic model. RVE data is plotted with red color, and the model prediction is plotted with blue color.

$$\bar{\varepsilon}^G = \frac{1}{2}\left(J^{-\frac{2}{3}}C - I\right),$$

$$\bar{\varepsilon}^G = \frac{1}{2}\left(J^{-\frac{2}{3}}\left(2\varepsilon^G + I\right) - I\right),$$

$$J^{\frac{2}{3}}\left(\bar{\varepsilon}^G + \frac{1}{2}I\right) = \frac{1}{2}\left(2\varepsilon^G + I\right),$$

$$\varepsilon^G = J^{\frac{2}{3}}\bar{\varepsilon}^G + \frac{1}{2}\left(J^{\frac{2}{3}} - 1\right)I,$$

$$\frac{\partial \varepsilon^G}{\partial \bar{\varepsilon}^G} = J^{\frac{2}{3}}\frac{\partial \varepsilon^G}{\partial \varepsilon^G},$$

By applying the chain rule, the remaining derivatives can be determined:

$$
\begin{aligned}
\frac{\partial \Psi}{\partial \bar{\varepsilon}^G} &= J^{\frac{2}{3}} \frac{\partial \Psi}{\partial \varepsilon^G}, \\
\frac{\partial \Psi}{\partial J} &= \frac{\partial \varepsilon^G}{\partial J} : \frac{\partial \Psi}{\partial \varepsilon^G}, \\
\frac{\partial^2 \Psi}{\partial \bar{\varepsilon}^G \partial \bar{\varepsilon}^G} &= J^{\frac{4}{3}} \frac{\partial^2 \Psi}{\partial \varepsilon^G \partial \varepsilon^G}, \\
\frac{\partial^2 \Psi}{\partial J \partial J} &= \frac{\partial^2 \varepsilon^G}{\partial J^2} : \frac{\partial \Psi}{\partial \varepsilon^G} + \frac{\partial \varepsilon^G}{\partial J} : \frac{\partial^2 \Psi}{\partial \varepsilon^G \partial \varepsilon^G} : \frac{\partial \varepsilon^G}{\partial J}, \\
\frac{\partial^2 \Psi}{\partial J \partial \bar{\varepsilon}^G} &= \frac{2}{3} J^{-\frac{1}{3}} \frac{\partial \Psi}{\partial \varepsilon^G} + J^{\frac{2}{3}} \frac{\partial^2 \Psi}{\partial \varepsilon^G \partial \varepsilon^G} : \frac{\partial \varepsilon^G}{\partial J},
\end{aligned}
$$

where

$$
\frac{\partial \varepsilon^G}{\partial J} = \frac{2}{3J} \left(\varepsilon^G + \frac{1}{2} I \right)
$$

and

$$
\frac{\partial^2 \varepsilon^G}{\partial J^2} = -\frac{1}{3J} \frac{\partial \varepsilon^G}{\partial J}.
$$

The implementation details can be found at https://github.com/Jamal-dev/thesis_material/.

4.5.2 Strain-based nonlinear anisotropic model

Based on the results from the previous section. We modified the energy potential by adding one nonlinear term:

$$
\Psi \left(\varepsilon^G \right) = \frac{1}{2} \varepsilon^G : \mathbf{C} : \varepsilon^G + \frac{1}{4} \varepsilon^{G2} : \mathbf{D} : \varepsilon^{G2},
$$

where both $\mathbf{C}$, $\mathbf{D}$ are fourth-order material tensors. The derivatives with respect to ε^G becomes:

$$
\begin{aligned}
\frac{\partial \Psi}{\partial \varepsilon^G} &= \mathbf{C} : \varepsilon^G + \frac{1}{2} \varepsilon^G \cdot \mathbf{D} : \varepsilon^{G2} + \frac{1}{2} \varepsilon^{G2} : \mathbf{D} \cdot \varepsilon^G, \\
\frac{\partial^2 \Psi}{\partial \varepsilon^G \partial \varepsilon^G} &= \mathbf{C} + \frac{1}{2} \mathbb{I} \cdot \mathbf{D} : \varepsilon^{G2} + \varepsilon^G \cdot \mathbf{D} \cdot \varepsilon^G + \varepsilon^G \cdot \mathbf{D} \cdot \varepsilon^G + \frac{1}{2} \varepsilon^{G2} : \mathbf{D} \cdot \mathbb{I},
\end{aligned}
$$

where $\mathbb{I}$ is the fourth order symmetric tensor defined as $\mathbb{I}_{ijkl} := \frac{\delta_{ik}\delta_{jl} + \delta_{jk}\delta_{il}}{2}$. The results for this model can be seen in Figure 4.5.6. The matrices C, and D are found to be:

Deviatoric Stress Response of nonlinear Anisotropic model
Strain Based Approach

- Predicted result
· RVE data
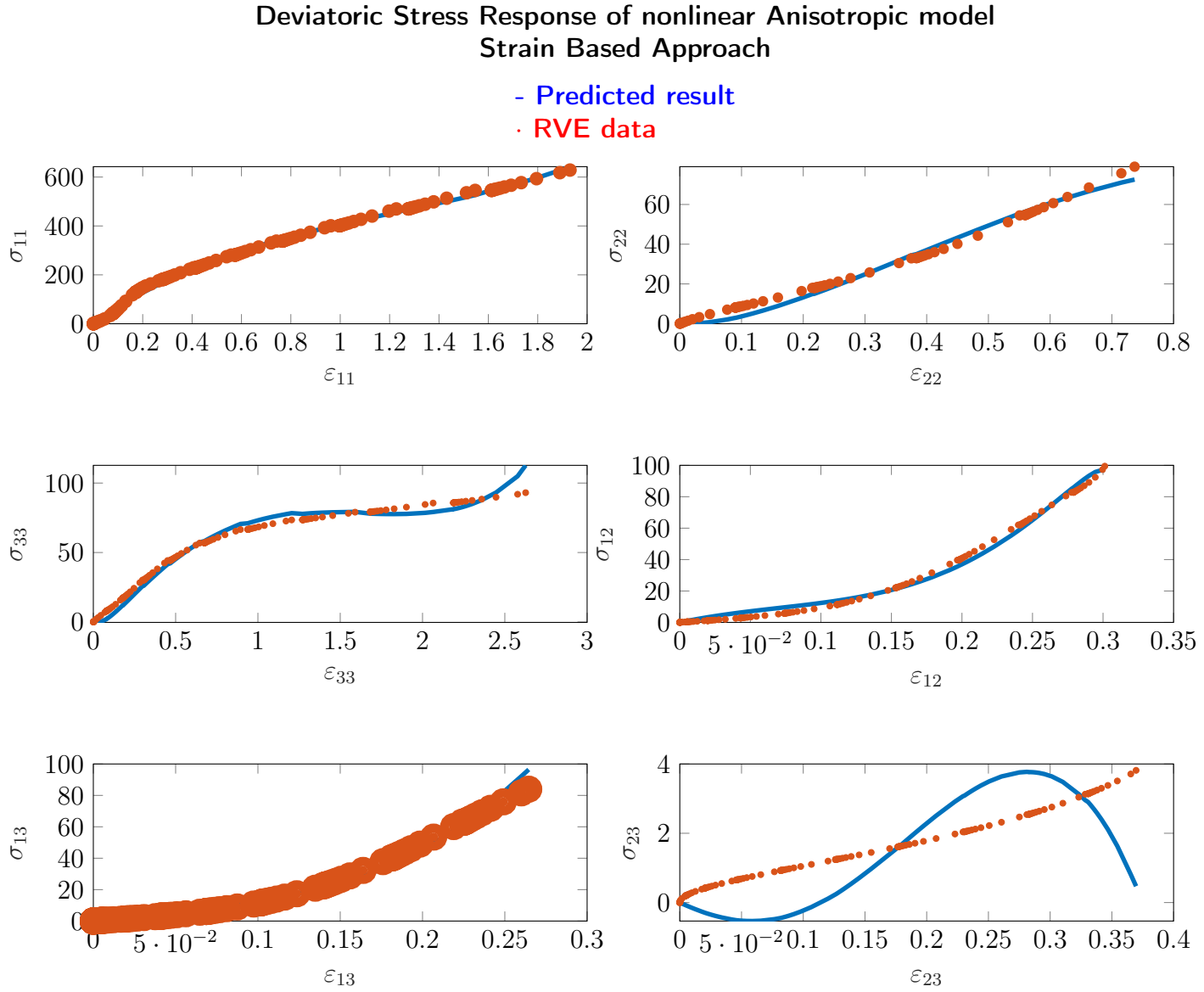
Figure 4.5.6: Deviatoric stress results of non-linear strain-based model. RVE data is plotted with red color, and the model prediction is plotted with blue color.

$$
\boldsymbol{C} = \begin{bmatrix}
-158.0 & -609.0 & -608.0 & 0 & 0 & 0 \\
-609.0 & -30.4 & 252.0 & 0 & 0 & 0 \\
+608.0 & 252.0 & -71.4 & 0 & 0 & 0 \\
0 & 0 & 0 & 93.1 & 0 & 0 \\
0 & 0 & 0 & 0 & 110.0 & 0 \\
0 & 0 & 0 & 0 & 0 & -8.19
\end{bmatrix},
$$

$$
\boldsymbol{D} = \begin{bmatrix}
14.0 & 0 & 0 & 0 & 0 & 0 \\
0 & -22.0 & 0 & 0 & 0 & 0 \\
0 & 0 & 3.38 & 0 & 0 & 0 \\
0 & 0 & 0 & 2660.0 & 0 & 0 \\
0 & 0 & 0 & 0 & 2960.0 & 0 \\
0 & 0 & 0 & 0 & 0 & -437.0
\end{bmatrix}.
$$

The results show the good agreement with the RVE data. However, when analyzed the results in ABAQUS, it shows the stability problem. The reason lies in the involvement of strain in the elasticity tensor. The elasticity tensor's condition number becomes high at certain values of strain which leads to the inversion problem. In addition to this, the eigen values of stiffness matrix are negative which also causes stability problems. To tackle this problem, invariant-based approach is next used.

4.5.3 Invariant-based nonlinear anisotropic model

The conventional optimization algorithms in Matlab, such as *fmincon* and *fminsearch* [30], proved ineffective for parameter identification. To address this, a customized variation of the ADAM algorithm [22] was devised, detailed in Algorithm 1.

The algorithm begins with the user specifying the number of terms n for the Helmholtz free energy function Ψ. Subsequently, a set of n_i terms is selected, each associated with specific invariants. This model selection step requires user input. The Helmholtz free energy function is then expressed as a summation of these terms, featuring unknown parameters $P1_i, P2_j, P3_m, P4_k, P5_l$ multiplied by corresponding invariants. The algorithm's objective is to determine optimal values for these unknowns.

Key parameters, including the learning rate α, initialize the algorithm with vectors $\boldsymbol{\theta}_0$, m_0, v_0, and t_0. Here, $\boldsymbol{\theta}$ represents the parameter set, while m_0 and v_0 denote the 1st and 2nd moment vectors, respectively. The iteration step is denoted by t.

The algorithm incorporates hyperparameters such as β_1 and β_2 for exponential decay rates, with ϵ preventing division by zero. Weights $w_1, w_2, w_3, w_4, w_5, w_6$ are introduced to compute a weighted average of gradients during optimization.

Initialization involves loading nominal strain $\boldsymbol{\varepsilon}_N$ and Cauchy stress $\boldsymbol{\sigma}$ data, along with specifying the fiber direction in the reference configuration ($\boldsymbol{A}_1$), obtained from Abaqus.

For each nominal strain, relevant quantities related to the deformation gradient and invariants are computed. The iterative process continues until the parameter vector $\boldsymbol{\theta}_t$ converges. Within each iteration, gradients of stress components concerning parameters are calculated, and the Adam optimizer is employed for efficient parameter updates. Convergence is achieved when the parameter vector stabilizes, indicating optimal values for the material model parameters.

The algorithm introduces stochastic elements in two ways. The first option involves computing gradients for a batch of examples instead of all, enhancing computational speed. In the second option, random weights generated from a normal distribution are used, introducing randomness to each gradient and assigning varying importance randomly.

This algorithmic framework provides a systematic and iterative approach for refining and identifying material model parameters, facilitating the accurate representation of material behavior in computational simulations. To further explore this, multiple fitting methods were employed to analyze the data.

In the next section, the model and results will be presented.

Algorithm 1 An algorithm for the computation of material parameters

---

Require: Choose number of terms n for Ψ

Ensure: Choose n_i, where $i \in [1,5]$ terms such as $\sum_{i=1}^{5} n_i = n$

Require: Select $\Psi = \sum_{i,j,k,l,m=1}^{n_1,n_2,n_4,n_5,n_3} P1_i \left(\bar{I}_1 - 3 \right)^i + P2_j \left(\bar{I}_2 - 3 \right)^j + P4_k \left(\bar{I}_4 - 1 \right)^k + P5_l \left(\bar{I}_5 - 1 \right)^l + P3_m \left(J - 1 \right)^{2m}$

$P1_i, \ P2_j, \ P3_m, \ P4_k, \ P5_l$ are parameters which are multiplied with invariants

Require: α learning rate

Require: Initialize $\boldsymbol{\theta}_0, m_0, v_0, t_0, \ \boldsymbol{\theta} \in [P1_i, \ P2_j, \ P3_m, \ P4_k, \ P5_l]$; m_0, v_0 are 1st and 2nd moment vectors; t is iteration step; $\boldsymbol{\theta}$ is parameter vector

Require: $\beta_1 = 0.99, \ \beta_2 = 0.999, \ \epsilon = 1 \times 10^{-8}, \ \beta_i \in [0,1), i \in [1,2]$ are exponential decay rate; ϵ is to avoid division by 0

Require: Select weights $w_1, \ w_2, \ w_3, \ w_4, \ w_5, \ w_6$

Require: Load nominal strain $\boldsymbol{\varepsilon}_N$, and Cauchy stress $\boldsymbol{\sigma}$ data

Require: Fiber direction in reference configuration $\boldsymbol{A}_1$

    for Iterate over $\boldsymbol{\varepsilon}_N$ list **do**

        $\boldsymbol{v} \leftarrow \boldsymbol{\varepsilon}_N + \boldsymbol{I}$

        $\boldsymbol{b} \leftarrow \boldsymbol{v} \cdot \boldsymbol{v}$

        $J \leftarrow \det \boldsymbol{v}$

        $\bar{\boldsymbol{b}} \leftarrow J^{-\frac{2}{3}} \boldsymbol{b}$

        $\boldsymbol{F} \leftarrow \boldsymbol{v} \cdot \boldsymbol{R}$

        $\bar{\boldsymbol{F}} \leftarrow J^{-\frac{1}{3}} \boldsymbol{F}$

        $\bar{\boldsymbol{C}} \leftarrow \bar{\boldsymbol{F}}^T \cdot \bar{\boldsymbol{F}}$

        $\bar{I}_1 \leftarrow \mathrm{tr} \left(\bar{\boldsymbol{b}} \right)$

        $\bar{I}_2 \leftarrow \frac{1}{2} \left(\bar{I}_1^2 - \mathrm{tr} \left(\bar{\boldsymbol{b}} \cdot \bar{\boldsymbol{b}} \right) \right)$

        $\bar{I}_4 \leftarrow \bar{\boldsymbol{C}} : \boldsymbol{A}_1 \otimes \boldsymbol{A}_1$

        $\bar{I}_5 \leftarrow \bar{\boldsymbol{C}} \cdot \bar{\boldsymbol{C}} : \boldsymbol{A}_1 \otimes \boldsymbol{A}_1$

    end for

    while $\boldsymbol{\theta}_t$ not converge **do**

        $t \leftarrow t + 1$

        $\boldsymbol{g}1_t \leftarrow \nabla_{\boldsymbol{\theta}} \sigma_{11} \left(\boldsymbol{\theta}_{t-1}, \bar{\boldsymbol{b}}, J, \frac{\partial \Psi}{\partial \bar{I}_i} \left(\boldsymbol{\theta}_{t-1}, \bar{I}_i \right) \right), \forall i \in [1,5]$

        $\boldsymbol{g}2_t \leftarrow \nabla_{\boldsymbol{\theta}} \sigma_{22} \left(\boldsymbol{\theta}_{t-1}, \bar{\boldsymbol{b}}, J, \frac{\partial \Psi}{\partial \bar{I}_i} \left(\boldsymbol{\theta}_{t-1}, \bar{I}_i \right) \right), \forall i \in [1,5]$

        $\boldsymbol{g}3_t \leftarrow \nabla_{\boldsymbol{\theta}} \sigma_{33} \left(\boldsymbol{\theta}_{t-1}, \bar{\boldsymbol{b}}, J, \frac{\partial \Psi}{\partial \bar{I}_i} \left(\boldsymbol{\theta}_{t-1}, \bar{I}_i \right) \right), \forall i \in [1,5]$

        $\boldsymbol{g}4_t \leftarrow \nabla_{\boldsymbol{\theta}} \sigma_{12} \left(\boldsymbol{\theta}_{t-1}, \bar{\boldsymbol{b}}, J, \frac{\partial \Psi}{\partial \bar{I}_i} \left(\boldsymbol{\theta}_{t-1}, \bar{I}_i \right) \right), \forall i \in [1,5]$

        $\boldsymbol{g}5_t \leftarrow \nabla_{\boldsymbol{\theta}} \sigma_{13} \left(\boldsymbol{\theta}_{t-1}, \bar{\boldsymbol{b}}, J, \frac{\partial \Psi}{\partial \bar{I}_i} \left(\boldsymbol{\theta}_{t-1}, \bar{I}_i \right) \right), \forall i \in [1,5]$

        $\boldsymbol{g}6_t \leftarrow \nabla_{\boldsymbol{\theta}} \sigma_{23} \left(\boldsymbol{\theta}_{t-1}, \bar{\boldsymbol{b}}, J, \frac{\partial \Psi}{\partial \bar{I}_i} \left(\boldsymbol{\theta}_{t-1}, \bar{I}_i \right) \right), \forall i \in [1,5]$

        $\boldsymbol{g}_t = w_1 \boldsymbol{g}1_t + w_2 \boldsymbol{g}2_t + w_3 \boldsymbol{g}3_t + w_4 \boldsymbol{g}4_t + w_5 \boldsymbol{g}5_t + w_6 \boldsymbol{g}6_t$ ▷ Weighted average of 6 objectives

        $\boldsymbol{m}_t \leftarrow \beta_1 \boldsymbol{m}_{t-1} + (1 - \beta_1) \boldsymbol{g}_t$

        $\boldsymbol{v}_t \leftarrow \beta_2 \boldsymbol{v}_{t-1} + (1 - \beta_2) \boldsymbol{g}_t^2$ ▷ $\boldsymbol{g}_t^2$ is an element-wise multiplication

        $\hat{\boldsymbol{m}}_t \leftarrow \frac{\boldsymbol{m}_t}{1 - \beta_1^t}$ ▷ Correction term for first moment; β_1^t, t is exponent

        $\hat{\boldsymbol{v}}_t \leftarrow \frac{\boldsymbol{v}_t}{1 - \beta_2^t}$ ▷ Correction term for second moment; β_2^t, t is exponent

        $\boldsymbol{\theta}_t \leftarrow \boldsymbol{\theta}_{t-1} - \alpha \frac{\hat{\boldsymbol{m}}_t}{\sqrt{\hat{\boldsymbol{v}}_t + \epsilon}}$ ▷ Update step

    end while

4.5.3.1 Model 1

$$\Psi = c_1 \left(J - 1 \right)^2 + c_2 \left(\bar{I}_1 - 3 \right) + c_3 \left(\bar{I}_4 - 1 \right)$$

For the parameters $(c_1, c_2, c_3) = (4.2 \times 10^{-3}, 4.2, 4.7)$, the results are shown in Figure 4.5.7.

4.5.3.2 Model 2

$$\Psi = c_1 \left(J - 1 \right)^2 + c_2 \left(\bar{I}_1 - 3 \right) + c_3 \left(\bar{I}_4 - 1 \right) + c_4 \left(\bar{I}_4 - 1 \right)^2$$

For the parameters $(c_1, c_2, c_3, c_4) = (5.0 \times 10^{-3}, 2.5, 3.1, 2.9)$, the results are presented in Figure 4.5.8.

4.5.3.3 Model 3

$$\Psi = c_1 \left(J - 1 \right)^2 + c_2 \left(\bar{I}_1 - 3 \right) + c_3 \left(\bar{I}_1 - 3 \right)^2 + c_4 \left(\bar{I}_4 - 1 \right) + c_5 \left(\bar{I}_4 - 1 \right)^2$$

For the parameters $(c_1, c_2, c_3, c_4, c_5) = (4.6 \times 10^{-3}, 3.1, -52 \times 10^{-3}, 4.0, 4.3)$, the results are illustrated in Figure 4.5.9.

4.5.3.4 Model 4

$$\Psi = c_1 \left(J - 1 \right)^2 + c_2 \left(\bar{I}_1 - 3 \right) + c_3 \left(\bar{I}_4 - 1 \right) + c_4 \left(\bar{I}_5 - 1 \right)$$

For the parameters $(c_1, c_2, c_3, c_4, c_5) = (4.7 \times 10^{-3}, 2.7, 4.5, 4.2)$, the results are displayed in Figure 4.5.10.

4.5.3.5 Model 5

$$\Psi = c_1 \left(J - 1 \right)^2 + c_2 \left(\bar{I}_1 - 3 \right) + c_3 \left(\bar{I}_4 - 1 \right) + c_4 \left(\bar{I}_4 - 1 \right)^2 + c_5 \left(\bar{I}_5 - 1 \right)$$

For the parameters $(c_1, c_2, c_3, c_4, c_5) = (4.8 \times 10^{-3}, 1.7, 3.8, 3.6, 3.8)$, the results are shown in Figure 4.5.11.

4.5.3.6 Model 6

$$\Psi = c_1 \left(J - 1 \right)^2 + c_2 \left(\bar{I}_1 - 3 \right) + c_3 \left(\bar{I}_1 - 3 \right)^2 + c_4 \left(\bar{I}_4 - 1 \right) + c_5 \left(\bar{I}_4 - 1 \right)^2 + c_6 \left(\bar{I}_5 - 1 \right)$$

For the parameters $(c_1, c_2, c_3, c_4, c_5, c_6) = (8.0 \times 10^{-3}, 9.9, -3.7, 45, 36, -7.2)$, the results are presented in Figure 4.5.12.

4.5.3.7 Model 7

$$
\begin{aligned}
\Psi = {} & 1/c_1 \left(J - 1 \right)^2 + c_3 \left(\bar{I}_1 - 3 \right)^2 + c_2 \left(\bar{I}_1 - 3 \right) + c_4 \left(\bar{I}_1 - 3 \right)^3 + c_5 \left(\bar{I}_2 - 3 \right) + c_6 \left(\bar{I}_2 - 3 \right)^2 + c_7 \left(\bar{I}_2 - 3 \right)^3 + \\
& c_8 \left(\bar{I}_4 - 1 \right) + c_9 \left(\bar{I}_4 - 1 \right)^2 + c_{10} \left(\bar{I}_4 - 1 \right)^3 + c_{11} \left(\bar{I}_4 - 1 \right)^4 + c_{12} \left(\bar{I}_5 - 1 \right) + c_{13} \left(\bar{I}_5 - 1 \right)^2 + c_{14} \left(\bar{I}_5 - 1 \right)^3 + \\
& c_{15} \left(\bar{I}_5 - 1 \right)^4 + c_{16} \left(\bar{I}_5 - 1 \right) \left(\bar{I}_1 - 3 \right) + c_{17} \left(\bar{I}_5 - 1 \right)^2 \left(\bar{I}_1 - 3 \right)^2 + c_{18} \left(\bar{I}_5 - 1 \right) \left(\bar{I}_2 - 3 \right) + \\
& c_{19} \left(\bar{I}_5 - 1 \right)^2 \left(\bar{I}_2 - 3 \right)^2 + c_{20} \left(\bar{I}_4 - 1 \right) \left(\bar{I}_2 - 3 \right) + c_{21} \left(\bar{I}_4 - 1 \right)^2 \left(\bar{I}_2 - 3 \right)^2 + c_{22} \left(\bar{I}_4 - 1 \right) \left(\bar{I}_1 - 3 \right) + \\
& c_{23} \left(\bar{I}_4 - 1 \right)^2 \left(\bar{I}_1 - 3 \right)^2 + c_{24} \left(\bar{I}_4 - 1 \right) \left(\bar{I}_5 - 1 \right) + c_{25} \left(\bar{I}_4 - 1 \right)^2 \left(\bar{I}_5 - 1 \right)^2
\end{aligned}
$$

$$\Psi = c_1 \left(J - 1\right)^2 + c_2 \left(\bar{I}_1 - 3\right) + c_3 \left(\bar{I}_4 - 1\right) + c_4 \left(\bar{I}_4 - 1\right)^2$$
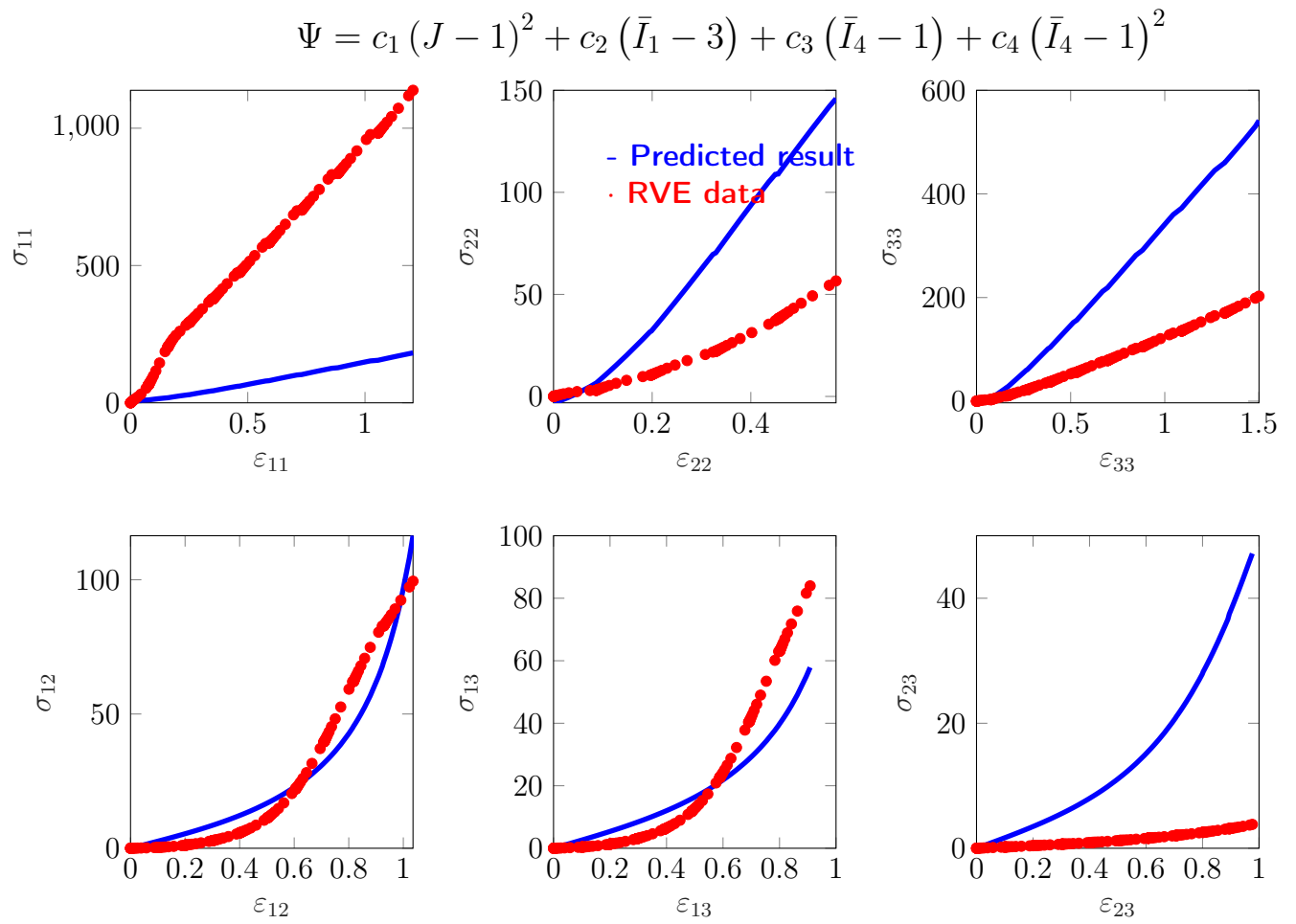
Figure 4.5.7: Results of model 1. Blue shows predicted results, and red shows the RVEresult.

$$\Psi = c_1 \left(J - 1\right)^2 + c_2 \left(\bar{I}_1 - 3\right) + c_3 \left(\bar{I}_4 - 1\right) + c_4 \left(\bar{I}_4 - 1\right)^2$$
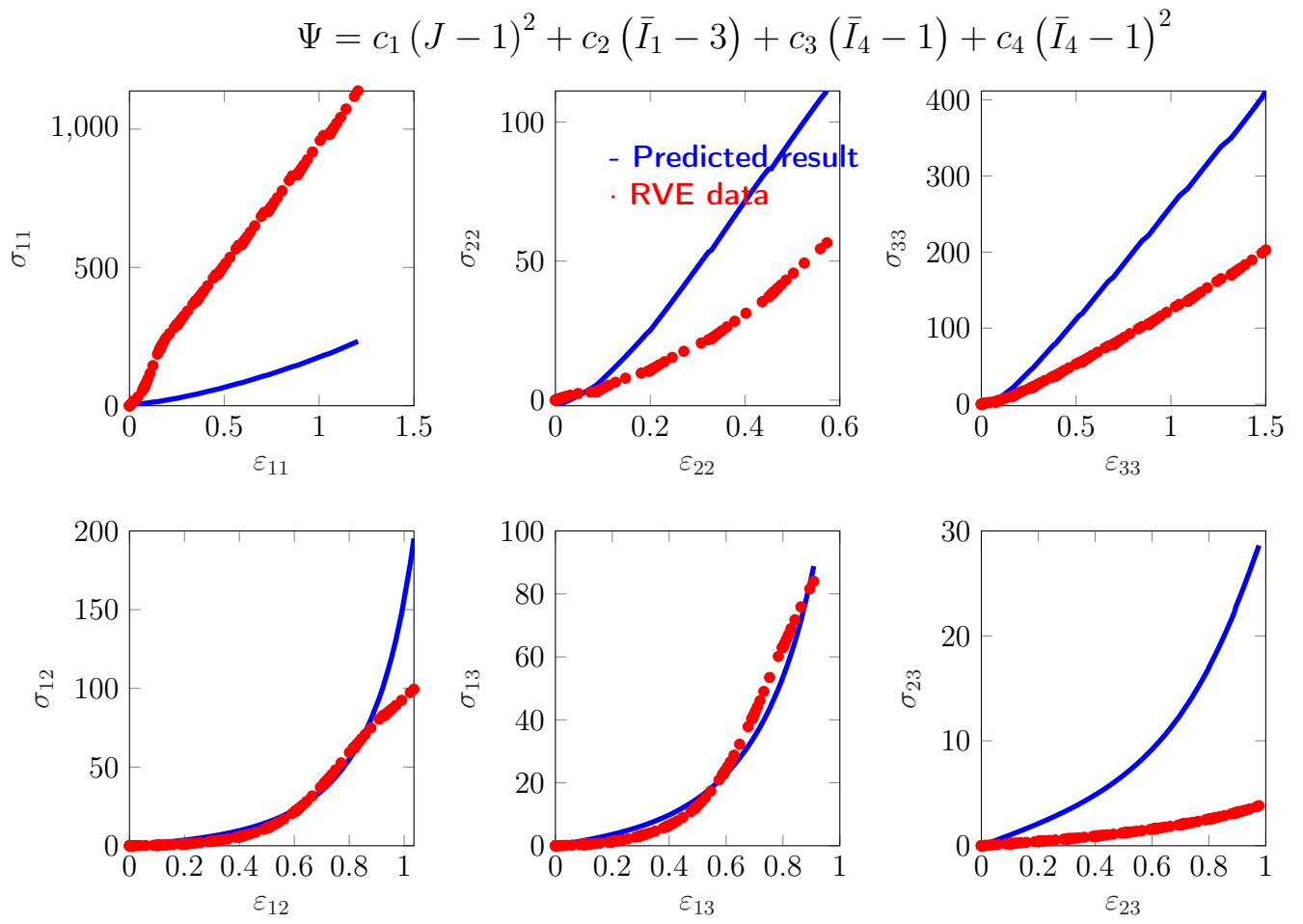
Figure 4.5.8: Results of model 2. Blue shows predicted results, and red shows the RVEresult.

$$\Psi = c_1 \left(J - 1\right)^2 + c_2 \left(\bar{I}_1 - 3\right) + c_3 \left(\bar{I}_4 - 1\right) + c_4 \left(\bar{I}_4 - 1\right)^2$$
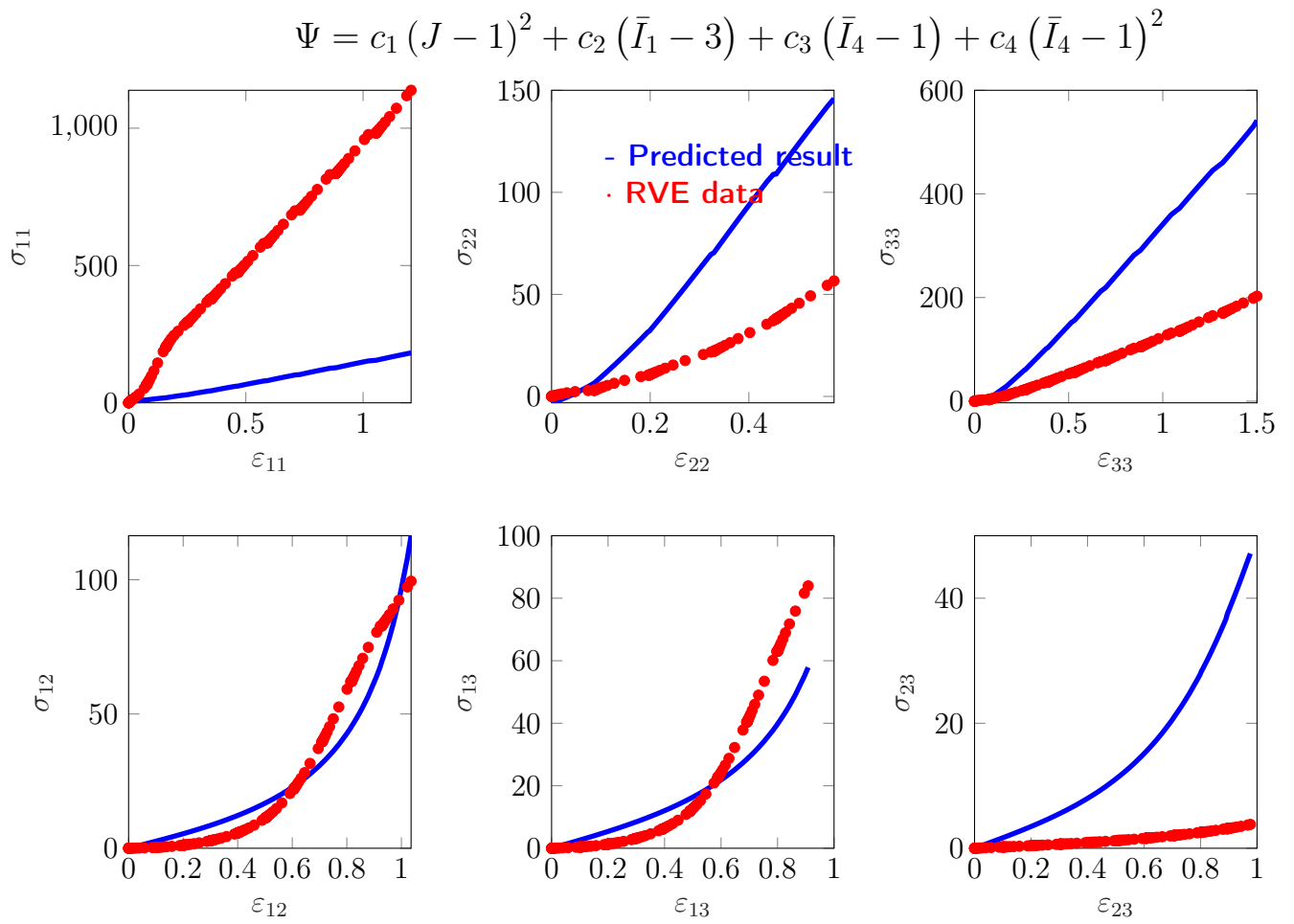
Figure 4.5.9: Results of model 3. Blue shows predicted results, and red shows the RVEresult.

$$\Psi = c_1 \left(J - 1 \right)^2 + c_2 \left(\bar{I}_1 - 3 \right) + c_3 \left(\bar{I}_4 - 1 \right) + c_4 \left(\bar{I}_5 - 1 \right)$$
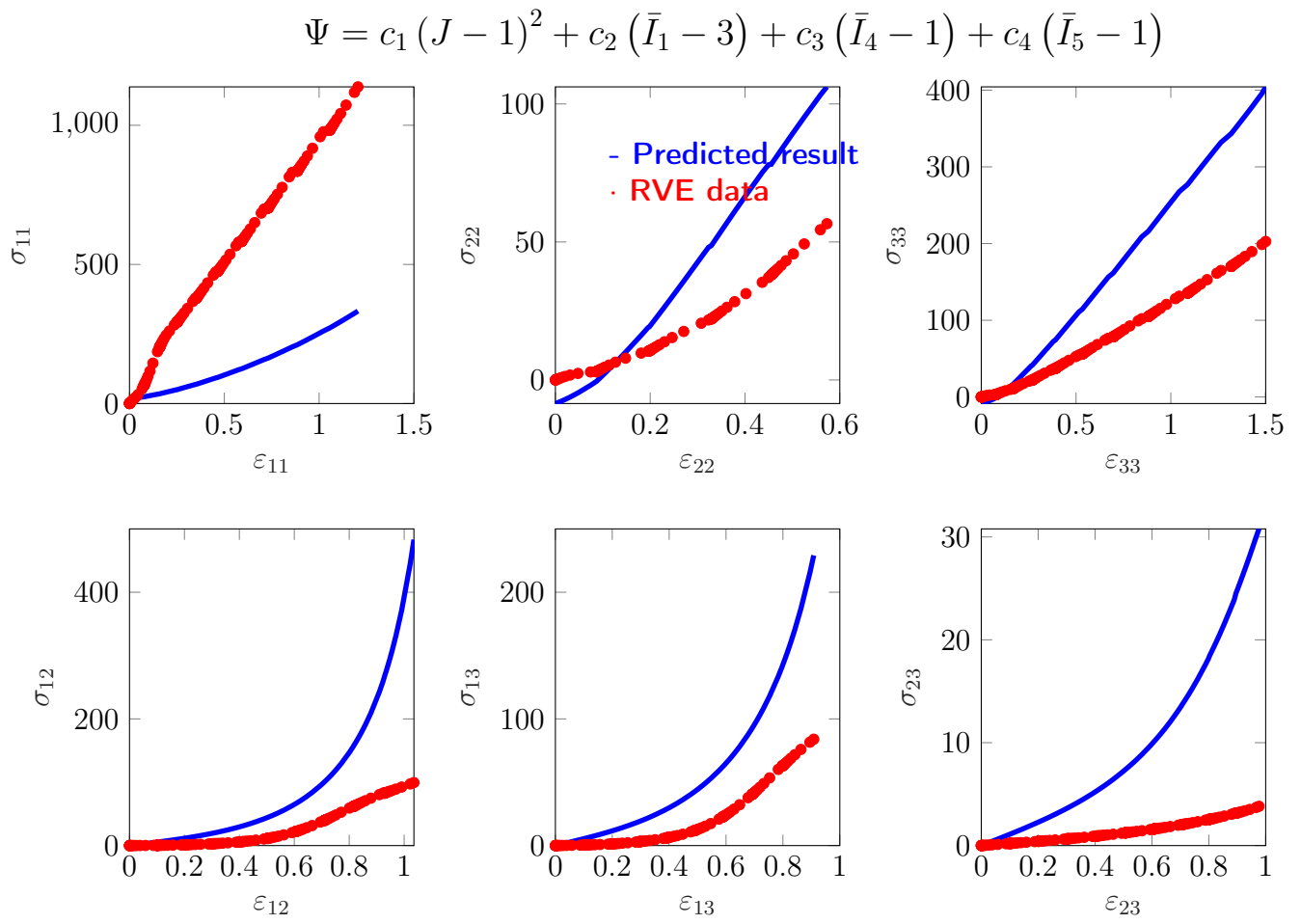
Figure 4.5.10: Results of model 4. Blue shows predicted results, and red shows the RVEresult.

$$\Psi = c_1 \left(J - 1\right)^2 + c_2 \left(\bar{I}_1 - 3\right) + c_3 \left(\bar{I}_4 - 1\right) + c_4 \left(\bar{I}_4 - 1\right)^2 + c_5 \left(\bar{I}_5 - 1\right)$$
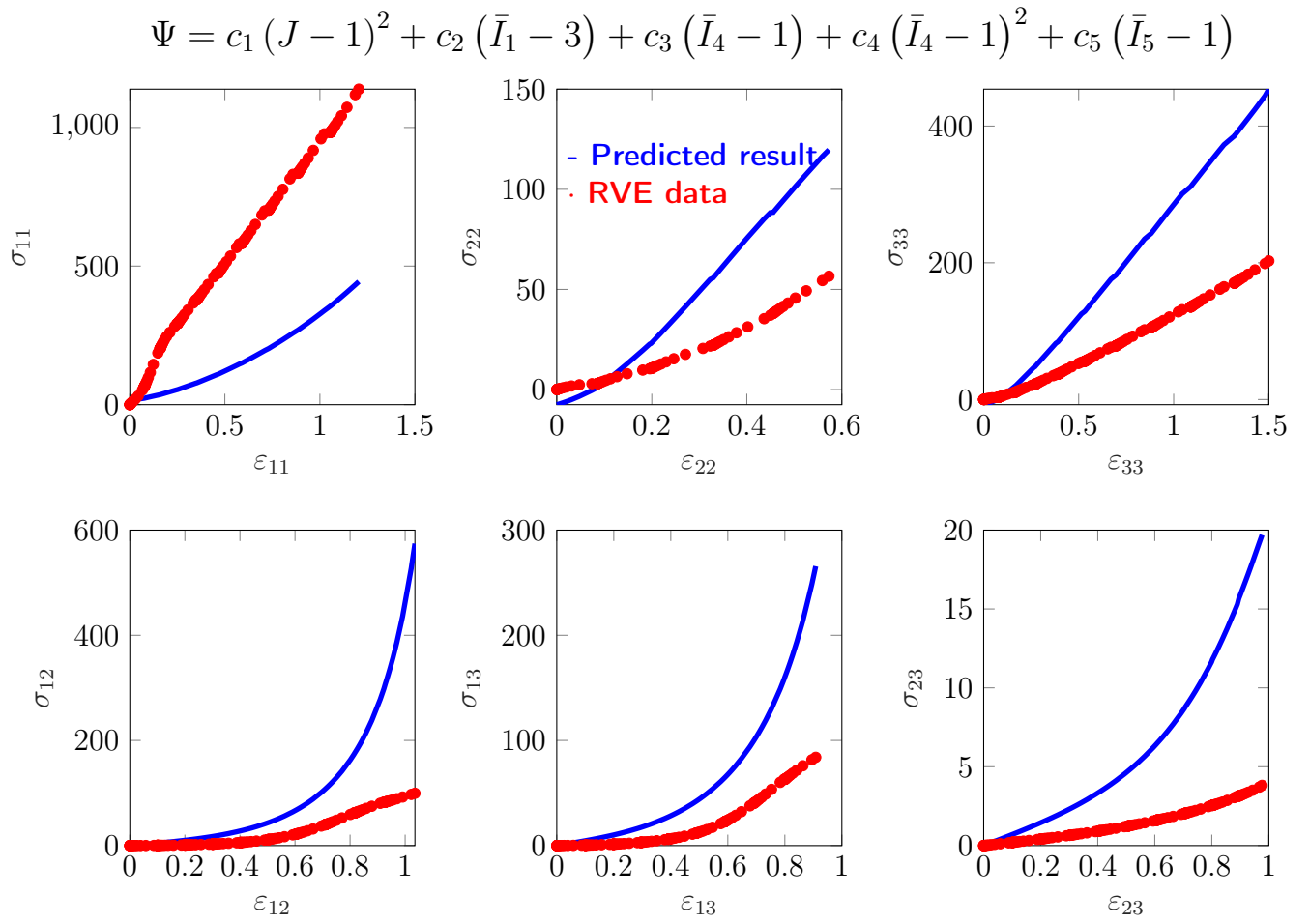
Figure 4.5.11: Results of model 5. Blue shows predicted results, and red shows the RVEresult.

$$_1 \left(J-1\right)^2 + c_2 \left(\bar{I}_1 - 3\right) + c_3 \left(\bar{I}_1 - 3\right)^2 + c_4 \left(\bar{I}_4 - 1\right) + c_5 \left(\bar{I}_4 - 1\right)^2 + c_6 \left(\bar{I}_5 - 1\right)$$
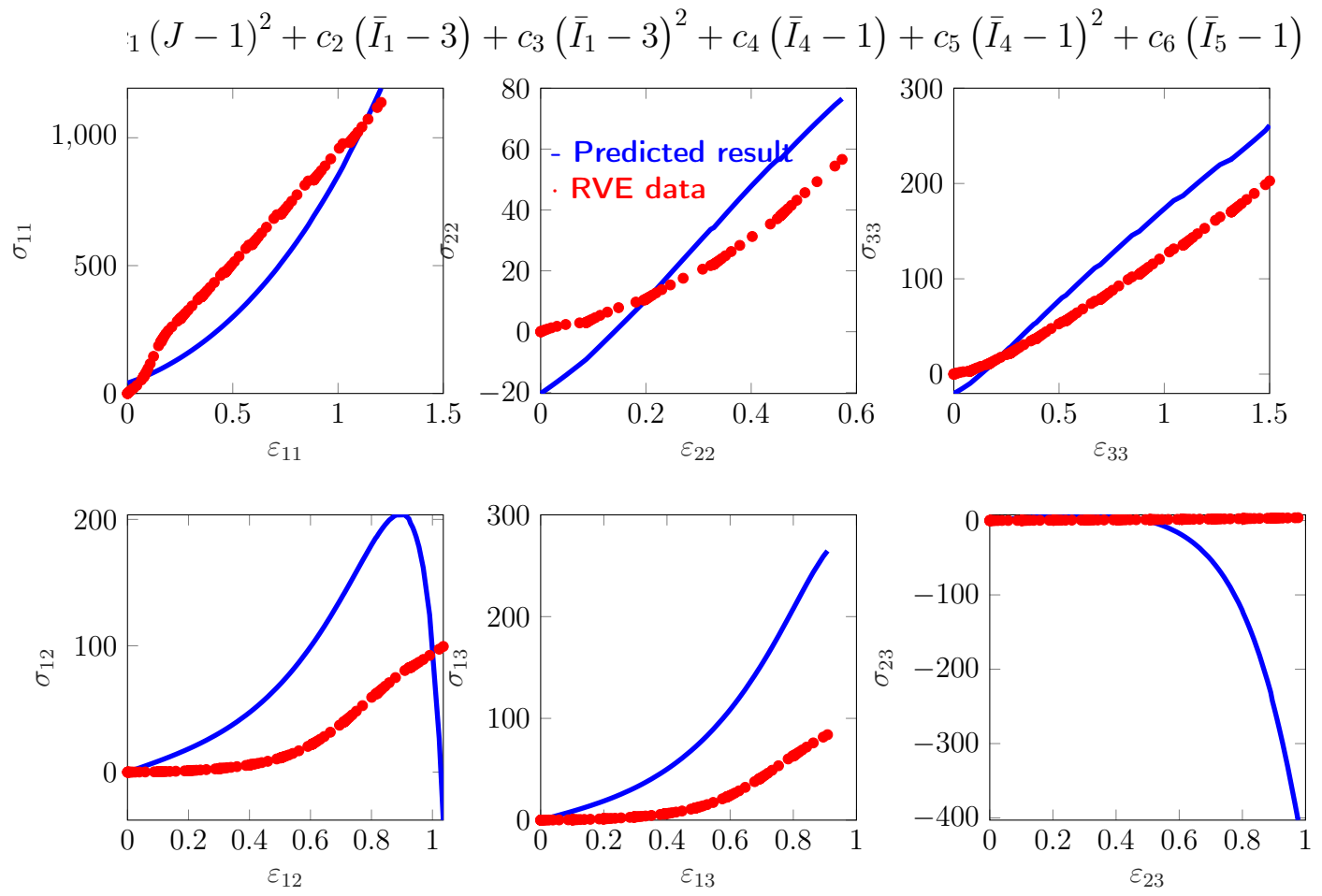
Figure 4.5.12: Results of model 6. Blue shows predicted results, and red shows the RVEresult.

For the parameters,

$$(c_1, c_2, c_3, c_4, c_5) = \left(530 \times 10^{-3}, 7.1, -4.9, 4.7, -22\right)$$
$$(c_6, c_7, c_8, c_9, c_{10}) = (-4.8, 6.9, 24, 37, 17)$$
$$(c_{11}, c_{12}, c_{13}, c_{14}, c_{15}) = \left(-1.9, 2.0, 5.7, -1.4, -17 \times 10^{-3}\right)$$
$$(c_{16}, c_{17}, c_{18}, c_{19}, c_{20}) = (-25, 2.0, -28, 1.2, -21)$$
$$(c_{21}, c_{22}, c_{23}, c_{24}, c_{25}) = (-11, -15, -7.5, 28, 1.3)$$

, the results are depicted in Figure 4.5.13.

4.5.4 Discussion on results

The L_2 error all these models can be summarized in Table 4.5.1.

Model Name	L_2 Error
Model 1	9.2×10^3
Model 2	8.1×10^3
Model 3	8.3×10^3
Model 4	8.8×10^3
Model 5	9.0×10^3
Model 6	5.0×10^3
Model 7	720
Linear anisotropic model	2.3×10^3
Nonlinear anisotropic model	290

Table 4.5.1: Results of fitting all models of RVE data

From model 1 to model 5, the number of iterations remained constant at $28\,000$. A notable drop in error occurs starting from model 6, attributed to the inclusion of both terms $\bar{I}_4$ and $\bar{I}_5$, along with the increased complexity of the model. As the model's complexity rises, its capacity increases, but caution is necessary to prevent excessive capacity that could lead to overfitting.

Model 7 outperforms all other invariant-based models, fitting exceptionally well. Despite its complexity, featuring 25 terms and intricate formulations, including coupling terms between $\bar{I}_4$ and $\bar{I}_3$, training this model proved to be the slowest process. While it fits well compared to other models, it encounters challenges in fitting the σ_{23} data, a recurring issue observed in other models.

A hypothesis arises regarding the inaccurate shear response of σ_{23}, suggesting the need for further experimentation to refine models for both rubber and the chord. The chord's Marlow model, based on uni-dimensional data lacking volumetric effects, and the rubber's Mooney-Rivlin model, accurate but potentially limited in its range of strain, warrant verification through experimentation. If time permits, measuring the shear response of the fabric layer could address these uncertainties.

$$\Psi = 1/c_1 \left(J - 1 \right)^2 + c_3 \left(\bar{I}_1 - 3 \right)^2 + c_2 \left(\bar{I}_1 - 3 \right) + c_4 \left(\bar{I}_1 - 3 \right)^3 +$$

$$c_5 \left(\bar{I}_2 - 3 \right) + c_6 \left(\bar{I}_2 - 3 \right)^2 + c_7 \left(\bar{I}_2 - 3 \right)^3 + c_8 \left(\bar{I}_4 - 1 \right) +$$

$$c_9 \left(\bar{I}_4 - 1 \right)^2 + c_{10} \left(\bar{I}_4 - 1 \right)^3 + c_{11} \left(\bar{I}_4 - 1 \right)^4 +$$

$$c_{12} \left(\bar{I}_5 - 1 \right) + c_{13} \left(\bar{I}_5 - 1 \right)^2 + c_{14} \left(\bar{I}_5 - 1 \right)^3 +$$

$$c_{15} \left(\bar{I}_5 - 1 \right)^4 + c_{16} \left(\bar{I}_5 - 1 \right) \left(\bar{I}_1 - 3 \right) + c_{17} \left(\bar{I}_5 - 1 \right)^2 \left(\bar{I}_1 - 3 \right)^2 +$$

$$c_{18} \left(\bar{I}_5 - 1 \right) \left(\bar{I}_2 - 3 \right) + c_{19} \left(\bar{I}_5 - 1 \right)^2 \left(\bar{I}_2 - 3 \right)^2 +$$

$$c_{20} \left(\bar{I}_4 - 1 \right) \left(\bar{I}_2 - 3 \right) + c_{21} \left(\bar{I}_4 - 1 \right)^2 \left(\bar{I}_2 - 3 \right)^2 + c_{22} \left(\bar{I}_4 - 1 \right) \left(\bar{I}_1 - 3 \right) +$$

$$c_{23} \left(\bar{I}_4 - 1 \right)^2 \left(\bar{I}_1 - 3 \right)^2 + c_{24} \left(\bar{I}_4 - 1 \right) \left(\bar{I}_5 - 1 \right) + c_{25} \left(\bar{I}_4 - 1 \right)^2 \left(\bar{I}_5 - 1 \right)^2$$

Figure 4.5.13: Results of model 7. Blue shows predicted results, and red shows the RVEresult.

Additionally, the modeling of the interaction layer or interface layer between the fiber and rubber was overlooked in the current homogenization model. While the model defines the regions of the fiber and matrix, the integration region between the fiber and rubber is not specified, potentially influencing the results.

The strain-based approach yields significantly better results than the invariant-based approach. However, even in the strain-based approach, the model encounters challenges with the σ_{23} data, aligning with the earlier hypothesis. Stability problems, stemming from negative eigenvalues in the stiffness matrix and a high condition number, further contribute to the model's limitations. The high condition number suggests instability in the data, where small changes in values can lead to disproportionately large changes in results, a condition incompatible with realistic simulations.

Chapter 5

Conclusion

In this study, a dedicated plugin for ABAQUS has been developed to facilitate the comprehensive homogenization process for two-phase materials. The outcomes generated by this plugin have been rigorously compared with theoretical homogenization results, demonstrating a consistent agreement.

Subsequently, distinct constitutive models were formulated, specifically tailored for the bellows of air springs. These constitutive models were derived through both strain-based and invariant-based approaches. Furthermore, the plugin underwent additional refinements to effectively address nonlinear responses in the material behavior.

When comparing the results obtained from the strain-based and invariant-based approaches, the strain-based method exhibited a better fit. However, this superiority was accompanied by stability issues, arising from negative eigenvalues in the stiffness matrix and a high condition number. In contrast, the invariant-based approach provided a more stable solution, although it did not fully align with the RVE data.

In the invariant-based modeling, seven distinct models were developed, each incrementally increasing in complexity. As the models became more intricate, their capacity to generalize responses improved. Despite these advancements, accurately capturing all six modes proved to be a challenging task for any model. Model 7, boasting 25 parameters, emerged as the most accurate solution among all models. This trend suggests that increasing the complexity of the model enhances its ability to capture responses more accurately.

It's noteworthy that the optimization algorithm tailored for parameter optimization outperformed default algorithms such as *fmincon* and *fminsearch*. For instance, the *fminsearch* algorithm failed to find a solution for Model 1.

A substantial disparity exists in the shear values, notably between σ_{23} and $(\sigma_{12}, \ \sigma_{13})$. Effectively capturing this difference proves challenging for any model. Furthermore, a significant gap is observed between the net bulk modulus and shear modulus, presenting an additional challenge in accurate representation. This notable difference appears unrealistic and can be attributed to the lack of precision in the material model descriptions for both the chord and rubber components.

Enhancing the accuracy of material models for chord and rubber necessitates comprehensive experimental characterizations, including pure shear tests in various directions. Unfortunately, due to time constraints within the scope of this thesis, such detailed experimental work could not be undertaken.

The tools created in the course of this project offer portability and applicability to diverse projects. The material calibration tool, designed to determine parameters for constitutive models, is not limited to the current material models and can be adapted for use with other models.

Utilizing the symbolic math toolbox in Matlab, the derivatives of the energy potential were accurately computed, showcasing the successful automation of this intricate process. Additionally, the entire plugin workflow has been automated, ensuring ease of use and accessibility for a wide range of applications.

Several avenues for improvement and expansion can be pursued in future research. Incorporating plasticity, damage, and fatigue considerations into the existing models would enhance their predictive capabilities, providing a more comprehensive representation of real-world material behavior.

To fully exploit the potential of this work, a comprehensive experimental investigation is essential to accurately capture the response of the fabric layer. Once the fabric layer aligns with experimental results, the model should progress to the meso scale. At this stage, fabric layers can be stacked at different angles and with varied sequences, introducing complexity. The meso-scale results should be rigorously compared with experimentation to validate the accuracy of the model.

Subsequently, the model can be further extended to the macro scale, necessitating additional experimentation for validation. Comparing macro-scale predictions with experimental results, especially under different stack sequences, is crucial for confirming the model's reliability at a larger scale.

Upon successful alignment of macro-scale predictions with experimental outcomes, the comprehensive journey from micro to macro will be complete. This work, having focused on micromechanics modeling, lays the groundwork for future studies. The developed tools, designed for versatility, can continue to be valuable assets in the exploration of more intricate material behaviors and structures.

Appendices

The development of constitutive modeling equations in this work involves the use of tensor algebra. Appendix A serves as a valuable reference, summarizing the notations employed throughout the thesis. Additionally, for readers less familiar with these notations, it aims to facilitate comprehension by presenting mathematical results in a concise manner. The formatting style of these appendices draws inspiration from [18].

Appendix A initiates with the outcomes of dyadic products for second-order tensors. It delineates the results for overbar dyadic products, followed by underbar dyadic products. The presentation then introduces essential tensor derivatives, delving into major and axis symmetries concerning fourth-order tensors. Furthermore, it sheds light on the derivatives of tensor-valued functions and scalar-valued functions with tensor arguments. The appendix concludes by elucidating symmetric tensor derivatives and incorporating the definitions of Gauss divergence theorem and Reynolds transport theorem, the latter of which is then proven. For a comprehensive exploration of these concepts, additional details can be found in [19].

In contrast, Appendix B provides a succinct introduction to Fortran. Covering vital concepts such as spaces, columns, line continuation, and comments, it offers an overview of essential Fortran elements. The discussion extends to variable declaration, variable dimensioning, debugging techniques, and the intricacies of subroutines, equipping readers with foundational insights into the Fortran programming language.

Appendix A

Mathematical Preliminaries

A.1 Continuum Mechanics Reference

A.1.1 Dyadic Products

A.1.1.1 Dyadic Product, $\{\boldsymbol{A} \otimes \boldsymbol{B}\}_{ijkl} = \boldsymbol{A}_{ij}\boldsymbol{B}_{kl}$

$$[\boldsymbol{I} \otimes \boldsymbol{I}] : \boldsymbol{A} = \mathsf{tr}(\boldsymbol{A})\boldsymbol{I} \tag{A.1.1}$$

$$[\boldsymbol{A} \otimes \boldsymbol{B}] : \boldsymbol{C} = \boldsymbol{A}[\boldsymbol{B} : \boldsymbol{C}] \tag{A.1.2}$$

$$\boldsymbol{C} : [\boldsymbol{A} \otimes \boldsymbol{B}] = [\boldsymbol{C} : \boldsymbol{A}]\boldsymbol{B} \tag{A.1.3}$$

A.1.1.2 Overbar Dyadic Product, $\{\boldsymbol{A}\overline{\otimes}\boldsymbol{B}\}_{ijkl} = \boldsymbol{A}_{ik}\boldsymbol{B}_{jl}$

$$[\boldsymbol{I}\overline{\otimes}\boldsymbol{I}] : \boldsymbol{A} = \boldsymbol{A} \tag{A.1.4}$$

$$[\boldsymbol{A}\overline{\otimes}\boldsymbol{B}] : \boldsymbol{C} = \boldsymbol{A}\boldsymbol{C}\boldsymbol{B}^{\mathrm{T}} \tag{A.1.5}$$

$$\boldsymbol{C} : [\boldsymbol{A}\overline{\otimes}\boldsymbol{B}] = \boldsymbol{A}^{\mathrm{T}}\boldsymbol{C}\boldsymbol{B} \tag{A.1.6}$$

$$\tag{A.1.7}$$

A.1.1.3 Underbar Dyadic Product, $\{\boldsymbol{A}\underline{\otimes}\boldsymbol{B}\}_{ijkl} = \boldsymbol{A}_{il}\boldsymbol{B}_{jk}$

$$[\boldsymbol{I}\underline{\otimes}\boldsymbol{I}] : \boldsymbol{A} = \boldsymbol{A}^{\mathrm{T}} \tag{A.1.8}$$

$$[\boldsymbol{A}\underline{\otimes}\boldsymbol{B}] : \boldsymbol{C} = \boldsymbol{A}\boldsymbol{C}^{\mathrm{T}}\boldsymbol{B}^{\mathrm{T}} \tag{A.1.9}$$

$$\boldsymbol{C} : [\boldsymbol{A}\underline{\otimes}\boldsymbol{B}] = \boldsymbol{B}^{\mathrm{T}}\boldsymbol{C}^{\mathrm{T}}\boldsymbol{A} \tag{A.1.10}$$

A.1.2 Useful Tensor Derivatives

$$\frac{\partial \boldsymbol{A}}{\partial \boldsymbol{A}} = \boldsymbol{I} \overline{\otimes} \boldsymbol{I} = \mathsf{I} \qquad\qquad \frac{\partial \boldsymbol{A}_{ij}}{\partial \boldsymbol{A}_{kl}} = \delta_{ik}\delta_{jl} \tag{A.1.11}$$

$$\frac{\partial \boldsymbol{A}^{\mathrm{T}}}{\partial \boldsymbol{A}} = \boldsymbol{I} \underline{\otimes} \boldsymbol{I} = \mathsf{I}^{\mathrm{T}} \qquad\qquad \frac{\partial \boldsymbol{A}_{ji}}{\partial \boldsymbol{A}_{kl}} = \delta_{il}\delta_{jk} \tag{A.1.12}$$

$$\frac{\partial \boldsymbol{A}^{-1}}{\partial \boldsymbol{A}} = -\boldsymbol{A}^{-1} \overline{\otimes} \boldsymbol{A}^{-\mathrm{T}} \qquad\qquad \frac{\partial \boldsymbol{A}_{ij}^{-1}}{\partial \boldsymbol{A}_{kl}} = -\boldsymbol{A}_{ik}^{-1}\boldsymbol{A}_{lj}^{-1} \tag{A.1.13}$$

$$\frac{\partial \boldsymbol{A}^{-\mathrm{T}}}{\partial \boldsymbol{A}} = -\boldsymbol{A}^{-\mathrm{T}} \underline{\otimes} \boldsymbol{A}^{-1} \qquad\qquad \frac{\partial \boldsymbol{A}_{ji}^{-1}}{\partial \boldsymbol{A}_{kl}} = -\boldsymbol{A}_{li}^{-1}\boldsymbol{A}_{jk}^{-1} \tag{A.1.14}$$

A.1.3 Major and Minor Symmetry

Fourth-order tensors can have major

$$\mathsf{A}_{IJKL} = \mathsf{A}_{KLIJ} \tag{A.1.15}$$

and/or minor symmetries:

$$\mathsf{A}_{IJKL} = \mathsf{A}_{JIKL} = \mathsf{A}_{IJLK} \tag{A.1.16}$$

Fourth-order tensors with minor symmetries can be written in Voigt notation as second-order tensors. Tensors that also have major symmetries appear symmetric in Voigt notation.

tensor notation	indicial notation	if $\boldsymbol{A}$ and $\boldsymbol{B}$ are symmetric	if $\boldsymbol{A} = \boldsymbol{B}$ also
$\boldsymbol{A} \otimes \boldsymbol{B}$	$\boldsymbol{A}_{IJ}\boldsymbol{B}_{KL}$	minor	major and minor
$\boldsymbol{A} \overline{\otimes} \boldsymbol{B}$	$\boldsymbol{A}_{IK}\boldsymbol{B}_{JL}$	major	major
$\boldsymbol{A} \overline{\otimes} \boldsymbol{B} + \boldsymbol{B} \overline{\otimes} \boldsymbol{A}$	$\boldsymbol{A}_{IK}\boldsymbol{B}_{JL} + \boldsymbol{A}_{JL}\boldsymbol{B}_{IK}$	major	(reduces to above)
$\boldsymbol{A} \underline{\otimes} \boldsymbol{B}$	$\boldsymbol{A}_{IL}\boldsymbol{B}_{JK}$	–	major
$\boldsymbol{A} \underline{\otimes} \boldsymbol{B} + \boldsymbol{B} \underline{\otimes} \boldsymbol{A}$	$\boldsymbol{A}_{IL}\boldsymbol{B}_{JK} + \boldsymbol{A}_{IL}\boldsymbol{B}_{JK}$	major	(reduces to above)
$\boldsymbol{A} \overline{\otimes} \boldsymbol{B} + \boldsymbol{A} \underline{\otimes} \boldsymbol{B}$	$\boldsymbol{A}_{IK}\boldsymbol{B}_{JL} + \boldsymbol{A}_{IL}\boldsymbol{B}_{JK}$	–	major and minor
$\boldsymbol{A} \overline{\otimes} \boldsymbol{B} + \boldsymbol{B} \underline{\otimes} \boldsymbol{A}$	$\boldsymbol{A}_{IK}\boldsymbol{B}_{JL} + \boldsymbol{A}_{JK}\boldsymbol{B}_{IL}$	ij minor symmetry	major and minor
$\boldsymbol{A} \overline{\otimes} \boldsymbol{B} + \boldsymbol{A} \underline{\otimes} \boldsymbol{B}$ $+\boldsymbol{B} \overline{\otimes} \boldsymbol{A} + \boldsymbol{B} \underline{\otimes} \boldsymbol{A}$	$\boldsymbol{A}_{IK}\boldsymbol{B}_{JL} + \boldsymbol{A}_{IL}\boldsymbol{B}_{JK}$ $+\boldsymbol{B}_{IK}\boldsymbol{A}_{JL} + \boldsymbol{B}_{IL}\boldsymbol{A}_{JK}$	major and minor	major and minor (reduces to above)

A.1.4 Tensor Derivatives

The derivative of a scalar-valued function $f(\boldsymbol{X})$ with respect to a tensor $\boldsymbol{X}$ is a tensor,

$$\left\{\frac{\partial f(\boldsymbol{X})}{\partial \boldsymbol{X}}\right\}_{IJ} = \frac{\partial f(\boldsymbol{X})}{\partial \boldsymbol{X}_{IJ}} \,. \tag{A.1.17}$$

It is defined as the tensor $f,_{\boldsymbol{X}}$ that satisfies the expression

$$\frac{d}{d\varepsilon} f\left(\boldsymbol{X} + \varepsilon d\boldsymbol{X}\right)\bigg|_{\varepsilon=0} = f,_{\boldsymbol{X}} : d\boldsymbol{X} \tag{A.1.18}$$

for all admissible variational tensors $d\boldsymbol{X}$.

The derivative of a tensor-valued function $\boldsymbol{F}(\boldsymbol{X})$ with respect to a tensor $\boldsymbol{X}$ is a fourth-order tensor,

$$\left\{\frac{\partial \boldsymbol{F}(\boldsymbol{X})}{\partial \boldsymbol{X}}\right\}_{IJKL} = \frac{\partial \boldsymbol{F}_{IJ}(\boldsymbol{X})}{\partial \boldsymbol{X}_{KL}} \,. \tag{A.1.19}$$

It is defined as the tensor $\boldsymbol{F},_{\boldsymbol{X}}$ that satisfies the expression

$$\frac{d}{d\varepsilon} \boldsymbol{F}\left(\boldsymbol{X} + \varepsilon d\boldsymbol{X}\right)\bigg|_{\varepsilon=0} = \boldsymbol{F},_{\boldsymbol{X}} : d\boldsymbol{X} \tag{A.1.20}$$

for all admissible variational tensors $d\boldsymbol{X}$.

A.1.4.1 Symmetric Tensor Derivatives

The derivative of a scalar-valued function $f(\boldsymbol{X})$ with respect to a symmetric tensor $\boldsymbol{X}$ is defined as any tensor $f,_{\boldsymbol{X}}$ that satisfies the expression

$$\frac{d}{d\varepsilon} f\left(\boldsymbol{X} + \varepsilon d\boldsymbol{X}\right)\bigg|_{\varepsilon=0} = f,_{\boldsymbol{X}} : d\boldsymbol{X} \tag{A.1.21}$$

for all *symmetric* variational tensors $d\boldsymbol{X}$ [24].

Thus defined, the derivative is clearly not unique, because $d\boldsymbol{X}$ is symmetric, and for any symmetric tensor $\boldsymbol{S}$ and any skew-symmetric tensor $\boldsymbol{W}$,

$$\boldsymbol{S} : \boldsymbol{W} = 0 \,. \tag{A.1.22}$$

Thus if a tensor $\boldsymbol{A}$ satisfies the equation, its symmetric part will also satisfy the equation by itself,

$$\boldsymbol{A} : d\boldsymbol{X} = \left[\boldsymbol{A}^{\mathrm{sym}} + \boldsymbol{A}^{\mathrm{skew}}\right] : d\boldsymbol{X} = \boldsymbol{A}^{\mathrm{sym}} : d\boldsymbol{X} + \overset{0}{\cancel{\boldsymbol{A}^{\mathrm{skew}} : d\boldsymbol{X}}} = \boldsymbol{A}^{\mathrm{sym}} : d\boldsymbol{X} \,. \tag{A.1.23}$$

To make the definition unique, then, we impose a further restriction: we require that the derivative itself be symmetric ($\left\{f,_{\boldsymbol{X}}\right\}_{IJ} = \left\{f,_{\boldsymbol{X}}\right\}_{JI}$). This eliminates the non-unique skew-symmetric parts. This is enforced by the definition of the symmetric part of a tensor:

$$\left\{f,_{\boldsymbol{X}}\right\}_{IJ} = \frac{1}{2}\left[\frac{\partial f(\boldsymbol{X})}{\partial \boldsymbol{X}_{IJ}} + \frac{\partial f(\boldsymbol{X})}{\partial \boldsymbol{X}_{JI}}\right] \,. \tag{A.1.24}$$

In this case, the derivative is naturally symmetric without enforcing it. This is true of derivatives that involve only a single symmetric tensor. However, in the case of the derivative of a tensor-valued function with respect to a tensor, we must further require that the derivative be symmetric in any and all slots in which the tensors themselves are symmetric. Thus, the derivative of a symmetric tensor with respect to itself is

$$\frac{\partial \boldsymbol{X}}{\partial \boldsymbol{X}} = \frac{1}{2}[\boldsymbol{I}\overline{\otimes}\boldsymbol{I} + \boldsymbol{I}\underline{\otimes}\boldsymbol{I}] = \mathsf{I}, \tag{A.1.25}$$

and the derivative of its inverse with respect to itself is

$$\frac{\partial \boldsymbol{X}^{-1}}{\partial \boldsymbol{X}} = -\frac{1}{2}\left[\boldsymbol{X}^{-1}\overline{\otimes}\boldsymbol{X}^{-1} + \boldsymbol{X}^{-1}\underline{\otimes}\boldsymbol{X}^{-1}\right]. \tag{A.1.26}$$

As expected, both expressions have all the major and minor symmetries.

This distinction between derivatives of symmetric and non-symmetric tensors is important when using Voigt notation, as only tensors with minor symmetries can be represented in Voigt notation. Thus, it is actually not possible to write derivatives of non-symmetric tensors (say, $\partial \boldsymbol{F}/\partial \boldsymbol{F}$) in Voigt notation. For more information, see Section A.1.3.

Definition A.1.1 (Gauss divergence theorem). *Let Ω is a subset of $\mathbb{R}^n$, which is compact and has piecewise smooth boundary $\partial\Omega$. If $\boldsymbol{F}$ is a vector field with continuous differentiablity in the neighborhood of Ω, then:*

$$\int_\Omega \nabla \cdot \boldsymbol{F}dV = \int_{\partial\Omega} \boldsymbol{F} \cdot \boldsymbol{n}dS$$

, in which dS, and dV, are area and volume elements, and $\boldsymbol{n}$ is an outward unit normal vector.

A.2 Reynold's Transport Theorem Proof

Let Ω_0 be reference configuration, and Ω_t be the current configuration. Let motion φ for the current configuration can be defined as,

$$\mathbf{x} = \varphi(\mathbf{X}, t),$$
$$\boldsymbol{F}(\mathbf{X}, t) = \nabla\varphi.$$

Let $J = \det(\boldsymbol{F})$. Define

$$\hat{\mathbf{f}}(\mathbf{X}, t) = \mathbf{f}(\varphi(\mathbf{X}, t), t).$$

Then the integrals in the current and the reference configurations are related by (from definition 2.1.5)

$$\int_{\Omega(t)} \mathbf{f}(\mathbf{x}, t)\, dv = \int_{\Omega_0} \mathbf{f}(\varphi(\mathbf{X}, t), t)\, J(\mathbf{X}, t)\, dV_0$$
$$= \int_{\Omega_0} \hat{\mathbf{f}}(\mathbf{X}, t)\, J(\mathbf{X}, t)\, dV_0.$$

Since, Ω_0 is not changing with time, if we take the time derivative, we can take it inside of the integral. Now by using the chain rule,

$$\frac{d}{dt}\left(\int_{\Omega(t)} \mathbf{f}(\mathbf{x},t)\,dv\right) = \int_{\Omega_0} \frac{\partial}{\partial t}\left(\hat{\mathbf{f}}(\mathbf{X},t)\,J(\mathbf{X},t)\right)\,dV_0$$

$$= \int_{\Omega_0}\left(\frac{\partial}{\partial t}\left(\hat{\mathbf{f}}(\mathbf{X},t)\right)J(\mathbf{X},t) + \hat{\mathbf{f}}(\mathbf{X},t)\frac{\partial}{\partial t}\left(J(\mathbf{X},t)\right)\right)\,dV_0.$$

The time derivative of J is given

Definition A.2.1 (time derivative of J).

$$\frac{\partial J(\mathbf{X},t)}{\partial t} = J(\mathbf{X},t)\,\boldsymbol{\nabla}\cdot\mathbf{v}(\mathbf{x},t)$$

Proof.

$$\frac{\partial J(\mathbf{X},t)}{\partial t} = \frac{\partial}{\partial t}(\det \boldsymbol{F})$$

$$= (\det \boldsymbol{F})\operatorname{tr}\left(\boldsymbol{F}^{-1}\frac{\partial \boldsymbol{F}}{\partial t}\right)$$

$$= (\det \boldsymbol{F})\operatorname{tr}\left(\frac{\partial \boldsymbol{X}}{\partial \boldsymbol{\varphi}}\frac{\partial}{\partial t}\left(\frac{\partial \boldsymbol{\varphi}}{\partial \boldsymbol{X}}\right)\right)$$

$$= (\det \boldsymbol{F})\operatorname{tr}\left(\frac{\partial \boldsymbol{X}}{\partial \boldsymbol{\varphi}}\frac{\partial}{\partial \boldsymbol{X}}\left(\frac{\partial \boldsymbol{\varphi}}{\partial t}\right)\right)$$

$$= (\det \boldsymbol{F})\operatorname{tr}\left(\frac{\partial}{\partial \boldsymbol{x}}\left(\frac{\partial \boldsymbol{\varphi}}{\partial t}\right)\right)$$

$$= (\det \boldsymbol{F})(\boldsymbol{\nabla}\cdot\mathbf{v})$$

$$= J(\mathbf{X},t)\,\boldsymbol{\nabla}\cdot\mathbf{v}\big(\boldsymbol{\varphi}(\mathbf{X},t),t\big)$$

$$= J(\mathbf{X},t)\,\boldsymbol{\nabla}\cdot\mathbf{v}(\mathbf{x},t).$$

$\square$

Therefore,

$$\frac{d}{dt}\left(\int_{\Omega(t)} \mathbf{f}(\mathbf{x},t)\,dv\right) = \int_{\Omega_0}\left(\frac{\partial}{\partial t}\left(\hat{\mathbf{f}}(\mathbf{X},t)\right)J(\mathbf{X},t) + \hat{\mathbf{f}}(\mathbf{X},t)\,J(\mathbf{X},t)\,\boldsymbol{\nabla}\cdot\mathbf{v}(\mathbf{x},t)\right)dV_0$$

$$= \int_{\Omega_0}\left(\frac{\partial}{\partial t}\left(\hat{\mathbf{f}}(\mathbf{X},t)\right) + \hat{\mathbf{f}}(\mathbf{X},t)\,\boldsymbol{\nabla}\cdot\mathbf{v}(\mathbf{x},t)\right)J(\mathbf{X},t)\,dV_0$$

$$= \int_{\Omega(t)}\left(\dot{\mathbf{f}}(\mathbf{x},t) + \mathbf{f}(\mathbf{x},t)\,\boldsymbol{\nabla}\cdot\mathbf{v}(\mathbf{x},t)\right)dv.$$

where $\dot{\mathbf{f}}$ is the material time derivative of $\mathbf{f}$. The material derivative is given by

$$\dot{\mathbf{f}}(\mathbf{x}, t) = \frac{\partial \mathbf{f}(\mathbf{x}, t)}{\partial t} + \left(\boldsymbol{\nabla} \mathbf{f}(\mathbf{x}, t) \right) \cdot \mathbf{v}(\mathbf{x}, t). \tag{A.2.1}$$

Therefore,

$$\frac{d}{dt} \left(\int_{\Omega(t)} \mathbf{f}(\mathbf{x}, t) \, dv \right) = \int_{\Omega(t)} \left(\frac{\partial \mathbf{f}(\mathbf{x}, t)}{\partial t} + \left(\boldsymbol{\nabla} \mathbf{f}(\mathbf{x}, t) \right) \cdot \mathbf{v}(\mathbf{x}, t) + \mathbf{f}(\mathbf{x}, t) \, \boldsymbol{\nabla} \cdot \mathbf{v}(\mathbf{x}, t) \right) \, dv,$$

or,

$$\frac{d}{dt} \left(\int_{\Omega(t)} \mathbf{f} \, dv \right) = \int_{\Omega(t)} \left(\frac{\partial \mathbf{f}}{\partial t} + \boldsymbol{\nabla} \mathbf{f} \cdot \mathbf{v} + \mathbf{f} \, \boldsymbol{\nabla} \cdot \mathbf{v} \right) \, dv.$$

Using the identity

$$\boldsymbol{\nabla} \cdot (\mathbf{v} \otimes \mathbf{w}) = \mathbf{v}(\boldsymbol{\nabla} \cdot \mathbf{w}) + \boldsymbol{\nabla} \mathbf{v} \cdot \mathbf{w},$$

we then have

$$\frac{d}{dt} \left(\int_{\Omega(t)} \mathbf{f} \, dv \right) = \int_{\Omega(t)} \left(\frac{\partial \mathbf{f}}{\partial t} + \boldsymbol{\nabla} \cdot (\mathbf{f} \otimes \mathbf{v}) \right) \, dv. \tag{A.2.2}$$

Using the divergence theorem $\left(\int_{\Omega} \boldsymbol{\nabla} \cdot (\bullet) \, dv = \int_{\partial \Omega} (\bullet) \, da \right)$ and the identity $(\boldsymbol{a} \otimes \boldsymbol{b} \cdot \boldsymbol{n} = (\boldsymbol{b} \cdot \boldsymbol{n}) \, \boldsymbol{a})$, we have

$$\begin{aligned}
\frac{d}{dt} \left(\int_{\Omega(t)} \mathbf{f} \, dv \right) &= \int_{\Omega(t)} \frac{\partial \mathbf{f}}{\partial t} \, dv + \int_{\partial \Omega(t)} (\mathbf{f} \otimes \mathbf{v}) \cdot \mathbf{n} \, da \\
&= \int_{\Omega(t)} \frac{\partial \mathbf{f}}{\partial t} \, dv + \int_{\partial \Omega(t)} (\mathbf{v} \cdot \mathbf{n}) \mathbf{f} \, da. \qquad \square
\end{aligned}$$

Appendix B

A Brief Introduction to Fortran

Abaqus user subroutines use Fortan 90/95.

B.1   Case and Whitespace

Fortran is case-insenstive (`dfgrd1 = DFGRD1`). Whitespace (spaces) are also ignored beyond the significance of the reserved colums (see below).

> "Consistently separating words by spaces became a general custom about the tenth century A.D.,
> and lasted until about 1957, when FORTRAN abandoned the practice."
> — Sun FORTRAN Reference Manual .

B.2   Columns

A relic of Fortran's use on punch cards, the first 6 columns are reserved for special use.

B.2.1   Comments

A c in column 1 results in a full line comment. To append a comment to the end of a line of code, use a !

B.2.2   Line Continuation

Any character in column 6 signifies that the line is a continuation of the previous line.

B.2.3 Declaration and Initialization

B.2.4 Declaring Variables

Variables should be declared, indicating their type and size, and initialized before use. To disable implicit declarations, you should include the statement `implicit none`. Otherwise, mistyped variables will be treated as new variables (with a random value) and no warning will be generated.

Examples of declarations:

- `character*80 string1` 80-character long string
- `real*8 var1` double precision floating point number with 15 significant digits
- `integer int1` integer (of default 4-byte size)

B.2.4.1 Dimensioning Variables

When an array is passed into a subroutine as an argument, what is really passed is usually the memory address of the beginning of the array. For this reason, the dimension of each array must also be specified. This is done using a `dimension` statement.

- `real x(*)` x is an input vector, but no information is given about its dimensions. Note that this can only be used for the last dimension of an array.
- `real x(3)` x is an one-dimensional array (vector) of length 3
- `real x(3,2)` x is a two-dimensional array with 3 rows and 2 columns
- `real x(m,n)` x is a two-dimensional array with m rows and n columns

B.2.4.2 Initializing Variables

Variables must be initialized, or given a value, before they are used. Fortran will not necessarily throw an error if a variable is used uninitialized; instead it will use a junk value.

To initialize an array $(1, 2, 3)$

```
1 real*8 examplearray(3)
  data examplearray /1.d0, 2.d0, 3.d0/
```

To initialize an array $(2, 2, 2)$

```
real*8 examplearray(3)
data examplearray /2.d0, 2.d0, 2.d0/
```

or

```
real*8 examplearray(3)
data examplearray / 3 * 2.d0/
```

The `data` command is only performed once, so initialize all needed vectors and tensors in a single command. Additionally, in user subroutines, the `data` command is only executed at the beginning of the job, so data initialization of this form should only be used for static variables.

Double precision numbers must be initialized as such to avoid rounding to a single precision number:

- `1.d0`

- `3.1415926535d0`

B.2.5 Producing Output

The simplest form of an I/O statement is
`WRITE(*,*) item1, item2`
where the first asterisk means that the input goes to the screen and the second asterisk means that the computer determines the format of the output based on the type of the data.

The more general form of I/O allows data transfer to files, the terminal, printers, etc.
`WRITE(unit #, format, options) item1, item2, . . .`
where the unit number has an association with a particular device. Reserved unit numbers in Fortran include

- 5 - input from the keyboard (for READ statements)

- 6 - output to the screen (for WRITE statements)

while some Abaqus-specific unit numbers include:

- 6 - output to the printed output (.dat) file

- 7 - output to the message (.msg) file

Other files can be associated with a unit number with an `OPEN` statement:
`OPEN(UNIT=n, FILE='filename', options ...)`

A `PRINT` statement is a `WRITE` statement that outputs to the default device, generally the terminal screen.

B.2.6 Debugging

An easy way to debug Fortran programs is to use print statements.

- `print *, 'Hello, world!'`

- `print *, "The solution is ", x`

Commas separate the items to be printed. Single or double quotes may be used.

B.2.7 Subfunctions

The basic structure of a subfunction is:

```fortran
        subroutine SubroutineName(arg1, arg2)
        implicit none
 3      real*8  arg1, arg2 ! declaration

  c...   subroutine code goes here


        return
 8      end
```

Subroutines in Fortran don't have explicit outputs; instead, the subroutine modifies some or all of its variables, which are substituted back for the original variables in the main program. Variables that are defined as 'passed in for information' must not be altered, at the risk of unpredictable results.

Subroutines are called using `call SubroutineName(arg1, arg2)`

B.2.8 Tensor Toolbox

Tensor Toolbox is a Fortran module that calculates tensor features, including identity tensors, dot products, and deviatoric components, in Fortran https://github.com/Jamal-dev/ttb

B.2.9 Miscellaneous

- Fortran is case insensitive!

- After column 6, Fortran does not recognize spaces; they only serve the purpose of making code more readable

For more information on Fortran, see `http://www.math.hawaii.edu/~hile/fortran/fortmain.htm`

Bibliography

[1] Jacob Aboudi. *Mechanics of composite materials: a unified micromechanical approach*. Elsevier, 2013.

[2] Veysel Alkan, SM Karamihas, and G Anlas. Finite element modeling of static tire enveloping characteristics. *International Journal of Automotive Technology*, 12:529–535, 2011.

[3] Ellen M Arruda and Mary C Boyce. A three-dimensional constitutive model for the large stretch behavior of rubber elastic materials. *Journal of the Mechanics and Physics of Solids*, 41(2):389–412, 1993.

[4] Naga Sai Harika Ayyagari. Multiscale finite element modelling of multi-layer composite membranes, January 2023.

[5] John M Ball. Convexity conditions and existence theorems in nonlinear elasticity. *Archive for rational mechanics and Analysis*, 63:337–403, 1976.

[6] EJ Barbero and R Luciano. Micromechanical formulas for the relaxation tensor of linear viscoelastic composites with transversely isotropic fibers. *International Journal of Solids and Structures*, 32(13):1859–1872, 1995.

[7] Ever J Barbero. *Introduction to composite materials design*. CRC press, 2017.

[8] Ronny Behnke and Michael Kaliske. Finite element based analysis of reinforcing cords in rolling tires: influence of mechanical and thermal cord properties on tire response. *Tire Science and Technology*, 46(4):294–327, 2018.

[9] Allan F Bower. *Applied mechanics of solids*. CRC press, 2009.

[10] R.J. Cembrola and T.J. Dudek. Chord/rubber material properties.

[11] ContiTech. Bonn-60sha from material database. Technical report, 2023.

[12] AV Eitzen, Uwe Weltin, T Brüger, Thomas Steinweger, and Martin Flamm. Modelling of cord-rubber composites of bellow air-springs. In *Constitutive models for rubber VIII*, pages 649–654. CRC Press, 2013.

[13] John Douglas Eshelby. The elastic field outside an ellipsoidal inclusion. *Proceedings of the Royal Society of London. Series A. Mathematical and Physical Sciences*, 252(1271):561–569, 1959.

[14] R Furuhashi and T Mura. On the equivalent inclusion method and impotent eigenstrains. *Journal of Elasticity*, 9(3):263–270, 1979.

[15] Peter Helnwein, Chang Hong Liu, Günther Meschke, and Herbert A Mang. A new 3-d finite element model for cord-reinforced rubber composites—application to analysis of automobile tires. *Finite elements in analysis and design*, 14(1):1–16, 1993.

[16] Rodney Hill. Elastic properties of reinforced solids: some theoretical principles. *Journal of the Mechanics and Physics of Solids*, 11(5):357–372, 1963.

[17] Rodney Hill. A self-consistent mechanics of composite materials. *Journal of the Mechanics and Physics of Solids*, 13(4):213–222, 1965.

[18] MA Holland. The hitchhiker's guide to abaqus. doi: 10.5281/zenodo.1243269, 2017.

[19] Gerhard A Holzapfel. *Nonlinear solid mechanics: a continuum approach for engineering science*. Kluwer Academic Publishers Dordrecht, 2002.

[20] Gerhard A Holzapfel, Thomas C Gasser, and Ray W Ogden. A new constitutive framework for arterial wall mechanics and a comparative study of material models. *Journal of elasticity and the physical science of solids*, 61:1–48, 2000.

[21] Ben G Kao and Ted Warholic. Bat model lateral parameters characterization using finite element model. *Tire Science and Technology*, 31(4):225–247, 2003.

[22] Diederik P Kingma and Jimmy Ba. Adam: A method for stochastic optimization. *arXiv preprint arXiv:1412.6980*, 2014.

[23] Laszlo P Kollar and George S Springer. *Mechanics of composite structures*. Cambridge university press, 2003.

[24] Leonid P Lebedev, Michael J Cloud, and Victor A Eremeyev. *Tensor analysis with applications in mechanics*. World Scientific, 2010.

[25] Jeff S Loeb, Dennis A Guenther, Hung-Hsu Fred Chen, and John R Ellis. Lateral stiffness, cornering stiffness and relaxation length of the pneumatic tire. *SAE transactions*, pages 147–155, 1990.

[26] Randall S Marlow. A general first-invariant hyperelastic constitutive model. *Constitutive Models for Rubber*, pages 157–160, 2003.

[27] G Meschke and P Helnwein. Large-strain 3d-analysis of fibre-reinforced composites using rebar elements: hyperelastic formulations for cords. *Computational Mechanics*, 13(4):241–254, 1994.

[28] Sakthivel Palanivelu, KV Narasimha Rao, and Krishna Kumar Ramarathnam. Determination of rolling tyre modal parameters using finite element techniques and operational modal analysis. *Mechanical systems and signal processing*, 64:385–402, 2015.

[29] Samuel Paolucci. *Continuum mechanics and thermodynamics of matter*. Cambridge University Press, 2016.

[30] Michael JD Powell. The convergence of variable metric methods for nonlinearly constrained optimization calculations. In *Nonlinear programming 3*, pages 27–63. Elsevier, 1978.

[31] V Prot and B Skallerud. Nonlinear solid finite element analysis of mitral valves with heterogeneous leaflet layers. *Computational Mechanics*, 43:353–368, 2009.

[32] Business Research. Railway Air Spring Market Size, Growth Analysis 2030 — businessresearchinsights.com. `https://www.businessresearchinsights.com/market-reports/railway-air-spring-market-107621`, 2023. [Accessed 17-11-2023].

[33] Gregory J Rodin. Eshelby's inclusion problem for polygons and polyhedra. *Journal of the Mechanics and Physics of Solids*, 44(12):1977–1995, 1996.

[34] Michael Smith. *ABAQUS/Standard User's Manual, Version 6.9*. Dassault Systèmes Simulia Corp, United States, 2009.

[35] Michael Smith. Multiple load case analysis. `https://classes.engineering.wustl.edu/2009/spring/mase5513/abaqus/docs/v6.6/books/usb/default.htm?startat=pt03ch06s01aus37.html`, 2022. [Accessed 31-10-2023].

[36] Michael Smith. Reference points. `https://classes.engineering.wustl.edu/2009/spring/mase5513/abaqus/docs/v6.6/books/usi/default.htm?startat=pt03ch11s08s01.html`, 2022. [Accessed 31-10-2023].

[37] Michael Smith. General and perturbation procedures. `https://docs.software.vt.edu/abaqusv2022/English/SIMACAEANLRefMap/simaanl-c-linearnonlinear.html`, 2022. [Accessed 31-10-2023].

[38] Anthony JM Spencer. Part iii. theory of invariants. *Continuum physics*, 1:239–353, 1971.

[39] Clifford Truesdell, Walter Noll, C Truesdell, and W Noll. *The non-linear field theories of mechanics*. Springer, 2004.

[40] Włodzimierz M Tulczyjew. The legendre transformation. In *Annales de l'institut Henri Poincaré. Section A, Physique Théorique*, volume 27, pages 101–114, 1977.

[41] Guido Van Rossum and Fred L Drake Jr. Data structures. `https://docs.python.org/3/tutorial/datastructures.html`, 1995. [Accessed 31-10-2023].

[42] Chongfeng Wei and Oluremi Ayotunde Olatunbosun. The effects of tyre material and structure properties on relaxation length using finite element method. *Materials & Design*, 102: 14–20, 2016.

[43] Yang Wei-min, Chen Can-hui, Chen Ya-ling, and Ren Yan-sha. Finite element analysis of an air spring for automobile suspension. *Journal of Beijing University of Chemical Technology*, 31(3):105, 2004.

[44] Shanyue Wu, Yingyun Huang, and Shijian Zhu. Study on air spring's finite element model. In *International Design Engineering Technical Conferences and Computers and Information in Engineering Conference*, volume 37033, pages 563–567, 2003.

[45] Guan Yanjin, Zhao Guoqun, and Cheng Gang. Influence of belt cord angle on radial tire under different rolling states. *Journal of reinforced plastics and composites*, 25(10):1059–1077, 2006.

[46] Jiatong Ye, Hua Huang, Chenchen He, and Guangyuan Liu. Analysis of vertical stiffness of air spring based on finite element method. In *MATEC Web of Conferences*, volume 153, page 06006. EDP Sciences, 2018.

[47] Oon H Yeoh. Some forms of the strain energy function for rubber. *Rubber Chemistry and technology*, 66(5):754–771, 1993.

[48] Wei Yintao, Luo Yiwen, Miao Yiming, Chai Delong, and Feng Xijin. Finite element modeling for steel cord analysis in radial tires. *Tire Science and Technology*, 41(1):60–79, 2013.